UNIVERSITY OF OKLAHOMA

GRADUATE COLLEGE

GEOLOGICALLY AND WELL-LOG CONSTRAINED QUALITY FACTOR (Q) ANALYSIS FOR SEISMIC RESERVOIR CHARACTERIZATION

A Dissertation

SUBMITTED TO THE GRADUATE FACULTY

in partial fulfillment of the requirements for the

Degree of

Doctor of Philosophy

by

Eshetu Gebretsadik

Norman, Oklahoma

2005

UMI Number: 3174451

UMI

UMI Microform 3174451

ProQuest Information and Learning Company
300 North Zeeb Road
P.O. Box 1346
Ann Arbor, MI 48106-1346

GEOLOGICALLY AND WELL-LOG CONSTRAINED QUALITY FACTOR (Q) ANALYSIS FOR SEISMIC RESERVOIR CHARACTERIZATION

A Dissertation APPROVED FOR THE

SCHOOL OF GEOLOGY AND GEOPHYSICS

By

…………………………………………………

Dr. John D. Pigott

…………………………………………………

Dr. John Castagna

…………………………………………………

Dr. Charles M. Gilbert

…………………………………………………

Dr. Carl Sondergeld

…………………………………………………

Dr. Samuel Osisanya

…………………………………………………..

Dr. Bill Lamb

ACKNOWLEDGMENTS

The author wishes to express his sincere appreciation to all the dissertation committee members, Dr. John D. Pigott for the support and guidance to do this research, and to Dr. John P. Castagna, Dr. M. Charles Gilberst, Dr. Samuel Osisanya, Dr. Carl Sondergeld and Dr. Bill Lamb who were helpful in providing ideas and comments during the course of this research.

I would like to pay homage to the SEG student scholarship committee, especially Mr. Dick Schneider for awarding me a scholarship. In addition, I am grateful to the American Federation of Mineralogical Societies for their generosity and financial support.

I thank the people at PERES COMPANC de Venezuela who supplied the material for my research. Also I would like to express my gratitude to Dr. Chandra Rai for his suggestions and comments. In addition, I am grateful to Gary Stowe, and to the staff and graduate students at the University of Oklahoma Mewbourne School of Petroleum Geology and Engineering Laboratory, for their help in preparing the core samples and showing me how the velocity measuring apparatus works. I do appreciate Mr. Joel Young for his help in preparing the synthetic samples.

My salutation goes to the staff and students of the School of Geology and Geophysics who made life at school pleasant, especially Ahmed Al Ahdal, and the seismic stratigraphy (seismicsista) group who were there for me everyday.

Last but not least I want to recognize all my close friends and family who never left my side during my ups and downs: comforted me when I was down and congratulated me when I succeeded.

TABLE OF CONTENTS

LIST OF FIGURES

LIST OF TABLES

ABSTRACT

The principal objective of this work is to answer the problems following questions:

- Can one extract Q directly from 2D reflection seismic in a way?
- Can the attenuation of a plane wave propagating through a medium be accurately quantified?
- What are the factors that complicate the measurement of attenuation from a propagating plane seismic wave?
- How does quality factor (Q) affect the near and far offset trace attenuation?
- Can one design a forward model that can effectively resolve effects of the complicating factors?
- What is the significance of measuring attenuation due to anelastic rock properties?

A forward model using 2D reflection seismic is used to observe effects of different values of Q and of offset on the seismic wavelet, both in the time domain and frequency domain. The result indicates Q inversely affects amplitude decay (i.e. the higher value of Q, the smaller the amplitude decay), while offset directly affects amplitude decay. In addition, preferential attenuation of the higher frequency content is prevalent, but phase distortion is not observed.

Measurements of P- and S-wave velocities are conducted on alternating layers of acrylic and aluminum. In this experiment, both thickness of the layers, and frequency of the propagating wave are varied. Based on these observations, for wavelength/thickness (λ/d) >> 1, the medium behaves as a transversely isotropic medium, and for (λ/d) << 1 the medium; is represented by individual homogeneous pieces. Velocity dispersion is minimal in both cases. However, when (λ/d) is between the two extreme cases there is a significant velocity dispersion due to interbed multiple scattering.

P- and S-wave velocities, Q_p and Q_s were measured on 46 core samples collected from Well C-276, La Concepcion Field, Lake Maracaibo Venezuela. Mmeasured V_p/V_s and Q_p/Q_s are correlated with petrophysical properties such as porosity and permeability of the core samples. Q_p/Q_s has shown a very good relationship with porosity and permeability. Finally, Q is estimated from a CMP-gather extracted 3D survey from La Concepcion Field, Venezuela. The computed Q values are correlated with Q values from the well, and there is a very good relationship between the two. Furthermore, all Q measurements show correlation with the porous and permeable layers. Therefore, properly measured Q can be used together with other geophysical methods in reservoir characterization.

In the Name of the Father The Son and Holy Spirit Amen!

I dedicate this work to my wonderful wife
Tafesework Sahlu

በስመ አብ ወወልድ ወመንፈስ ቅዱስ አሜን
አስጀምሮ ሳስጨረሰኝ አምላክ ክብር ምስጋና ይግባው

ይህ ስራዬ በሁሉም ነገር ላልተለየችን
ለባለቤቴ ወ/ሮ ታፈሰወርቅ ሳህሉ ስጦታ ይሁንልኝ

Chapter 1

PROBLEM DEFINITION AND GEOLOGICAL SETTING

1.1 Introduction

Seismic waves are used to image and interpret the subsurface, and seismic properties such as velocities, travel time, attributes, AVO and intrinsic attenuation are used to characterize lithology, porosity, degree of saturation and environment. However, the scale at which information about the subsurface is obtained depends on frequency content of the propagating seismic wave and scale of the heterogeneity of the subsurface. Since the frequency of seismic waves varies widely depending on the seismic method used, the scale of the layers that can be mapped varies considerably. Correlating these investigations made at different scale plays a significant role exploration, in particular in reservoir geophysics.

In addition, intrinsic attenuation, quantified by quality factor (Q), if measured accurately, can be used to predict petrophysical properties such as lithology, porosity, degree of saturation, and environment (pressure and temperature conditions). However, there are factors complicating computation of Q from plane waves propagating in a layered medium. For a wave propagating in a medium depending on the scale of the heterogeneity of the medium and the scale of the wavelength of the wave velocity dispersion and/or intrinsic attenuation will affect the wave. Discriminating the processes at work, and properly measuring Q have application in reservoir characterization.

The aim of this work is to explore the problems listed below, and elaborate on the significance of computing attenuation from reflection seismic data:

- Can one extract Q directly from reflection seismic in a meaningful way?
- Can the attenuation of a plane wave propagating through a medium be accurately quantified?
- What are the factors that complicate the measurement of attenuation from a propagating plane seismic wave?
- How does quality factor (Q) affect the near and far offset trace attenuation?
- Can one design a forward model that can effectively resolve effects of the complicating factors?
- What is the significance of measuring attenuation due to anelastic rock properties?

1.2. Exploration History

The indication of hydrocarbons in Venezuela goes as far back as the 16th century, when it was first mentioned by Fernandez de Oviedo in 1553. He wrote about oil seepages off the western shore of the Cubague Islands in 1540 (Berneys et al., 1996). However, in the Zulia province of Western Venezuela, surface exploration for petroleum started in 1920, followed by gravity exploration in 1924. The La Concepcion Field is part of the Western Province of Lake Maracaibo basin, Zulia State, Venezuela. The field is located on the western coast of Lake Maracaibo (Figure

1.1), northeast of Boscan Field, and east of La Paz Field. The field was first discovered in 1925 (Berneys et al., 1996) as a result of surface exploration and exploratory drilling.

In this region, production generally is from two zones; the lightest crude and condensates are from the oldest and deepest formations: the basement and Cretaceous, while the heavy to medium oils are associated with the Tertiary (Eocene) (Berneys et al., 1996). The La Concepcion Field produces light oil and gas from Cretaceous and Tertiary formations, whereas the nearby La Paz Field produces light oil from the basement and Cretaceous.

Exploration for oil and gas in Venezuela has along history, but still has a long way to go. With advances in technology and geophysics, exploration in Venezuela has great potential.

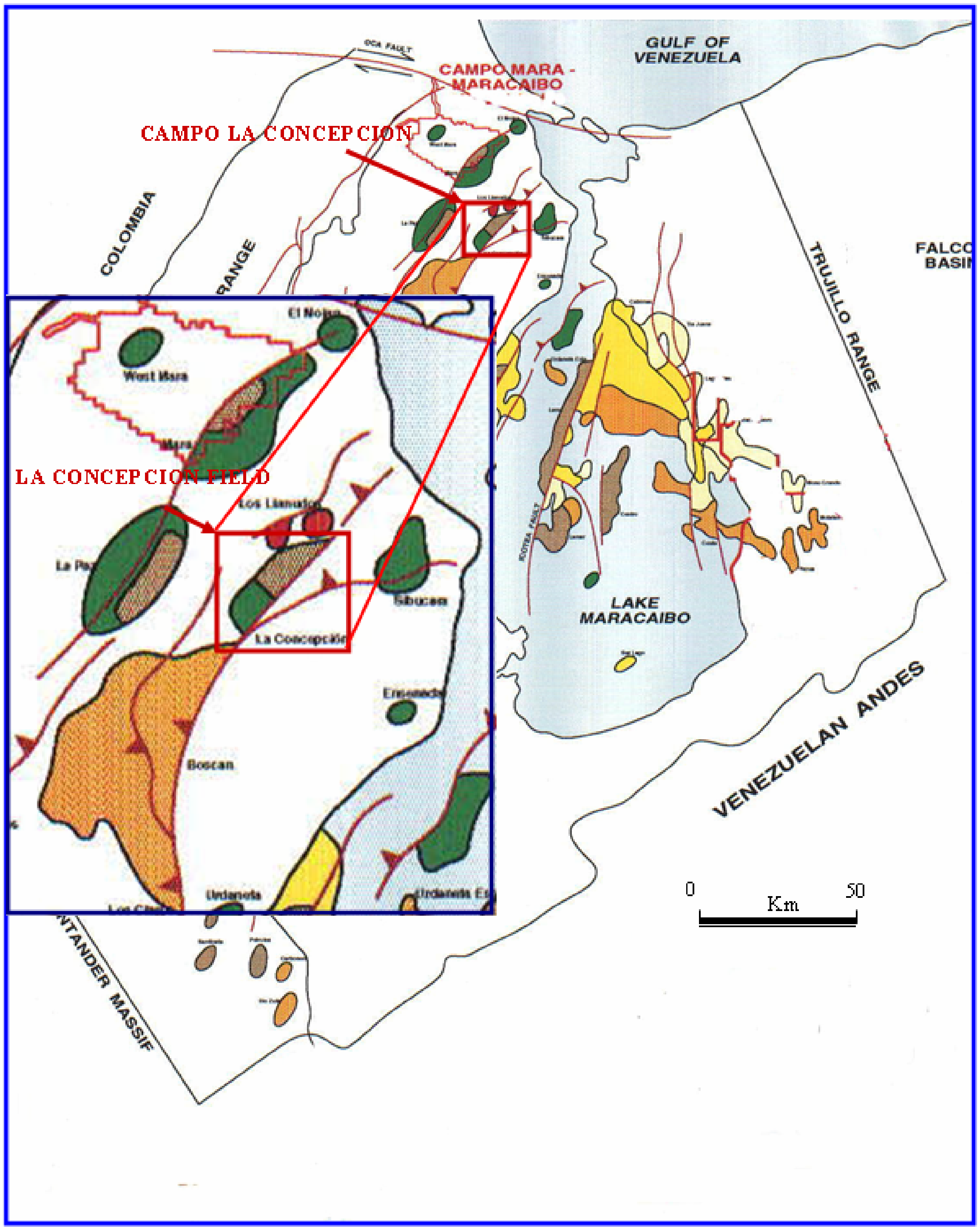

Figure 1.1.Venezuela oil fields, and The La Concepcion Field, Zulia, Venezuela (in-set)

1.3 Objectives

The aim of this study is to use the geology of the La Concepcion Field to constrain the velocity, intrinsic attenuation, and quality factor computed on a seismic line from this field. In this chapter, lithology, diagenesis, porosity and permeability of each formation are described. In addition, type and distribution of lithologies, diagenetic processes, porosities and permeability are briefly discussed. This information is used to tie down the theoretically and experimentally computed velocities, intrinsic attenuation, and quality factor from the seismic data.

1.4 Stratigraphy

The La Concepcion Field has a very thick Cretaceous section (1178 ft) in the studied well (Well C-276). The stratigraphic section in Well C-276 starts at the base with the Cogollo Group, and is topped by the La Luna Formation. The underlying unit in the well is the Cogollo Group and which ranges in age from Baremian to Cenomanian; it is characterized by mixed carbonate and siliciclastic at the base and clean carbonate at the top. However, there is a basal clastic unit, Rio Negro Formation of Barremian age. There are three formations that belong to the Cogollo Group (Apon, Lisure, and Maraca), and these formations are the reservoir units in the La Concepcion Field. The Apon Formation is a limestone unit with rather significant interbeds of shale and dolomite. The top part of the formation is mainly shale with abundant dolomite. The Lisure Formation is a limestone unit with interbeds of dolomitic limestone. The dolostone interbeds increase in abundance towards the base. The overlying Maraca Formation is chiefly limestone with minor interbeds of sandstone, dolomitic limestone, and shale. The sandstone and shale interbeds are mainly at the base, but the dolomitic limestone interbeds are distributed evenly in the section. Overlying the Maraca Formation is the La Luna Formation, Cenomanian to Santonian. The La Luna Formation is generally a carbonate (mudstone/wackestone to packstone), with skeletal grains of possibly foraminifera fragments (Figure 1.5b). It also has interbeds of thinly laminated shale at the base (Figure 1.2). The La Luna formation forms both the source and sealing rock in the field.

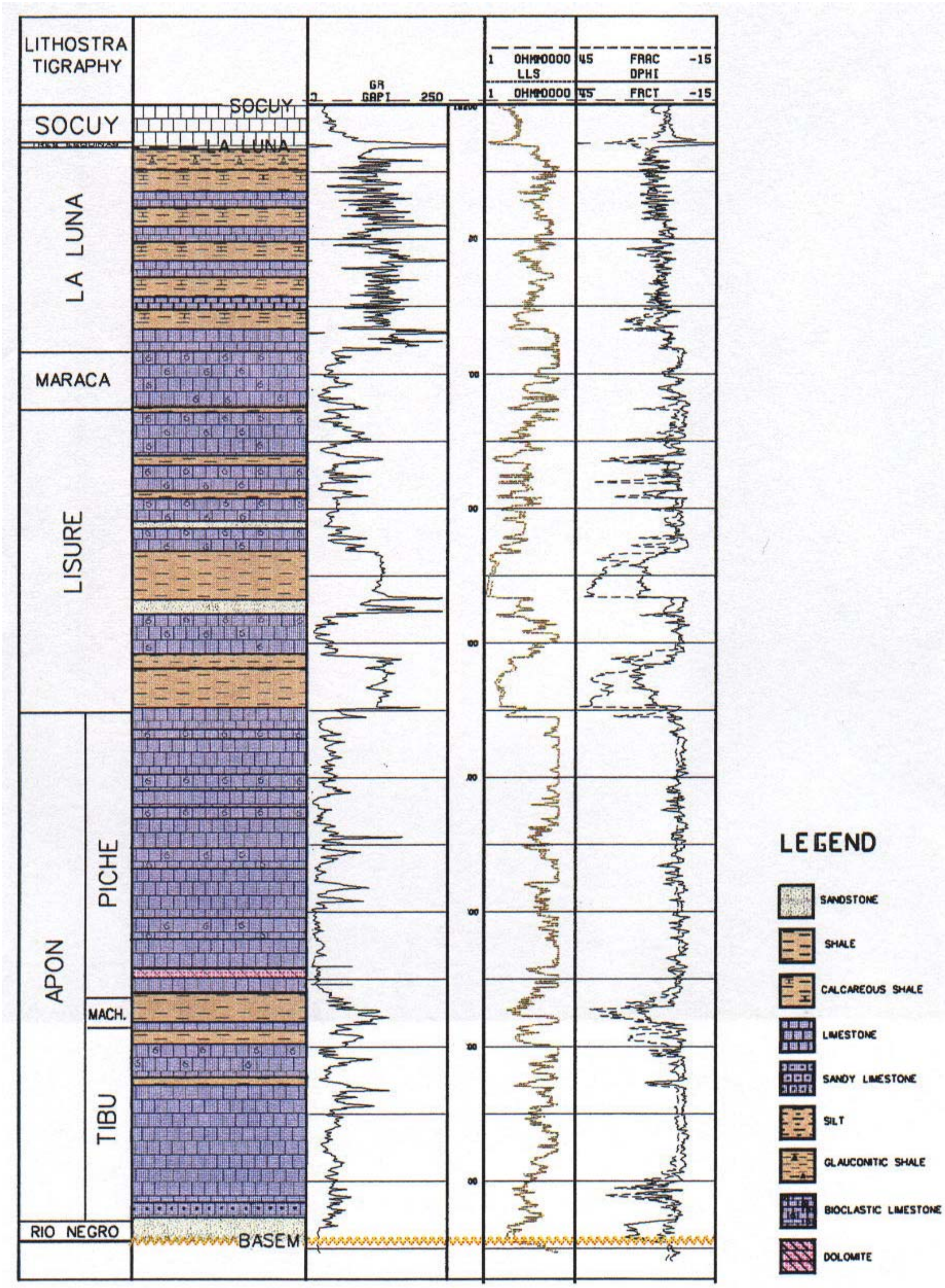

Figure 1.2 Lithostratigraphy for West Maracaibo Basin (Murat and Muñoz, 1997)

1.5 Chronostratigraphy

The chronostratigraphy of La Concepcion Field ranges in age from Triassic basement to the Eocene La Luna Formation (Figure 1.3). The productive formations of the field are the Cretaceous and Early Tertiary formations. The Rio Negro Formation of Barremian age forms the base of the Cretaceous stratigraphy, and uncomformably overlies the Triassic basement. Overlying the Rio Negro is the Cogollo Group, which ranges in age from Aptian to Early Cenomanian, and it underlies the La Luna Formation of Early Cenemanian to Early Campanian age (Figure 1.3). The thickness of the Cogollo Group in the study well (C-270) is 1103 feet, while the thickness of the La Luna Formation in the logged section is 75 feet.

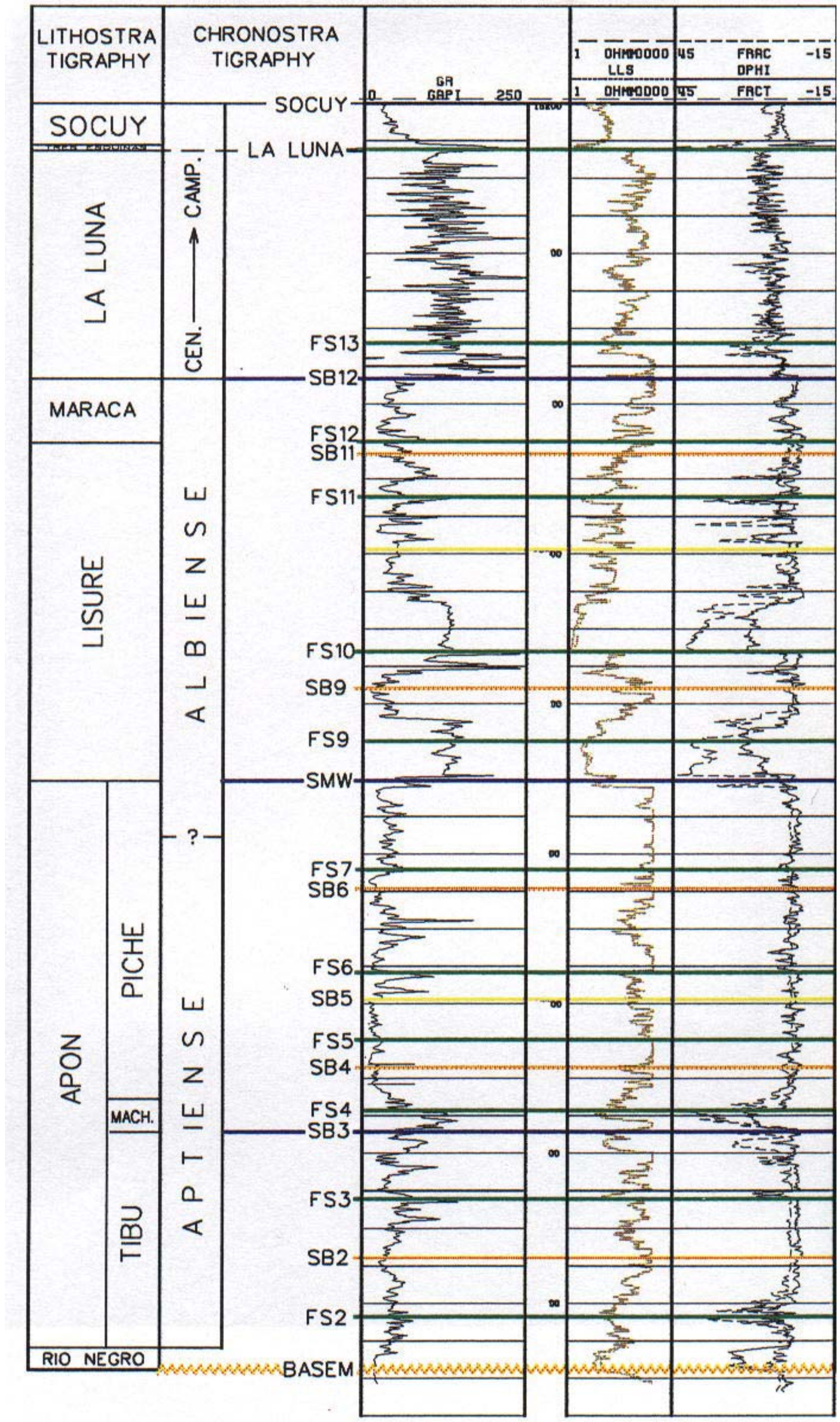

Figure 1.3. General Chronostratigraphy Cretaceous of the Maracaibo Basin (Murat and Muñoz, 1997)

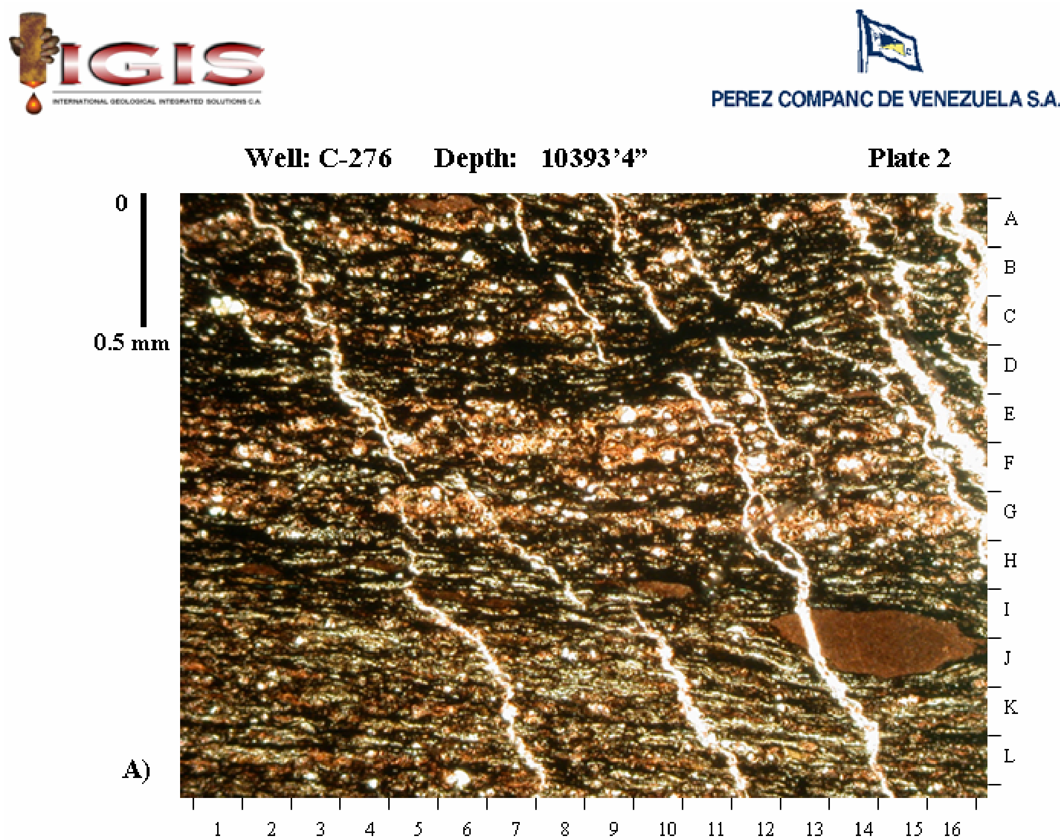

Figure 1.4 Thin section from core sample (La Luna Formation), Well C-276, showing lamination.

1.6 Depositional Environment

The Cretaceous basal unit, the Rio Negro Formation, was deposited in a fluvio-shoreline environment. The depositional environment of the overlying Cogollo Group varies from bars and lateral lagoons for the Apon Formation to marine for the Maraca Formation. The La Luna formation was deposited in a low-energy euxinitic marine environment (Berneys et al., 1996).

1.7 Petrographic Study of Core Samples from Well C-276

Visual investigation and analysis by Scanning Electron Microscopy (SEM), X-ray Diffraction (XRD), and thin-section petrography (corex UK, 2002) of core samples, from Well C-276 at various depths in La Concepcion Field, Venezuela, showed a fairly uniform mineralogical composition.

The most common detrital grains throughout the samples were fragments of bivalves (Figure 1.5a and 1.7); the internal structure of these fragments was preserved as a result of neomorphism, and this preservation helped in their identification. Other bioclastic fragments forming the detrital grains were observed in small amounts. Non-skeletal grains are rare, except ooid and peloidal grains which are dominant in a few samples (Figure 1.5a and 1.5b). The peloids shown in the thin section range in size between 1 mm and 200 μm, and make up 23% of the point count. In addition, glauconite is found in moderate amounts in most samples (Figure 1.6). Quartz grains are also present in trace amounts in majority of the samples, and the quartz grains are more concentrated around stylolites (Figure 1.7).

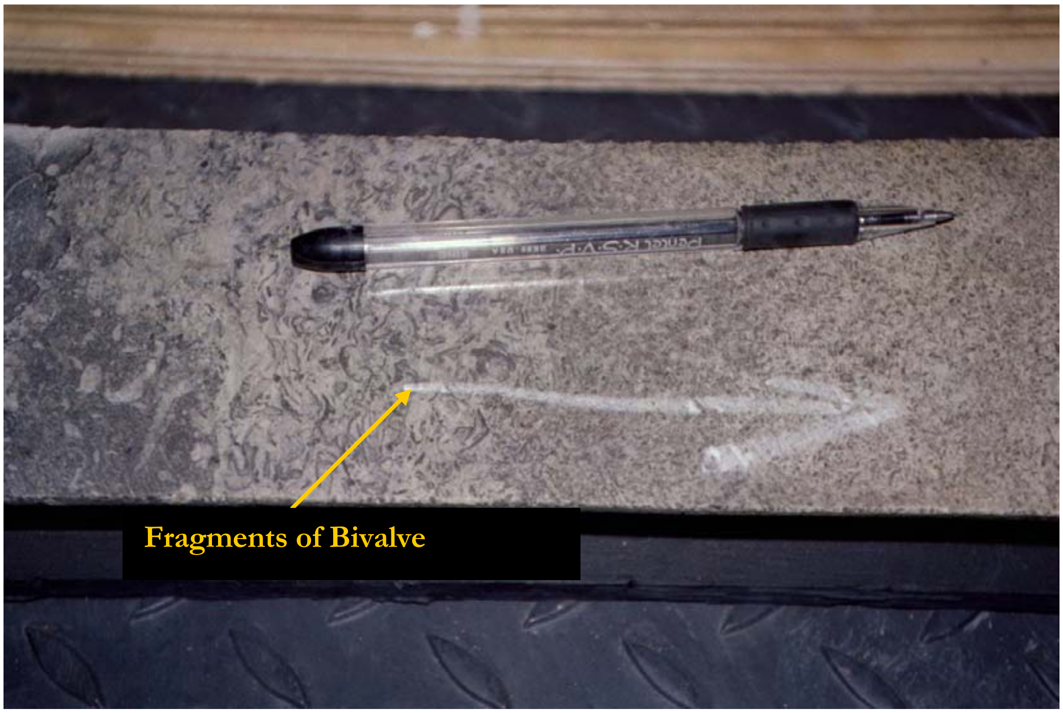

Figure 1.5a: Hand specimen from core sample, Well C-276, showing fragments of skeletal grains (bivalves), ooids and peloids, depth 11301.5' to 11302'.

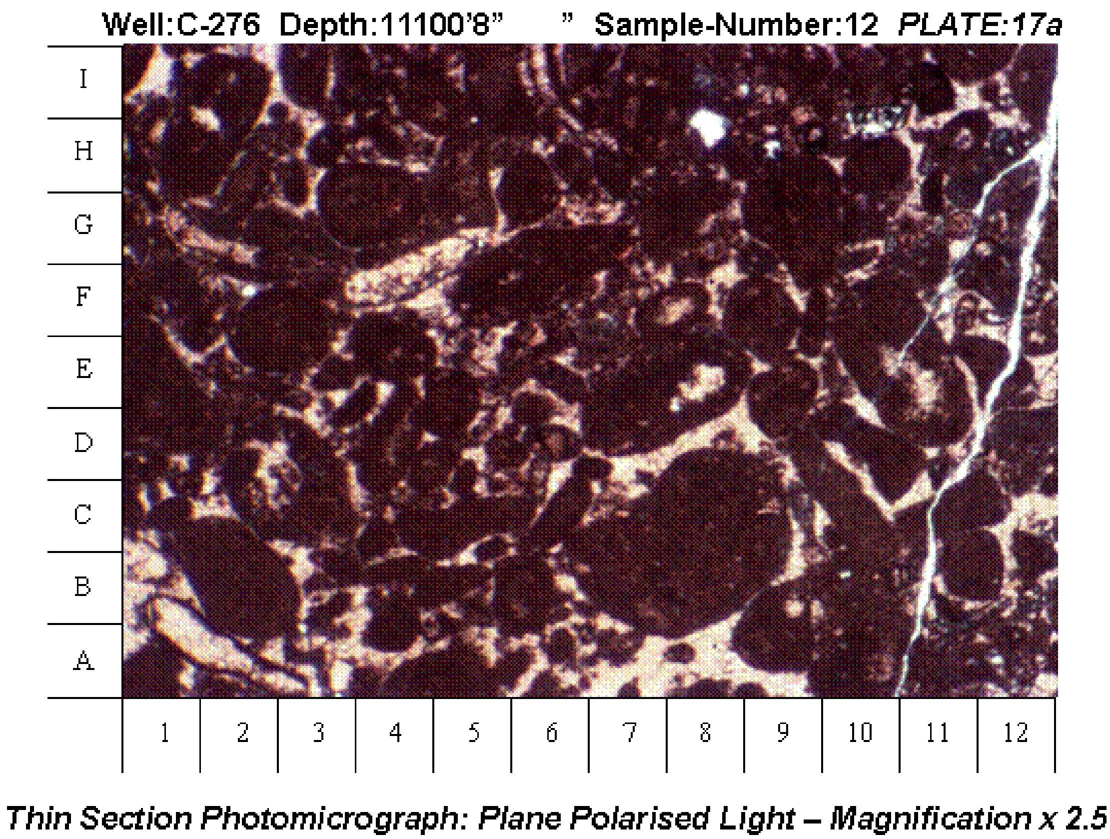

Figure 1.5b. Thin section from core sample, Well C-276, showing peloidal grains, skeletal fragments, and fracture on the right corner of the section.

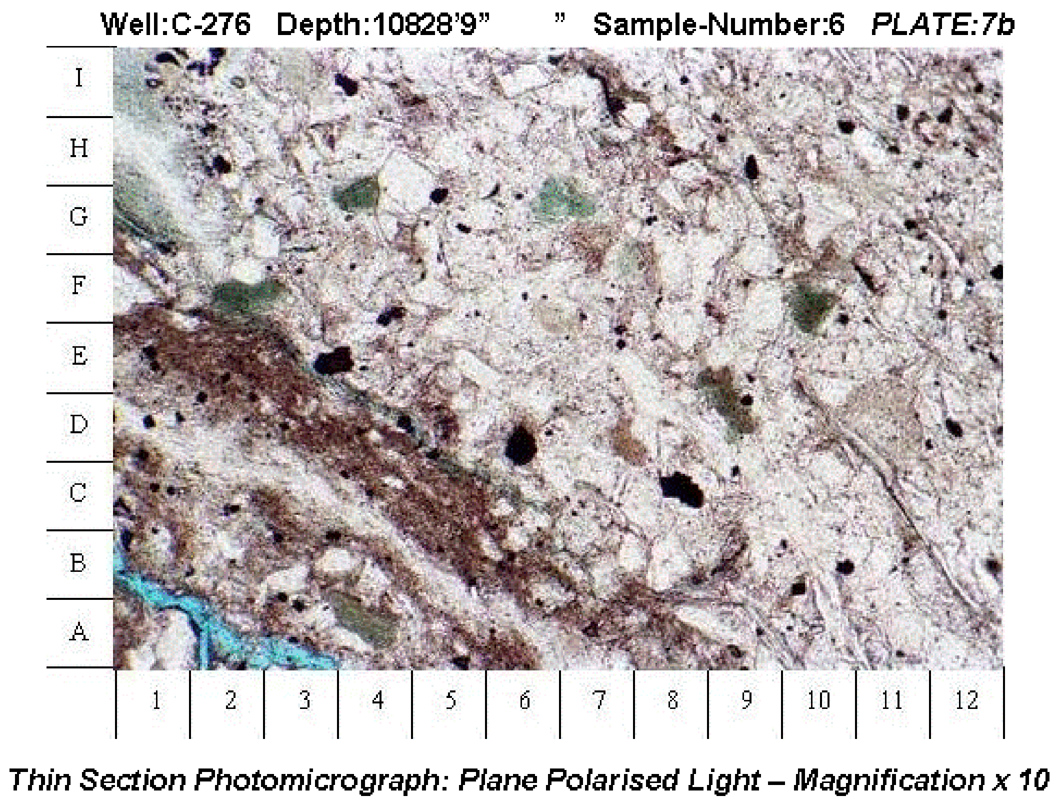

Figure 1.6a Thin section from core sample, Well C-276, showing quartz grains (G6, H5), and glauconite (F2, G4, F10).

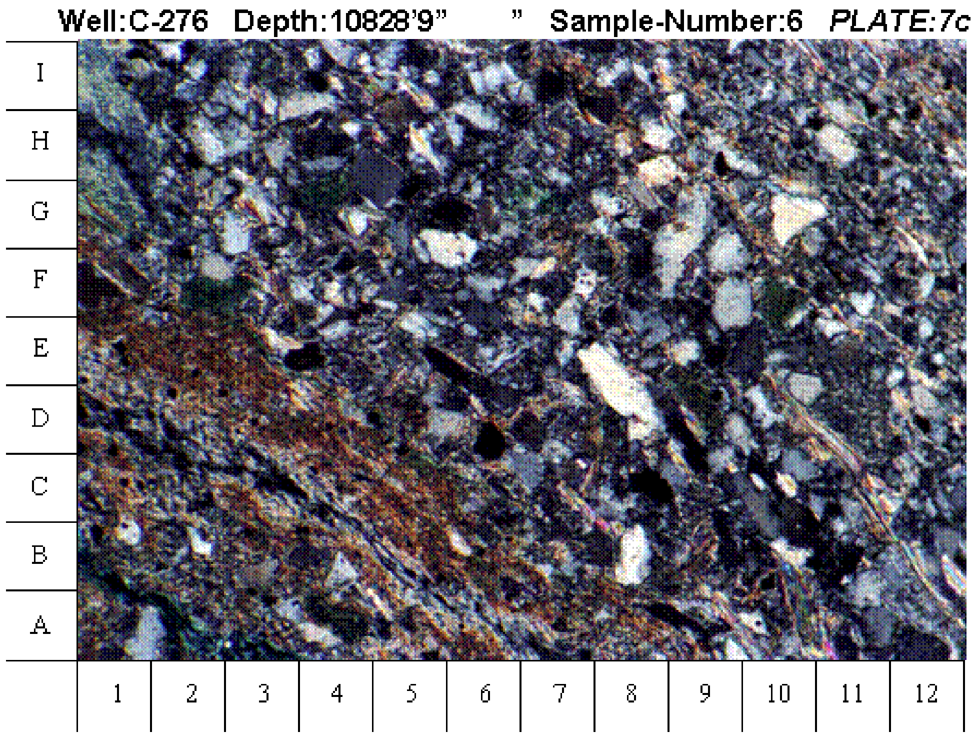

Thin Section Photomicrograph: Cross Polarised Light – Magnification x 10

Figure 1.6b Thin section from core sample, Well C-276, showing quartz, mica (lower left corner) and glauconite (Figure 6a under Cross-polarised light).

Well:C-276 Depth:10460'9.5" Sample-Number:2 *PLATE:2a*

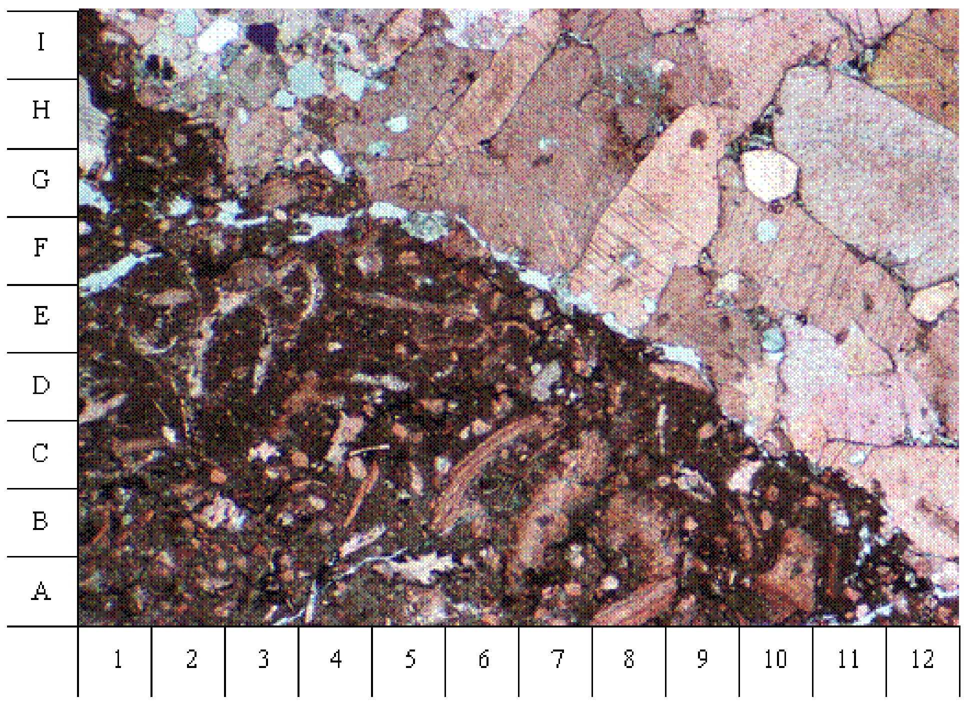

Thin Section Photomicrograph: Plane Polarised Light – Magnification x 2.5

Figure 1.7 Thin section from core sample, Well C-276, showing skeletal fragments (bivalves) and stylolite.

Moreover, the matrix is dominated by micrite, which sometimes makes up to 55% of some samples, and micritisation of sparite is observed in some samples.

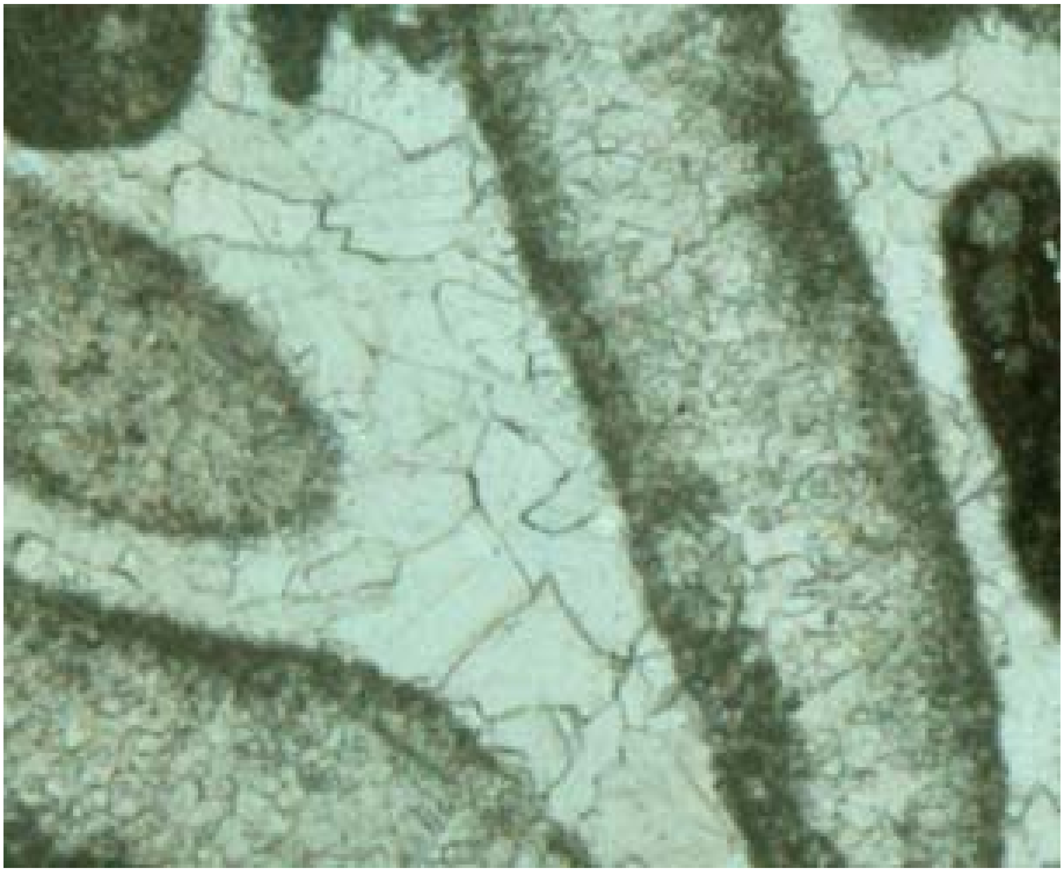

Figure 1.8 Thin section from core sample, Well C-276, showing sparite filling intra-granular porosity, depth = 10897'.

Sparite is present in most of the samples, generally forming the cement filling porosity (Figure 1.8). In some of the samples, it has formed through neomorphism of the micritic matrix. It is also observed replacing the skeletal fragments (bivalves); this occurs in two ways; dissolution of the shell, and infilling and neomorphism. Diagenesis is prevalent, especially cementation, and dolomitization is not uncommon (Figure 1.9a and 1.9b). Moreover, different dgrees of dolomite formation are found throughout the samples The dolomitization process ranges from partial to complete (Figure 1.9a and 1.9b). There are generally well-developed rhomboidal crystals and have formed along tracts of more porous and permeable sediment (Figure 1.9a and 1.9b).

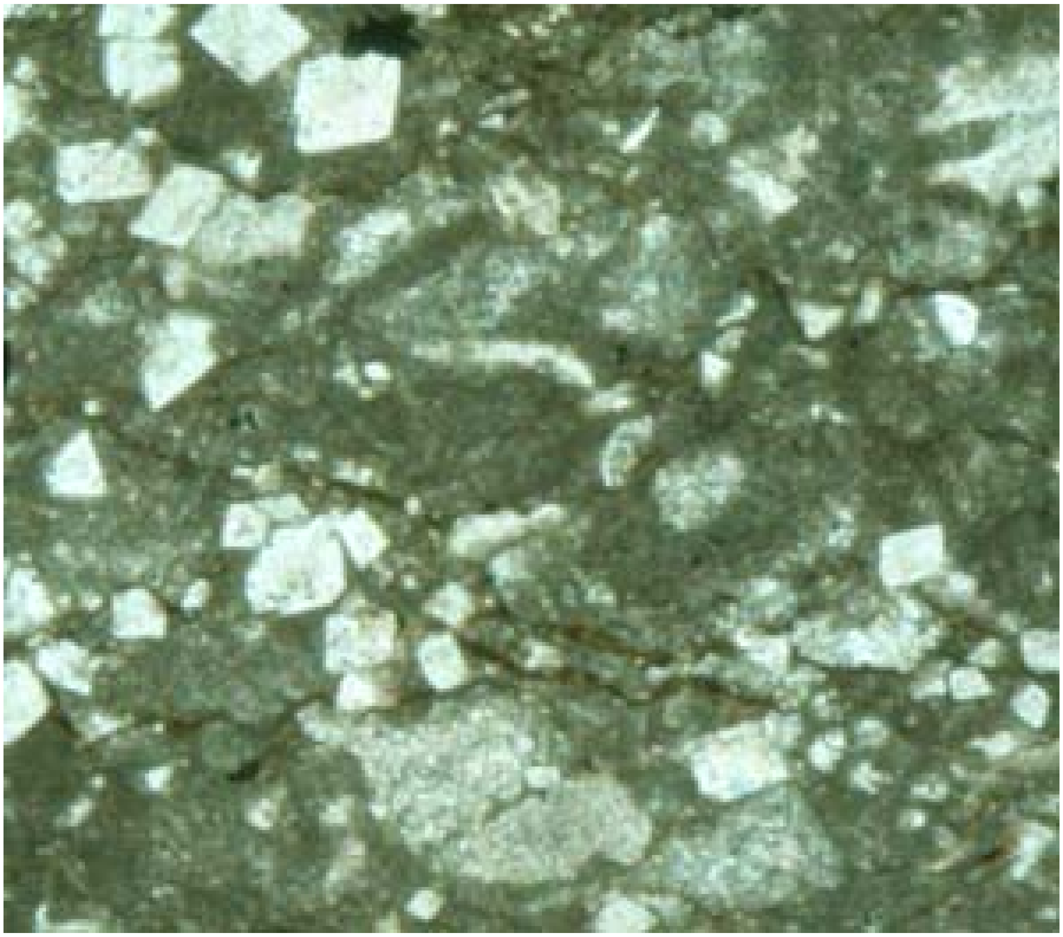

Figure 1.9a. Thin section from core sample, Well C-276, showing partial dolomitization with floating dolomite rhombs in sparite matrix, depth = 10770’7”.

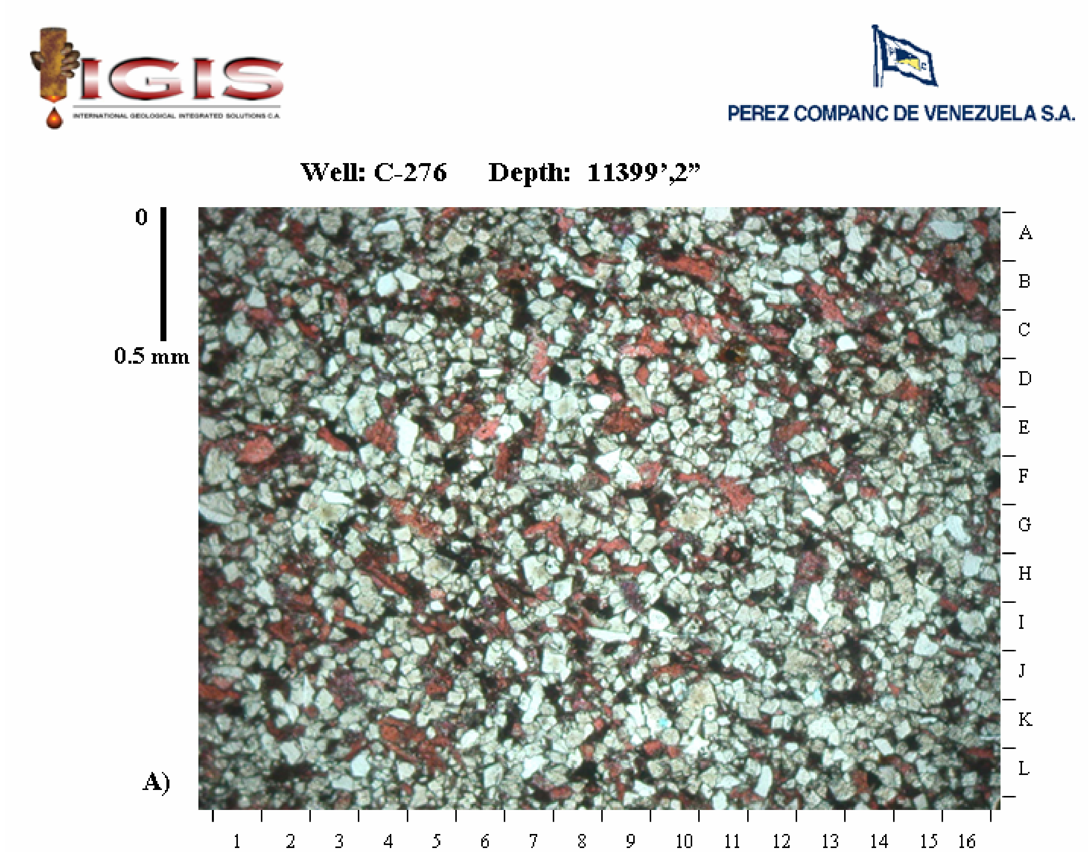

Figure 1.9b Thin section from core sample, Well C-276, showing complete dolomitizat showing well-formed dolomite rhombs, and intra-granular porosity with dead oil.

1.8 Porosity

In general, porosity is poor to moderate and permeability is very low. Microporosity is observed in samples containing micritic cement, which is not altered by neomorphism. In addition, some samples contain limited and isolated vuggy and moldic porosity (Figure 1.11), which is ineffective for permeability. Fracture porosity does make up the largest proportion of porosity in the samples (Figure 1.10); some of this fracture porosity could be an artifact of sample preparation (Murat, 2001). Dead oil is noted in most samples; it is found in veins, coating vuggy porosity and filling some microporosity (Figures 1.9b, and 1.11 and 1.12).

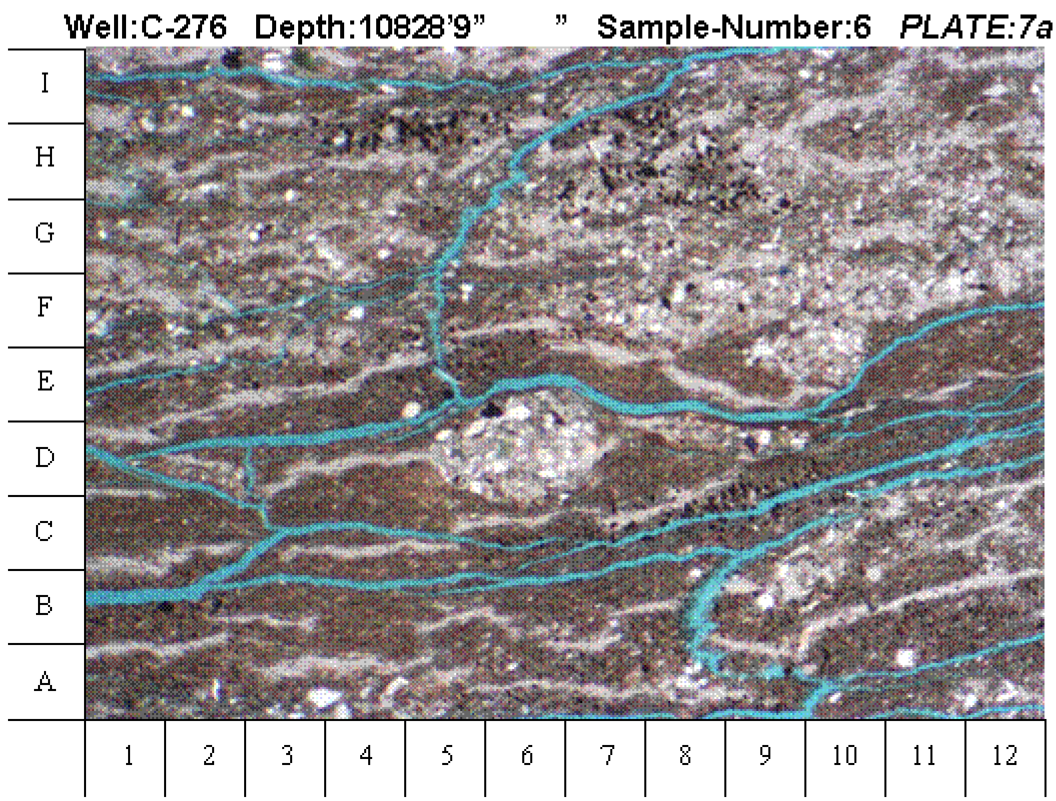

Thin Section Photomicrograph: Plane Polarised Light – Magnification x 2.5

Figure1.10. Thin section from core sample, Well C-276, showing fracture porosity (blue stained areas).

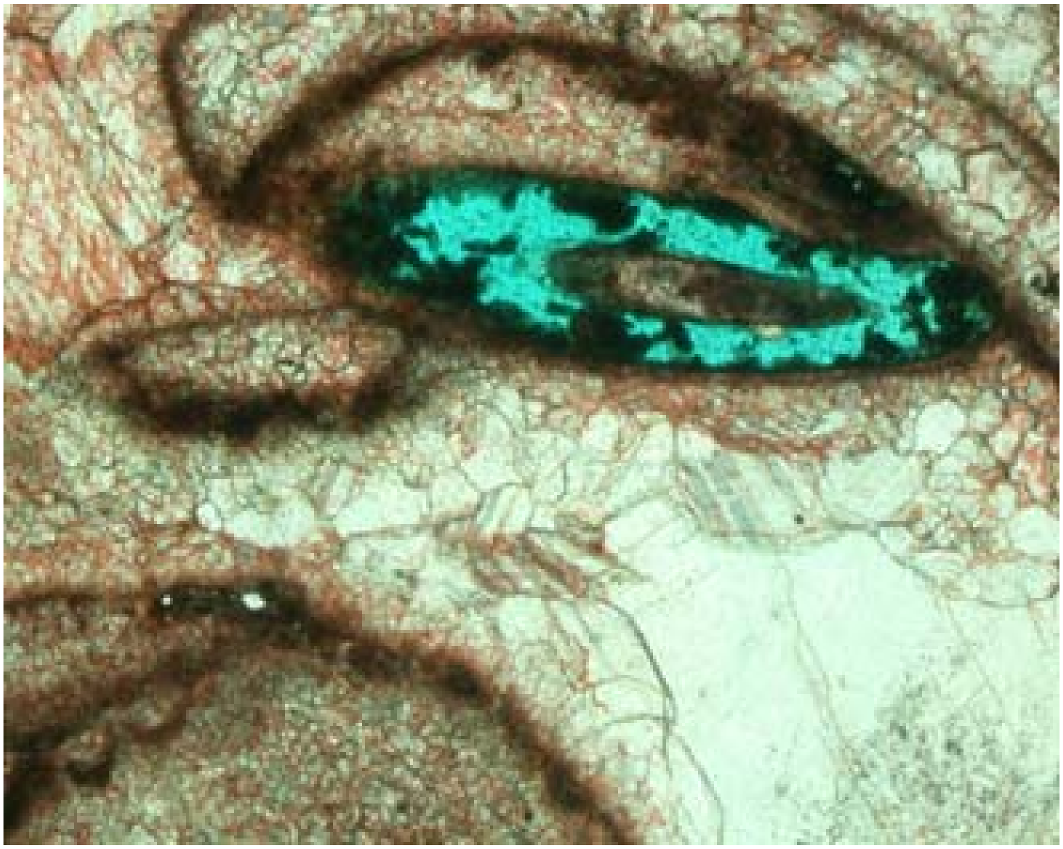

Figure 1.11 Thin section from core sample, Well C-276, showing moldic porosity formed by dissolution of skeletal grain, and oil filling the moldic porosity, depth = 11288’8”.

Well:C-276 Depth:11026'4.5"   " Sample-Number:10 *PLATE:14b*

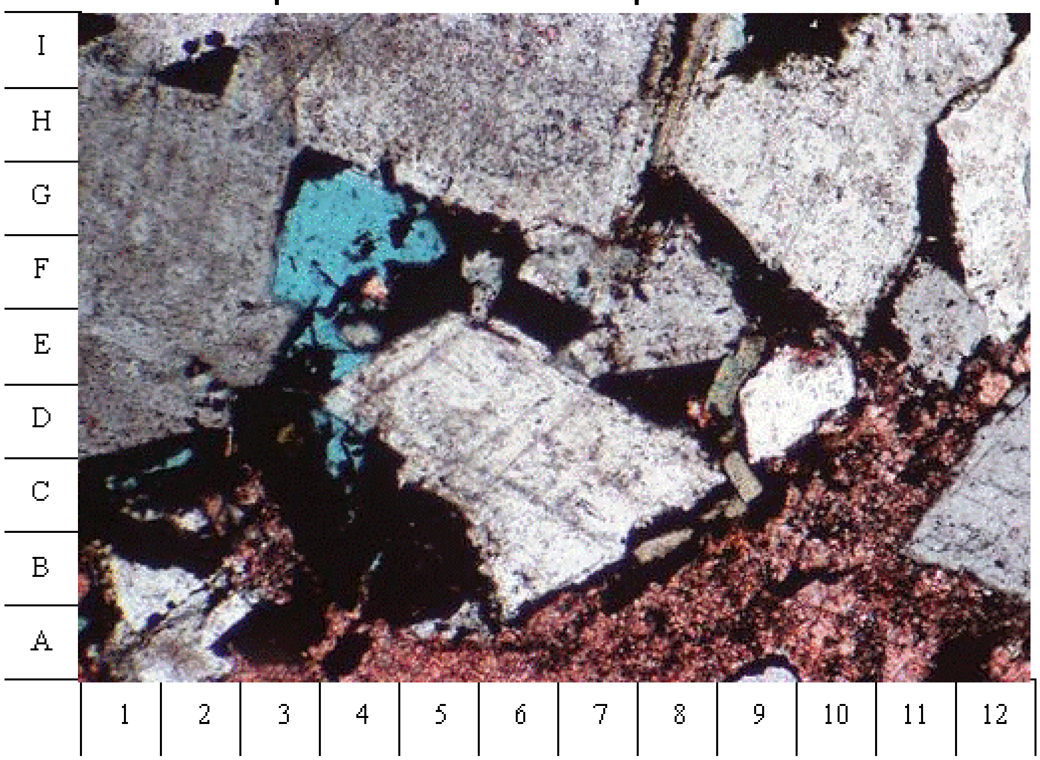

Thin Section Photomicrograph: Plane Polarised Light – Magnification x 10

Figure 1.12. Thin section from core sample, Well C-276, showing dead oil filling microporosity.

1.9 Summary

The La Concepcion Field, which is part of the Western Province of Lake Maracaibo Basin has been explored close to 80 years, and it is still producing. In addition, with the increase the science geophysics, and the advance of technology exploration in the area has a long way to go. Even though, the primary porosity in the samples studied show low values, the type of porosity, microporosity, fracture porosity, vuggy porosity and moldic porosity have potential to make a good reservoir unit. Especially, with the wide spreads of fracturing (provided not sample preparation artifact) there is high potential for the presence of a good reservoir. Diagenesis process is prevalent in the field, and this process plays a double role, it can enhance the reservoir quality, or destroy it.

Therefore, this section forms the geological setting for the ensuing Q analysis from a 3D survey acquired from La Concepcion Field.

Chapter 2

Forward Modeling

2.1 Introduction

In order to investigate ultimate Q extraction from seismic, first we shall examine the theoretical Q effects from a forward model. Forward modeling, using 2D reflection seismic data from the Red Sea, Yemen, was performed to see the effect of constant Q at variable offset, and variable Q with no offset, on the amplitude spectrum of a propagating wavelet. Amplitude decay, due to transmission loss and spherical divergence, was computed prior to calculation of attenuation due to an anelastic property of the transmitting media. The variable offset at constant Q is directly related to amplitude decay, while variable Q at no offset is inversely related to amplitude decay.

A data conditioning process, such as noise reduction, multiple suppression and amplitude balancing for transmission loss and spherical divergence, was conducted using Omega (Western Geco) software. These processes include surface consistent deconvolution, radon transform (tau-p) velocity filtering, band pass filtering, and program-controlled gain. After data conditioning and sorting to CMP-gather, interactive velocity picking of stacking or root mean square (RMS) velocity was performed on CMP and semblance gather panels. Then, the same CMP-gather (CMP# 300) with 23 traces was extracted into a text format. Since the data were originally sampled at 1 ms, it was necessary to resample the data to 20 ms. The CMP-gather text data were loaded to a script written in MATLAB software for forward modeling, and analysis of the effects of constant Q at variable offset and variable Q at no offset on the time domain wavelet amplitude and frequency domain amplitude spectrum.

Finally, forward modeling on the extracted CMP-gather was conducted to visualize change on the propagating wavelet and amplitude spectrum due to constant Q at variable offset, and variable Q with no offset. The modeling result shows a higher Q value decreases the change of the shape of the propagating wavelet as well as the bandwidth of the amplitude spectrum. However, increasing the offset decreases the amplitude of the pulse and the bandwidth of the amplitude spectrum.

2.2 Objectives

The focus of this study is to show theoretically and computationally the effects of offset distance transmission loss and quality factor on amplitude decay of a plane propagating wave. The various factors affecting seismic amplitude decay will be evaluated. Furthermore, the important parameters of intrinsic attenuation coefficient and quality factor effects on amplitude will be measured. Finally, based on the results obtained from this forward modeling, a framework will be set to calculate intrinsic attenuation coefficient and quality factor on 3D reflection seismic data from Venezuela.

2.3 Data Acquisition

2D reflection seismic data with common-shot gathers from the Yemen Red Sea area were used for this forward modeling study. The data were acquired by Western Atlas in 1985, using an air gun as an energy source (Western High Pressure air-guns) fired at water depths of 6 meters. Recording was done with hydrophones, six hydrophones per group, with 3200 meters streamer length, and the cable was at 6 meters water depth. The record length recorded is 4.096 seconds, and acquisition-sampling rate is 1 ms. In addition, the raw data were filtered in the field with low-cut (LC) 12/6 Hz dB/octave and high-cut (HC) 375/72 Hz dB/octave. The data were in SEGD format, and stored on 6250 BPI 9-track tape. The data on the 9-track tapes were transferred to an IBM 3590 tape, which is compatible with the IBM 3590 tape reader available at the lab.

2.4 Data Processing

The 2D reflection seismic data were loaded onto Omega (Western Geco) processing software. The SEGD data were input, and demultiplexed using the proper marine geometry, and were output as common-shot gathers. The common-shot gathers were processed to reduce noise, to reduce water bottom and inter-bed multiples, to increase the signal content, and to retain the proper amplitude. The processing included surface-consistent deconvolution, radon transform (tau-p) velocity filtering, amplitude balancing (gain), and interactive velocity processing (IVP). After the processing, a gather was extracted from the section and output as a text file for forward modeling.

2.4.1 Surface Consistent Deconvolution

Surface-consistent deconvolution is one set of deconvolution processes used to improve the temporal resolution of seismic data by compressing the basic wavelet. In addition, the deconvolution process removes a significant part of the multiple energy from a section (Yilmaz,1987). Theoretically, in surface-consistent deconvolution, the seismic trace is decomposed into the convolutional effects of source, receiver offset, and Earth's impulse response. This explicitly accounts for variation in wavelet shape due to near-source and near-receiver conditions, and source receiver separation (Yilmaz, 1987). The surface-consistent deconvolution process used here inputs seismic data in shot-gather into the input seismic function module (INPUT) (Figure 2.1). The second step in the process is the Surface-Consistent Deconvolution Analysis (SC_DCN_SPCTRL_ANL) SFM, which generates logarithmic power spectra for use in the surface-consistent deconvolution process. Next, the log power spectra generated by the (SC_DCN_SPCTRL_ANL) SFM are decomposed by the Surface-Consistent Deconvolution Spectral Decomposition (SC_DCN_SOCTRL_DECOMP) SFM into surface-consistent spectral estimates corresponding to the source, detector, subsurface midpoint, and offset component for each window of each trace. Then, these spectral estimates are used to design a surface-consistent predictive deconvolution operator by the Surface-Consistent Deconvolution Operator Design (SC_DCN_OPR_DESIGN) SFM. Finally, the deconvolution operator application (DCN_OPR_APPLY), applies the designed operator to the seismic data (Figure 2.1). The assumption of surface consistency implies that the basic wavelet shape depends only on the source and receiver location, not on the details of the ray path from source to reflector to receiver (Yilmaz, 1987). The surface-consistent deconvolution process improves the data content by increasing the wavelet bandwidth and removing multiples (Figure 2.2).

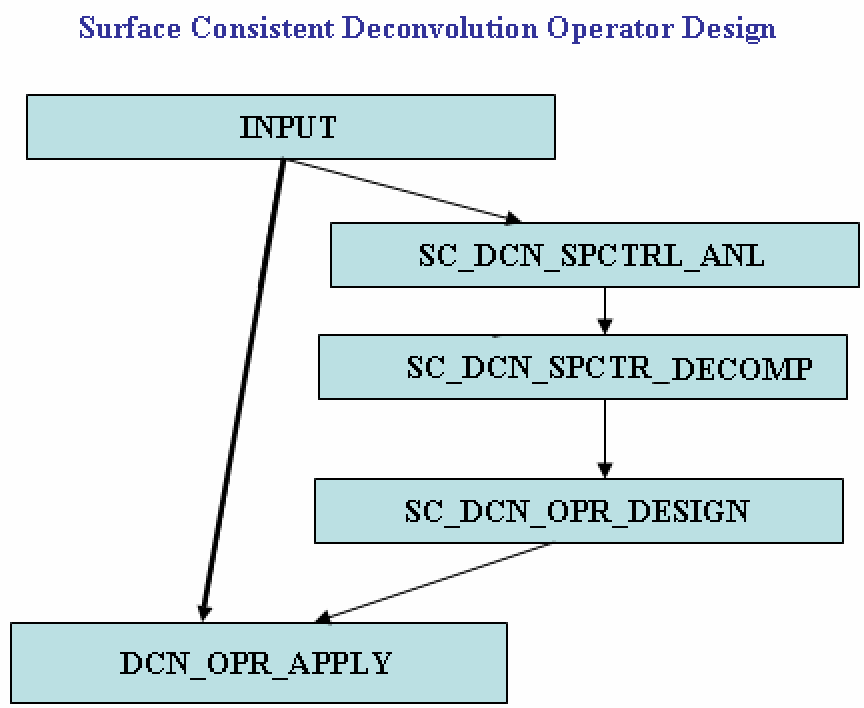

Figure 2.1. Surface consistent deconvolution seismic flow module.

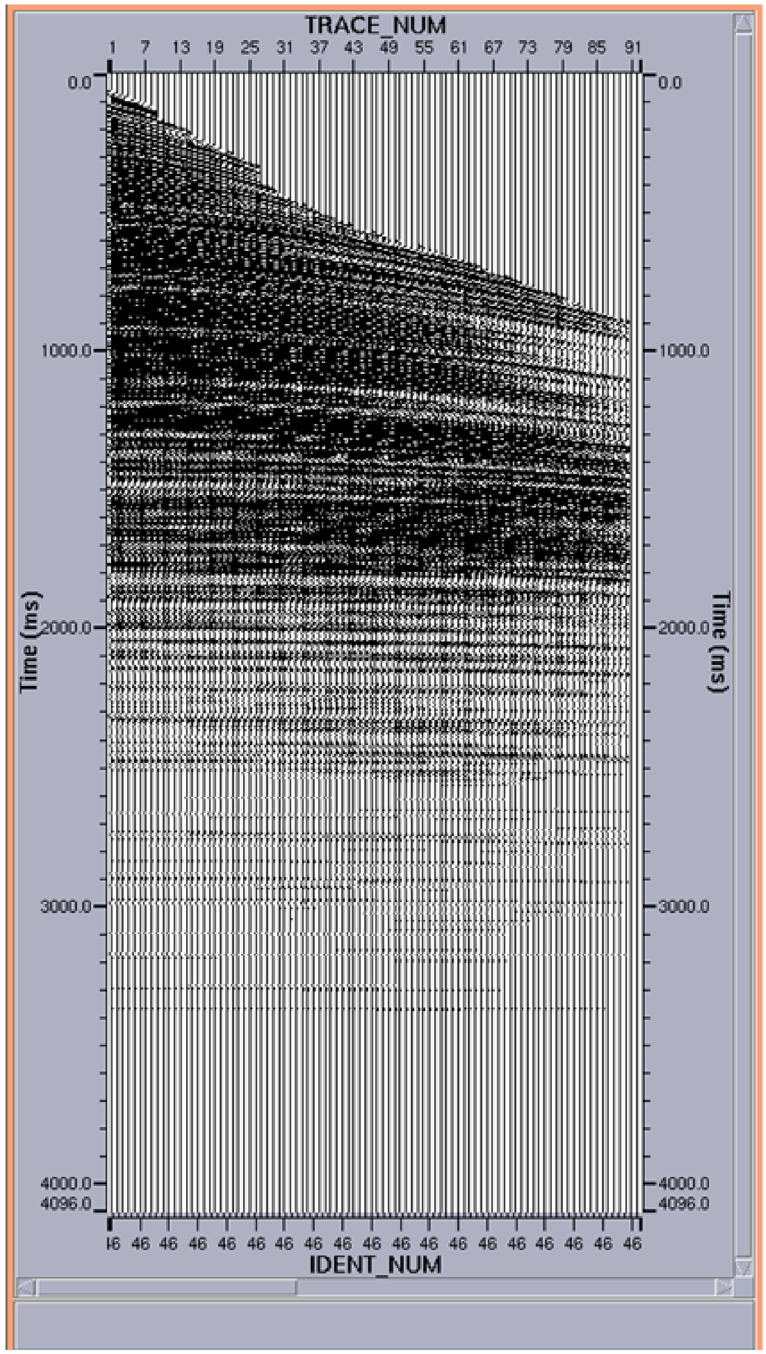

Figure 2.2. A common shot-gather after surface-consistent deconvolution and general bandpass filtering (low-cut = 4 Hz, low-pass = 8 Hz, high-pass = 250 Hz, and high-cut = 375 Hz)

2.4.2 Radon (tau-p) Transform Filter

The radon (tau-p) transform, also known as slant stack or projection (Yilmaz, 1987), is a line integral of some property (e.g. amplitude) of a medium along a specific line (usually a straight line). The radon (tau-p) transform filter is used to suppress multiples. Multiple suppression techniques in radon transform are based on the following characteristics of the multiples: the move-out difference between the primaries and multiples (velocity discrimination); the dip difference between primaries and multiples on the CMP stack; the difference in frequency content between the primaries and the multiples; and the periodicity of multiples (Yilmaz, 1987).

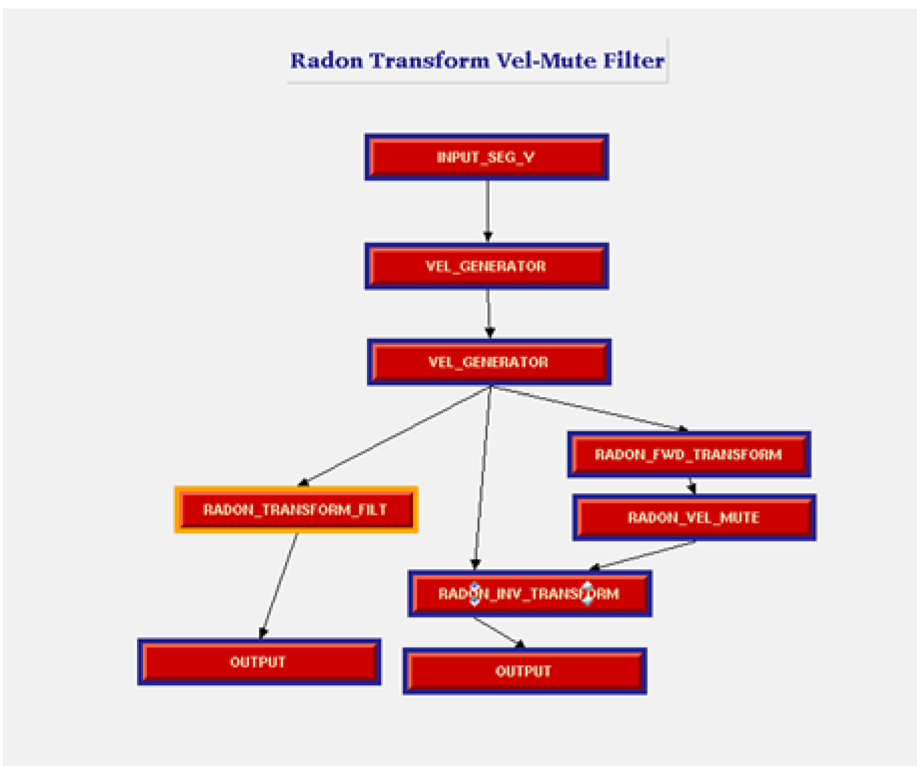

Figure 2.3. Radon transform seismic processing flow module.

2.4.3 Amplitude Balance (Program-Controlled Gain)

Figure 2.4 shows a program-controlled gain (PCG) module, which is a simple type of amplitude balance seismic process (Yilmaz, 1987). In PCG, the envelope, which is the curve drawn by smoothly connecting the adjacent peaks (or troughs) along the trace, is a reliable attribute that describes amplitude decay (Figure 2.5). The PCG function is then the inverse of the trace envelope and is used to balance the trace. In the PCG, tabulated values of time vs. gain value pairs are entered for each selected gather.

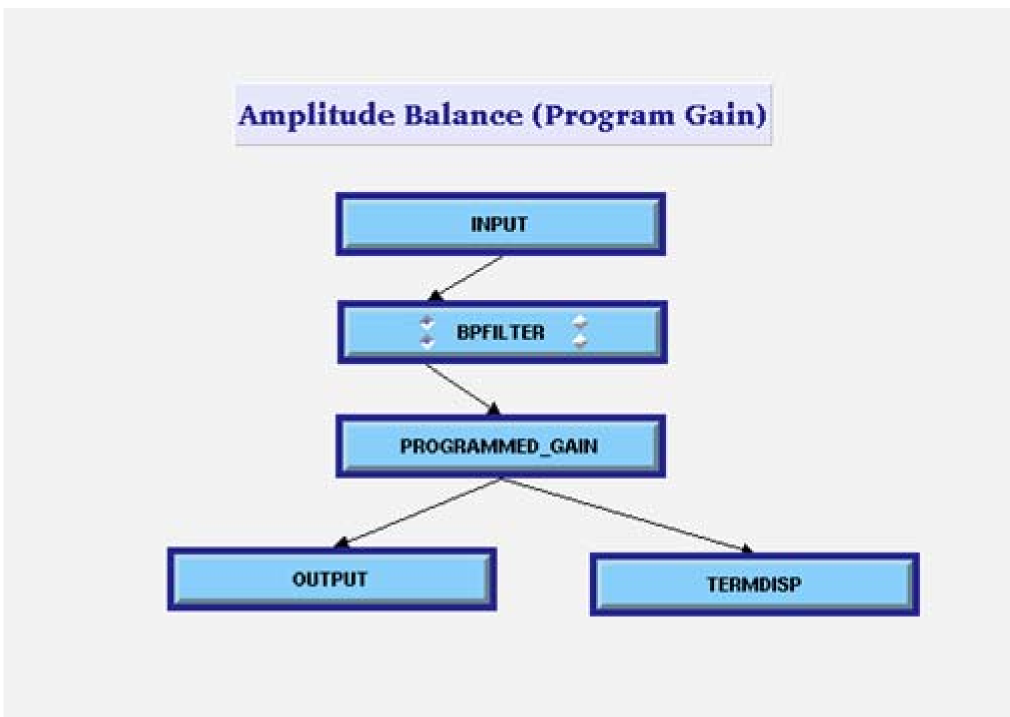

Figure 2.4. Program-Controlled gain seismic flow module.

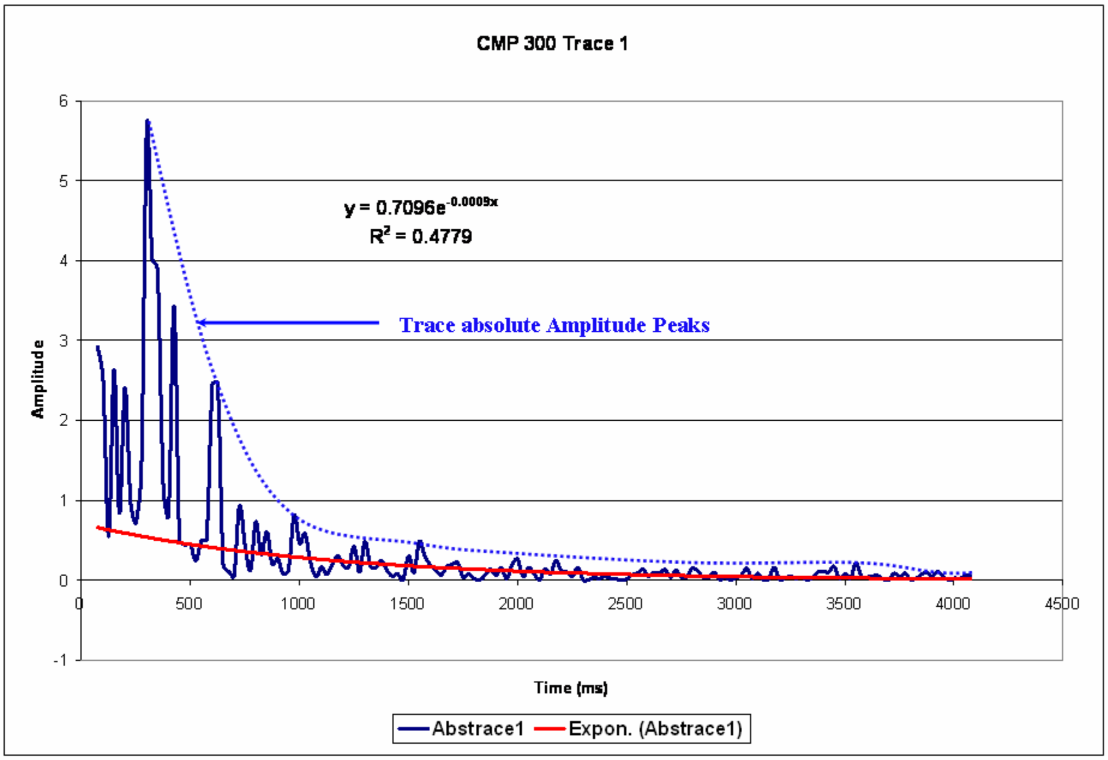

Figure 2.5. Amplitude decay curve for a trace extracted from a CMP-gather (CMP# 300); absolute amplitude values of trace plotted.

2.4.4 Velocity Analysis and Velocity Picking

Velocity analysis on the 2D reflection seismic line from the Red Sea, Yemen, is performed in two steps. The first step is the velocity analysis (VELAN) process (Figure 2.6), and the second step is the interactive velocity picking (IVP) process. The objective of velocity analysis is to generate a velocity file that can be used in the forward modeling process. Both the velocity analysis and interactive velocity picking processes are performed on a CMP-sorted seismic gather. A single velocity function (time versus velocity pair) is derived at selected analysis positions (CMP) along the line. The picked velocities are stored in a file called pick velocity file and used as an input to a script written on MATLAB software. The VELAN process incorporates a data input (INPUT), pick velocity file generator (VEL_GENERATOR), CMP selector for velocity analysis (VELAN_DEFINITION), general purpose band pass filter (BPFILTER), and instantaneous gain (INSTANT_GAIN) processes (Figure 2.6) for data conditioning of the first part. In addition, the VEL_GENERATOR flow in the velocity analysis process consists of two major additional flows, multiple velocity function (MVFS) generation flow and composite gather generation flow. The pick velocity file generation flow is run before the other two flows so that the subsequent two flows can use the pick velocity file. A semblance gather is generated by the composite gather generator flow, while MVFS panel and interactive stack panel are generated by the MVFS generation flow (Figure 2.6).

Finally, the IVP process uses the semblance gather panel (Figure 2.7), the gather panel, the MVFS panel, and the interactive stack panel generated by the (VELAN) process for an on screen velocity picking. Velocity picking is performed on the semblance gather panel (black line with black square boxes) shown in Figure 2.7, while the gather panel, the MVFS panel, and the interactive stack panel serve as guides for the correct velocity picking. The picked velocity file is saved either as a text file or binary file based on the intended use of the velocity file. In addition, the picked velocity file output is a stacking or root mean square (RMS) velocity with time versus velocity pairs given at each selected CMP position. The velocity from this velocity picking is exported into a MATLAB program script for forward modeling.

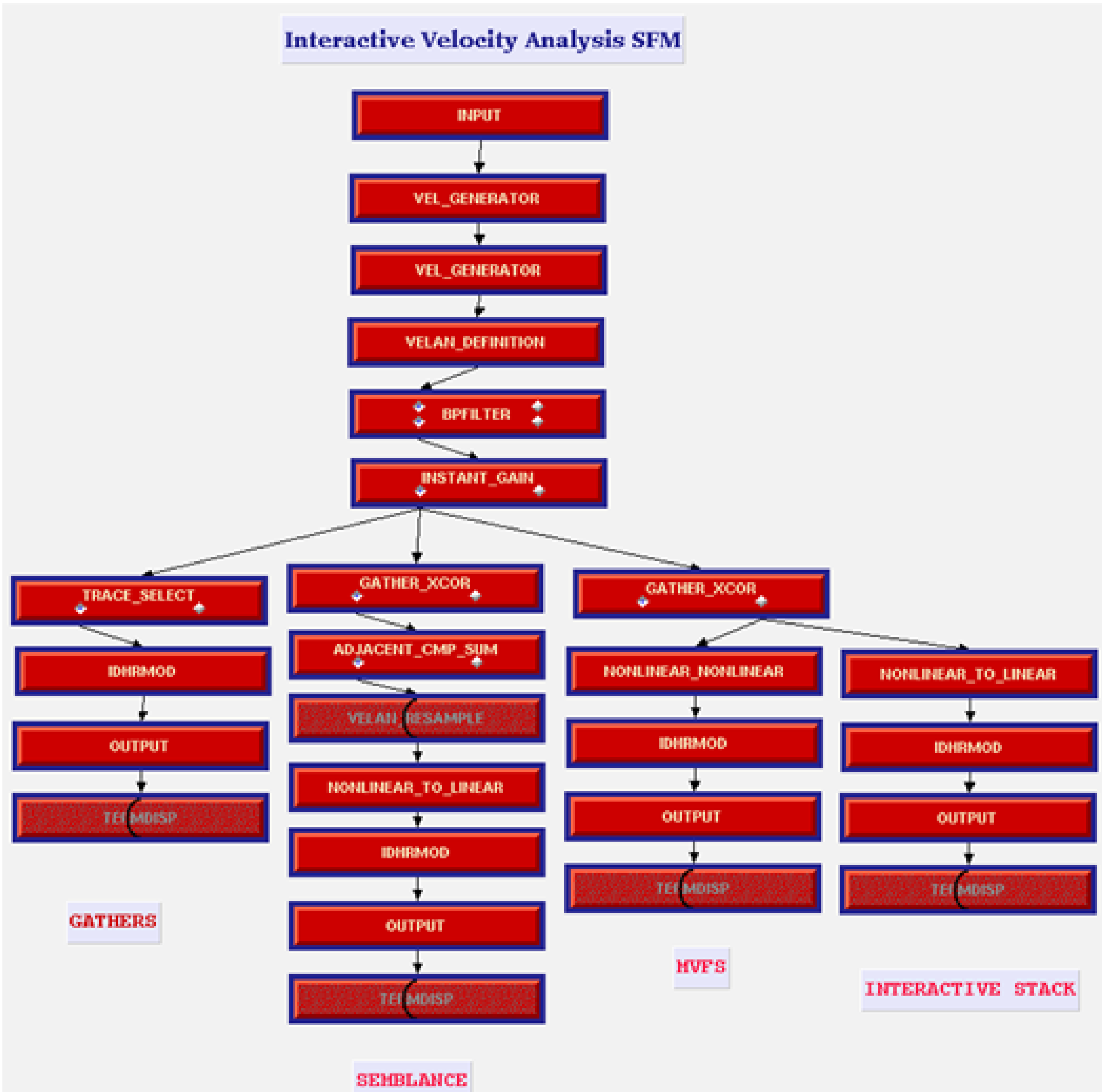

Figure 2.6. Velocity analysis processing (VELAN) flow module, which generates four outputs [Gathers, Semblance, Multiple Velocity Functions (MVFS), and Interactive Stack], which will be used during the interactive velocity picking (IVP) process.

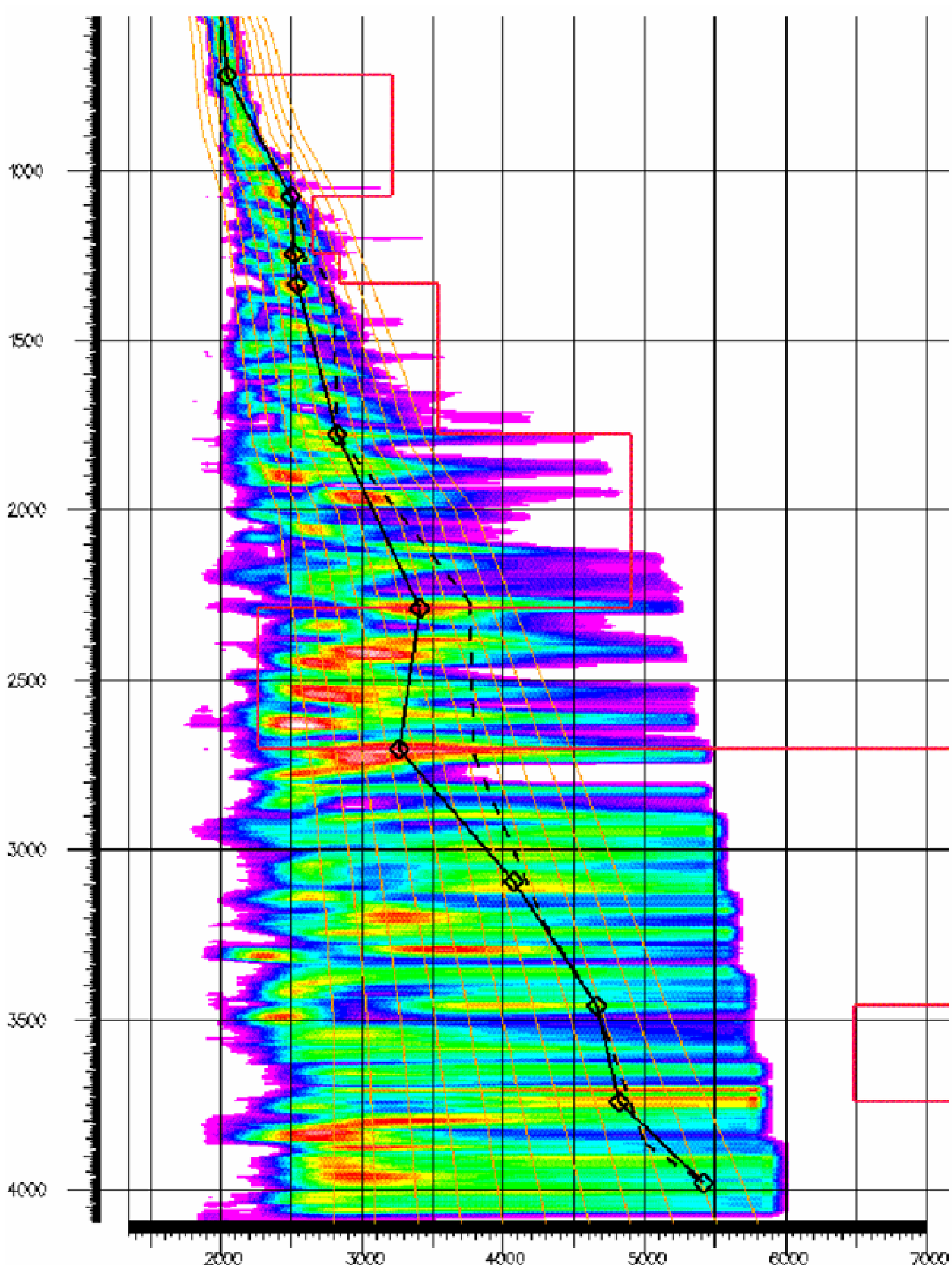

Figure 2.7. Semblance panel with RMS velocity pick (dashed black line = earlier pick and black solid line with diamonds = final pick), and velocity-fan (orange lines) shown.

2.5 Forward Modeling

For the forward modeling written in MATLAB code, an RMS velocity is imported from the velocity picking done on the 2D marine reflection seismic data from the Red Sea, Yemen. The RMS velocity values are converted into interval velocities using the Dix equation (equation 2.1). The calculated interval velocities are used to generate a velocity profile (Figure 2.8a). In addition, the same interval velocity data are used to calculate densities from the empirical density velocity relationship equation 2.2 (Gardner, et al, 1964). Based on the density values obtained earlier, a density log is constructed (Figure 2.8b). However, there are other velocity to density relationships, such as Castagna et al., (1993), which could give better approximation with the proper knowledge of lithology. From the density and velocity values, impedance and reflection coefficient values are calculated using equation 2.3. Then a reflectivity series is constructed (Figure 2.9) using the reflection coefficient values computed. Moreover, by convolving the reflectivity series (Figure 2.9) with a band limited zero-phase wavelet (Figure 2.10) a synthetic trace (seismogram) is generated (Figure 2.11).

Equation 2.1 Interval velocity

$$V_n = \left[\left(\overline{V}_n^2 t_n - \overline{V}_{n-1}^2 t_{n-1}\right) \Big/ \left(t_n - t_{n-1}\right)\right]^{1/2}$$

where $\overline{V}_n^2$ and $\overline{V}_{n-1}^2$ are the stacking velocities from the datum to the reflectors above and below the layer, and t_n and t_{n-1} are reflection arrival times.

Equation 2.2 Gardener Relation

$$\rho_b = 1.741\ V_p^{0.25}$$

where V_p is P-wave velocity in km/sec

Equation 2.3 Reflection coefficient (Normal incident)

$$RC_i = \frac{(\rho_{i+1}V_{i+1} - \rho_i V_i)}{(\rho_{i+1}V_{i+1} + \rho_i V_i)}$$

Equation 2.4 Transmission coefficient

$$TC_i = \frac{2\sqrt{\rho_i V_i \rho_{i+1} V}_{i+1}}{(\rho_i V_i + \rho_{i+1} V_{i+1})}$$

Where ρ_i and ρ_{i+1} are densities of the layers above and below the i_{th} interface respectively, and V_i and V_{i+1} are velocities of the layers above and below the i_{th} interface respectively. RC_i is the reflection coefficient at the i_{th} interface, while TC_i is the two-way transmission coefficient of the i_{th} interface.

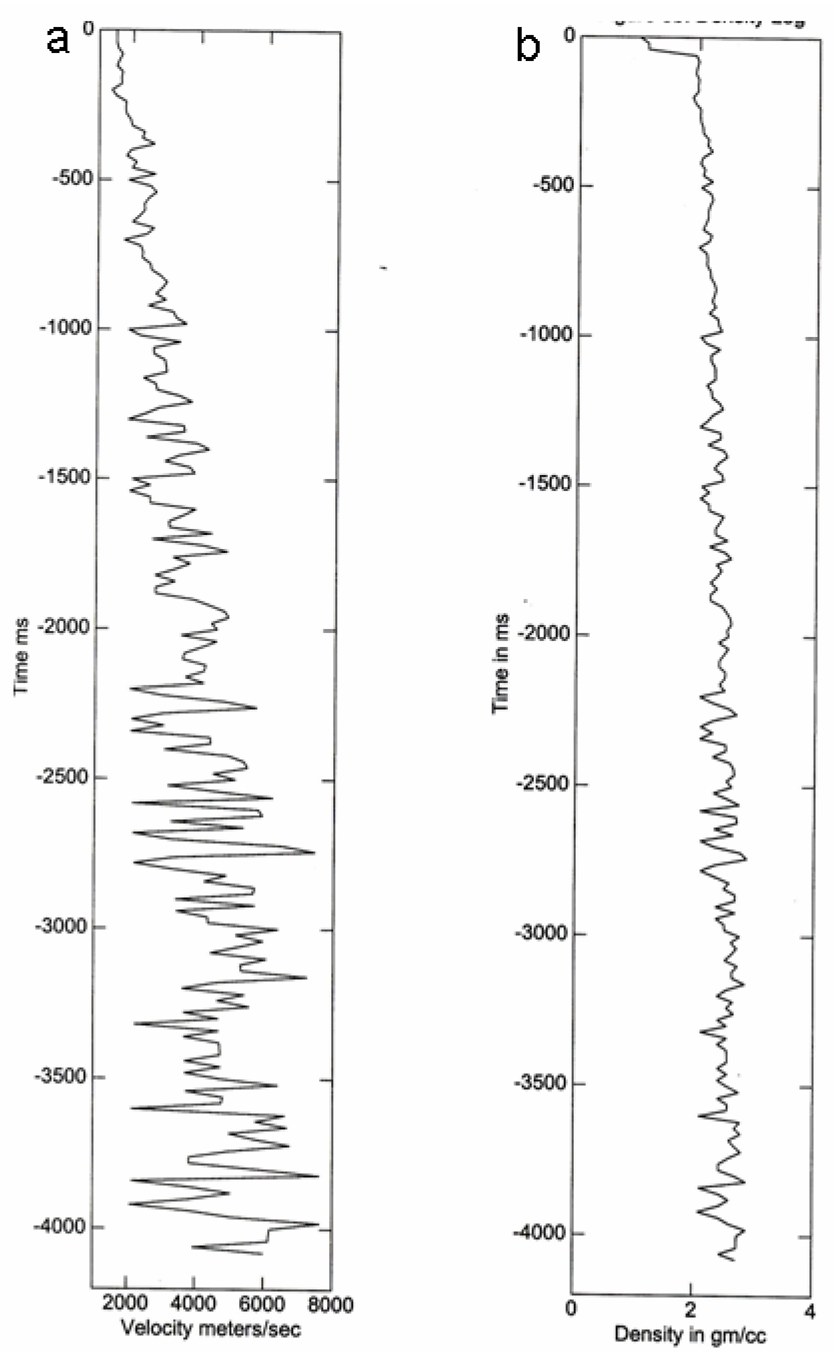

Figure 2.8. a) Velocity profile generated from interval velocities calculated from RMS velocity picks, and b) Density profile generated from calculated density using Gardener rule (Gardener et al., 1964).

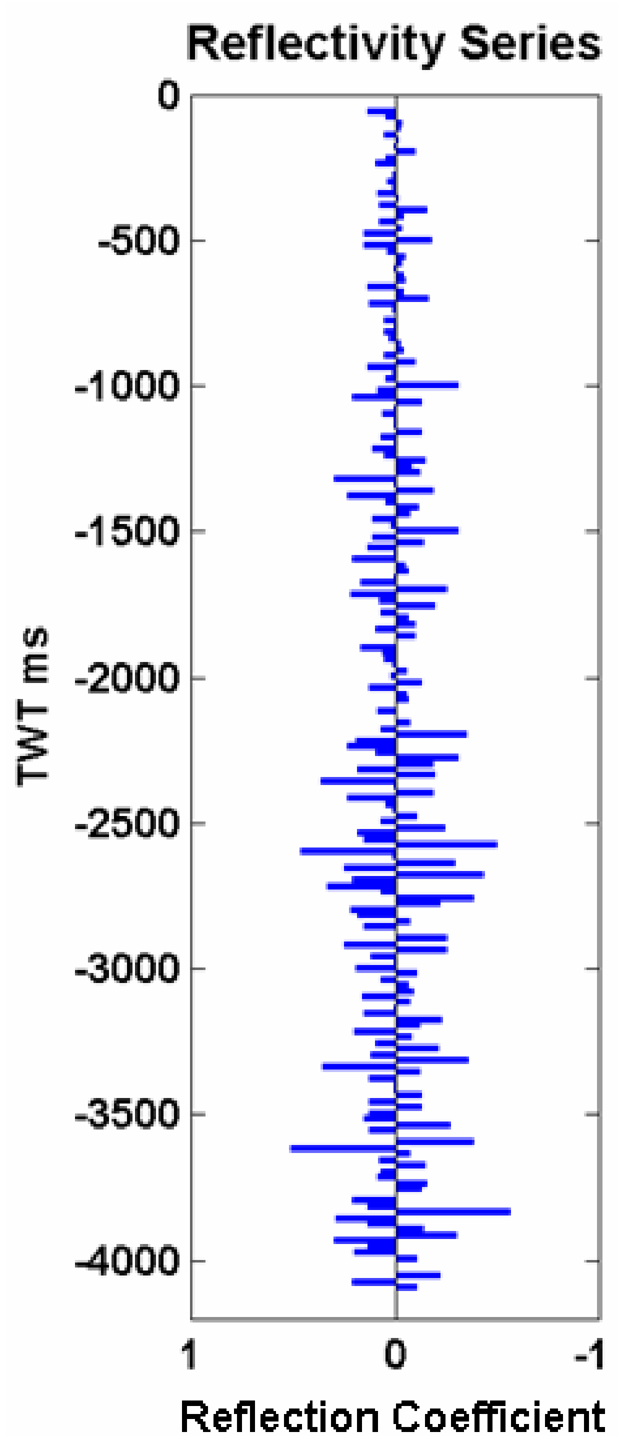

Figure 2.9 Reflectivity series generated from interval velocity and density given in Figures 2.8. a and b.

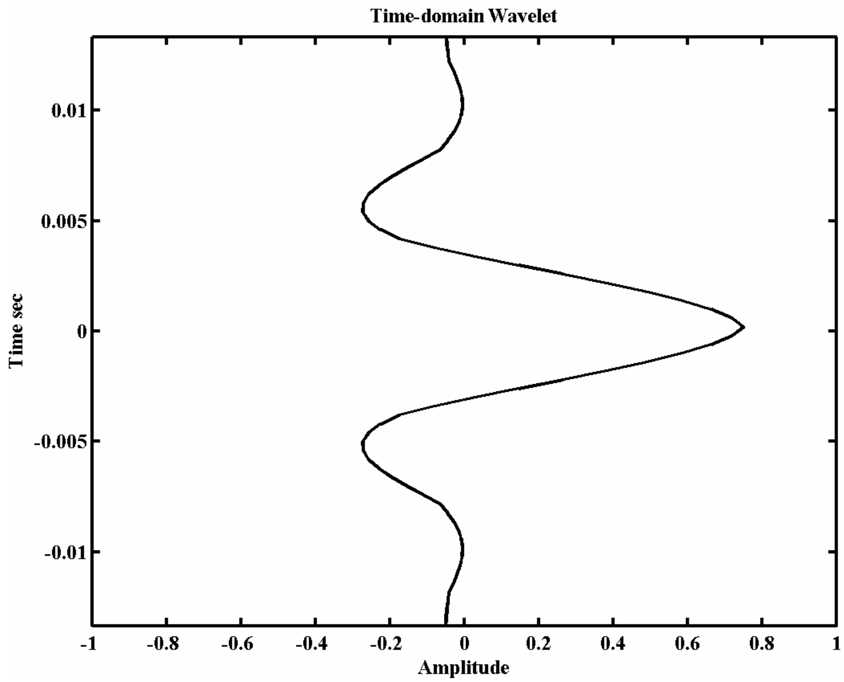

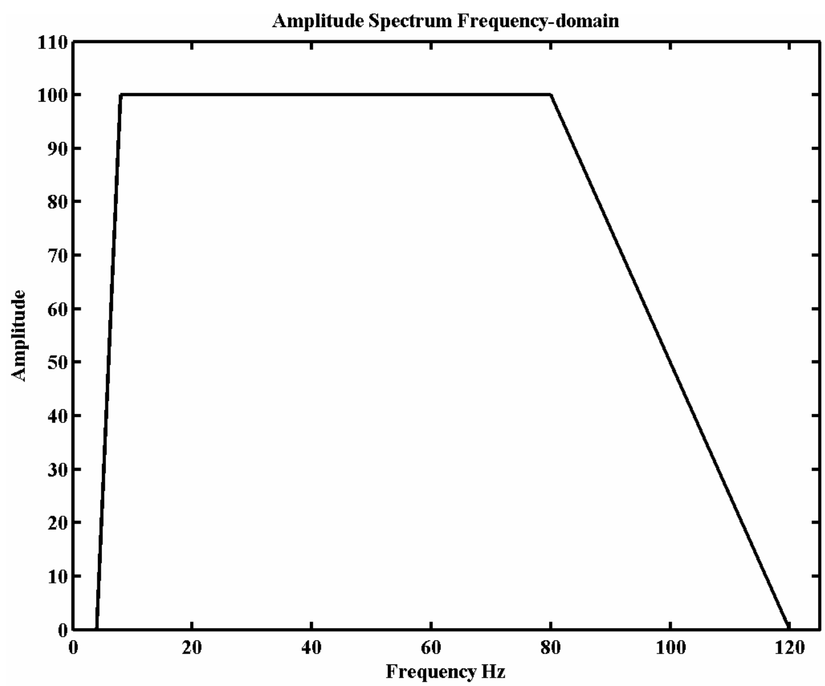

Figure 2.10. Band limited zero-phase wavelet with Lowcut = 4 Lowpass = 8, Highpass = 80 and Highcut = 120 Hz, a) amplitude spectrum in time domain b) amplitude spectrum frequency domain.

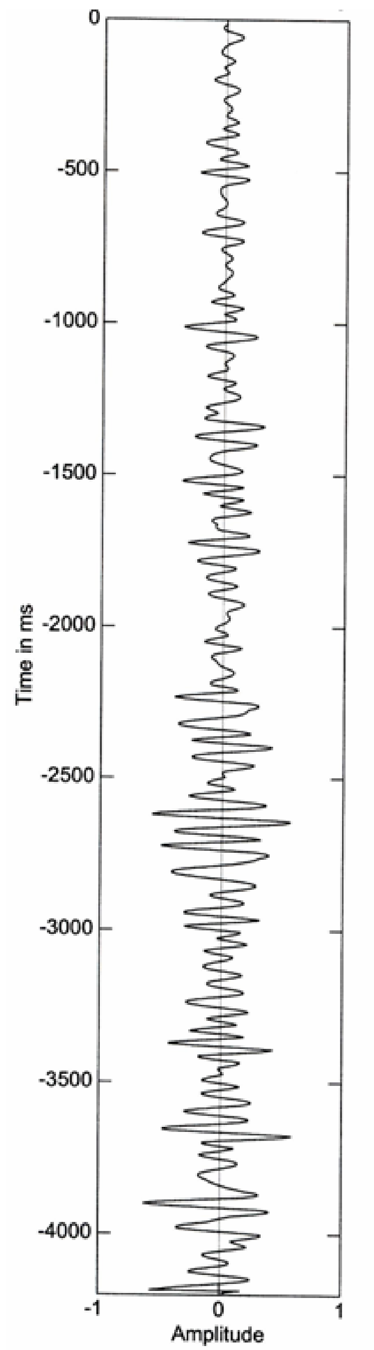

Figure 2.11. Synthetic trace (seismogram) generated by convolving the reflectivity series in Figure 2.9 and the band limited zero-phase wavelet in Figure 2.10 a.

2.5.1 Amplitude Decay due to Spherical Divergence and Transmission Loss

From the calculated reflectivity coefficient, transmission loss is computed using equation 2.5. Next, the radius of the propagating wave from the source is calculated using the two-way time, velocity, and offset distance. Then, amplitude decay due to spherical divergence is calculated from the radius information obtained above and equation 2.6. A plot of this amplitude decay is shown in Figure 2.12. A synthetic seismogram trace plot is generated after amplitude balancing for transmission loss and spherical divergence (Figure 2.13), using program gain control. To compare the effects of transmission loss and amplitude decay due to spherical divergence and transmission loss, Figure 2.14 is shown with both decay terms.

Equation 2.5 Total transmission loss

$$TL = \prod_{i=1}^{n} \left(1 - RC_i^{\ 2}\right)$$

where RC_i is the reflection coefficient at the i_{th} interface.

Equation 2.6 Amplitude decay due to spherical divergence

$$A_r = \frac{A_0}{r}$$

where A_r is the amplitude at distance r from the source, and A_0 is the amplitude at the source position.

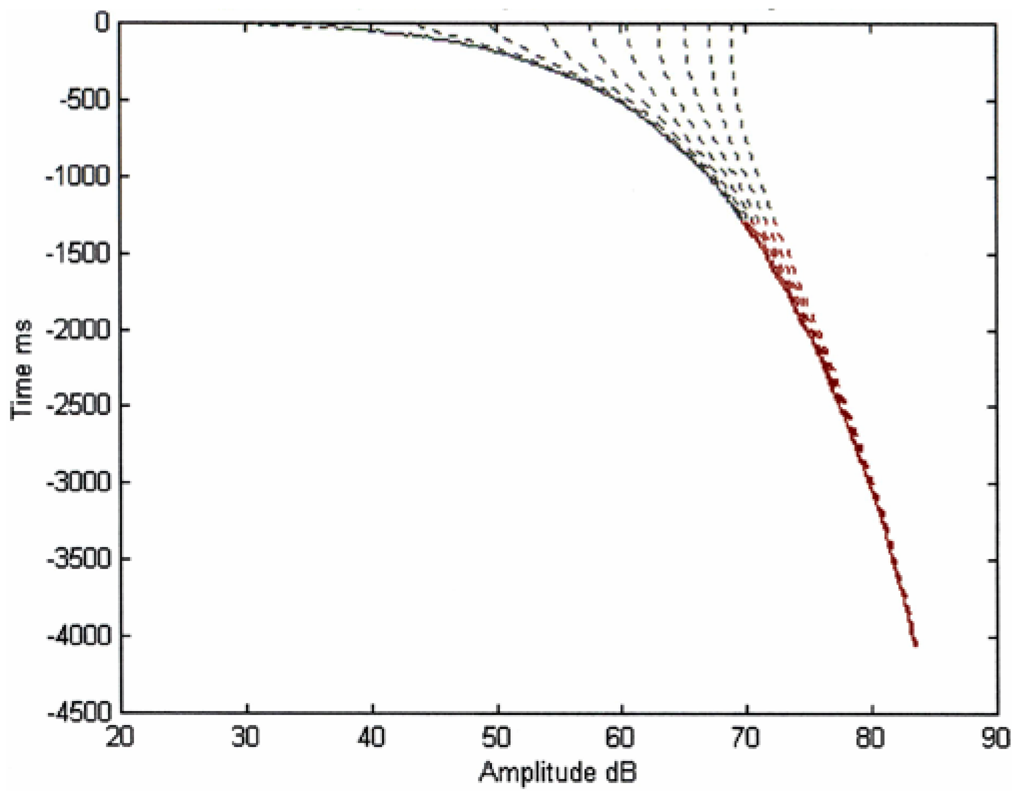

Figure 2.12. Curve for amplitude decay due to spherical divergence for traces with offset between 1000 to 8000 m (MATLAB generated).

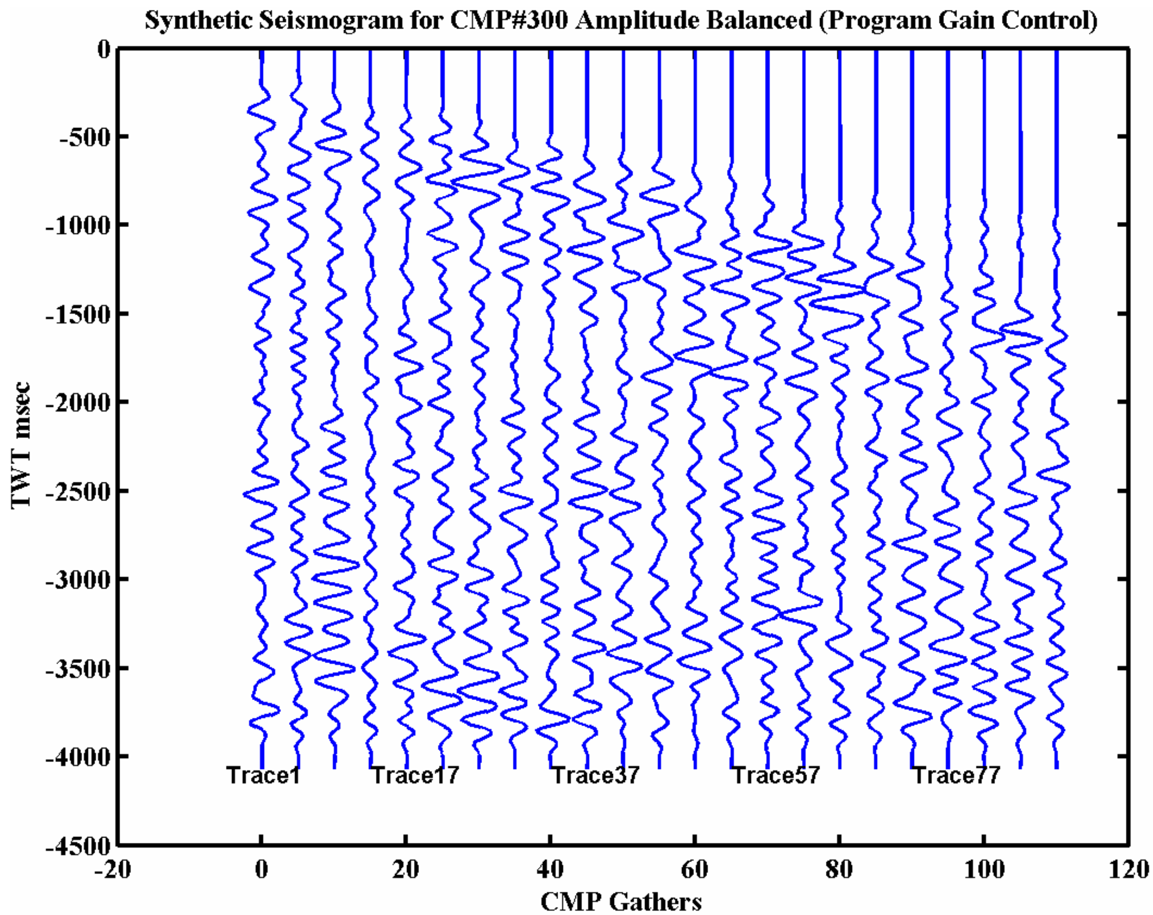

Figure 2.13. Extracted CMP-gather (CMP#300), after amplitude balanced using program controlled gain (PCG).

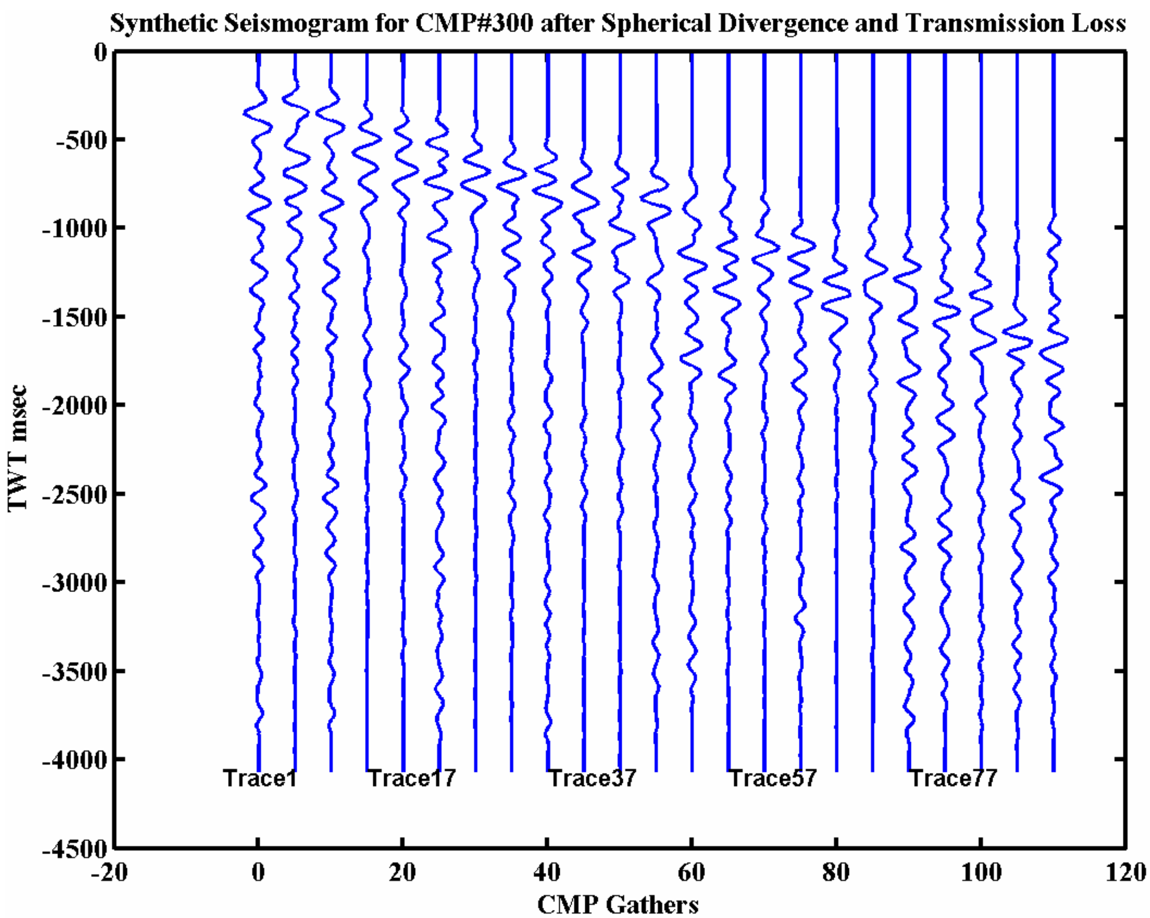

Figure 2.14. Synthetic seismogram for CMP#300, after application of amplitude decay due to spherical divergence and transmission loss to Figure 2.13.

2.5.2 Attenuation due to an Anelastic Property Computation

To characterize the effects of intrinsic attenuation on the synthetic trace (seismogram) of Figure 2.13, variable quality factors (Q) and different offset distances are used to compute the amplitude spectrum of the trace. Results of these computations are shown in Figures 2.15 and 16. A wavelet (Ricker wavelet) amplitude spectrum in terms of frequency can be expressed by equation 2.7 (Zhang and Ulrych, 2002).

Equation 2.7 Amplitude spectrum of a Ricker wavelet

$$A(f) = \frac{2}{\sqrt{\pi}} \frac{f^2}{f_m^2} e^{-f^2 / f_m^2}$$

where f_m is the dominant frequency, and at its initial, the wavelet peak frequency and dominant frequencies are the same. The evolution of the amplitude spectrum through time (t) of the wavelet traveling through an anelastic media with quality factor (Q) is given by equation 2.8 (Futterman, 1962).

Equation 2.8

$$A(f,t) = A(f) e^{-\frac{\pi f t}{Q}}$$

For a single layer with layer quality factor (Q) and wavelet traveling for time t, the amplitude spectrum is given by equation 2.9

Equation 2.9 Amplitude spectrum for wave

$$A(f,t) = A(t)A(f)e^{-\frac{\pi f t}{Q}}$$

where A(t) is an amplitude factor independent of frequency and absorption. Then, we can extend this to multiple layers, and the amplitude attenuation for multiple layers is given by equation 2.10.

Equation 2.10 Amplitude decay for multiple layers

$$A(f,t) = A(t)A(f)\exp\left(\sum_{i=1}^{n} \frac{\pi f \Delta t_i}{Q_i}\right)$$

where Q_i and Δt_i are the quality factors and the travel time in layer i.

The intraval quality factor in a multi-layered section can be calculated using Equation 2.11 (Dasgupta and Clark, 1998)

Equation 2.11 Interval Q from a multi-layer section for

$$Q_i = \frac{[t_n - t_{n-1}]}{\left[\frac{t_n}{Q_n} - \frac{t_{n-1}}{Q_{n-1}}\right]}$$

where t_{n-1} and t_n are the two-way travel time from layer n-1, and layer n and Q_{n-1} and Q_n are the quality factors for the two layers respectively.

2.6 Results and Discussion

Figures 2.15a and b show the effect of varying the quality factor, and the result shows high amplitude decay associated with small quality factor values. In addition, the wavelet bandwidth broadens for the lower quality factor (Q) < 100 values Figure 2.15a. The high frequency component of the wavelet attenuates faster than the low frequency component (Figure 2.15b). Attenuation of the high frequency component has produced stretching in the wavelet Figure 2.15a. Therefore, quality factor (Q) has an inverse effect on amplitude attenuation; the lower the quality factor value the higher the attenuation (Figures 2.15a and b). In the forward modeling the effects of offset distance and travel time were also evaluated. Figures 2.16a and b show there is a direct relationship between travel time plus offset distance and attenuation. As the propagating wave travel time and offset distance increase there is an increased attenuation of the higher frequency component (Figure 16b). There is a direct relationship between offset distance plus and amplitude decay.

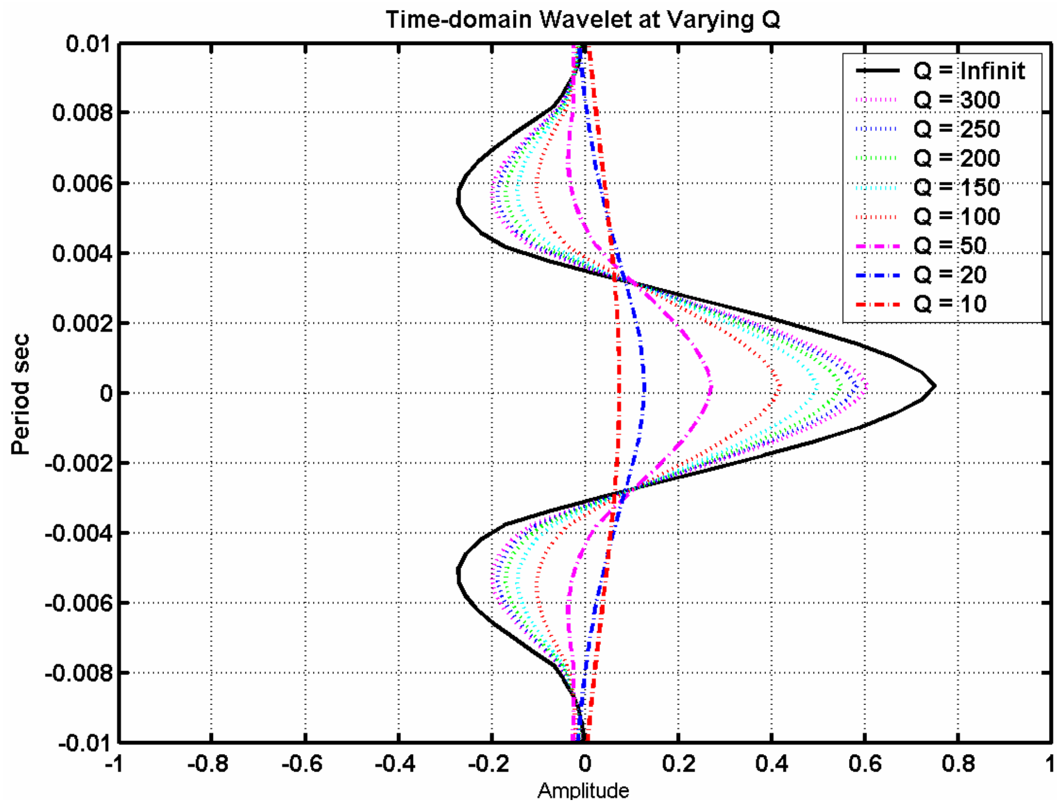

Figure 2.15a. Time domain amplitude spectrum, showing amplitude decay with decreasing Q value, and wave broadening (MATLAB generated).

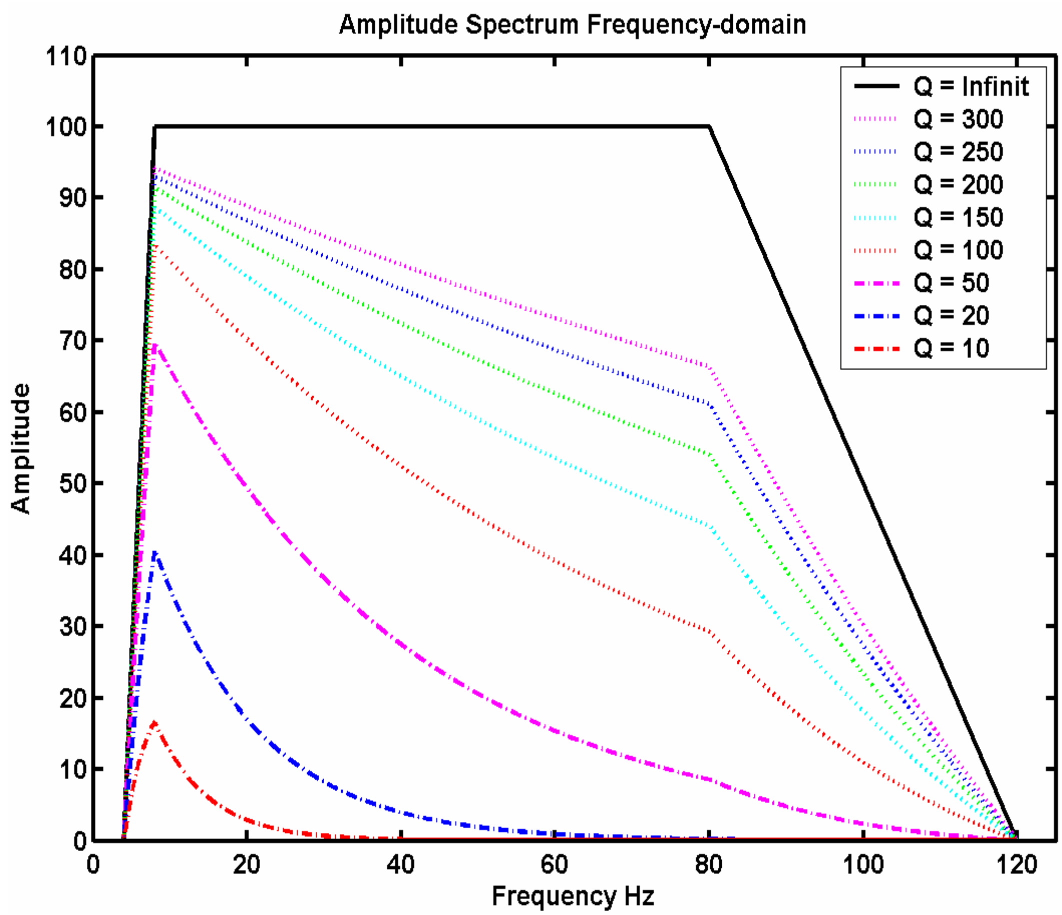

Figure 2.15b. Frequency domain amplitude spectrum, shows amplitude decay with decreasing quality factor value (MATLAB generated).

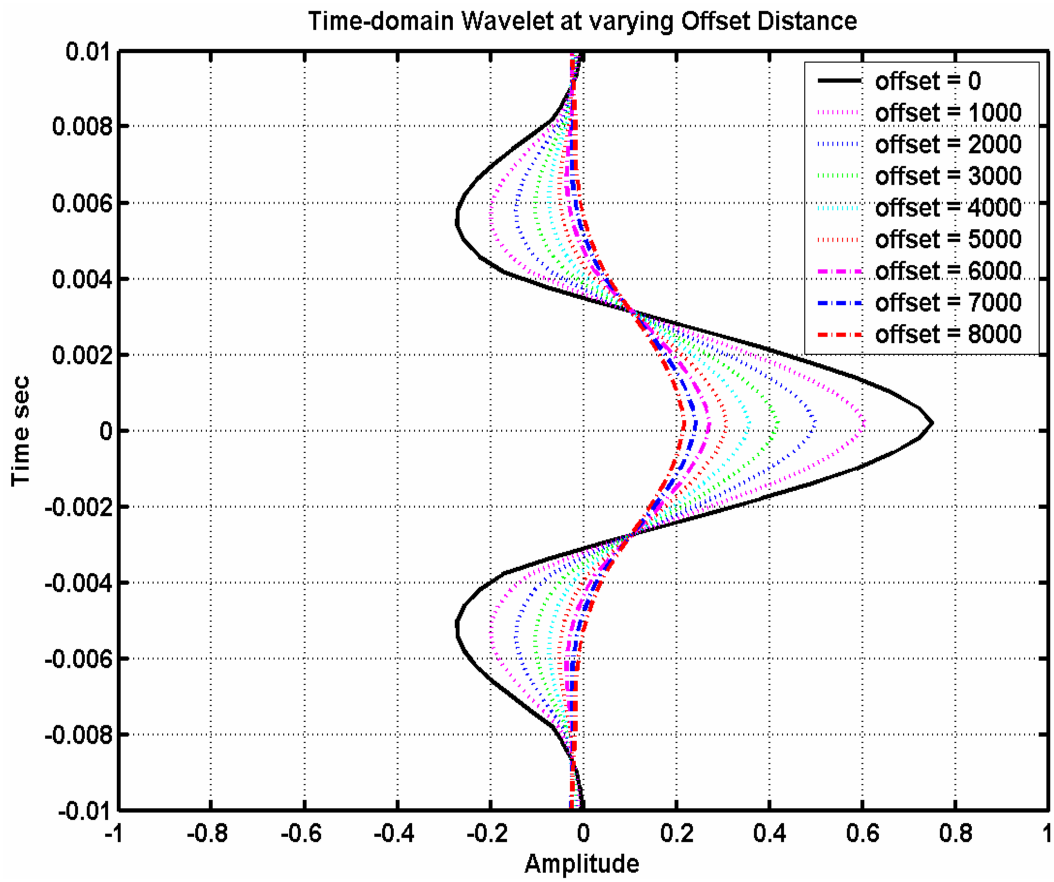

Figure 2.16a. Time domain amplitude spectrum, shows amplitude decay with changing offset distance (MATLAB generated).

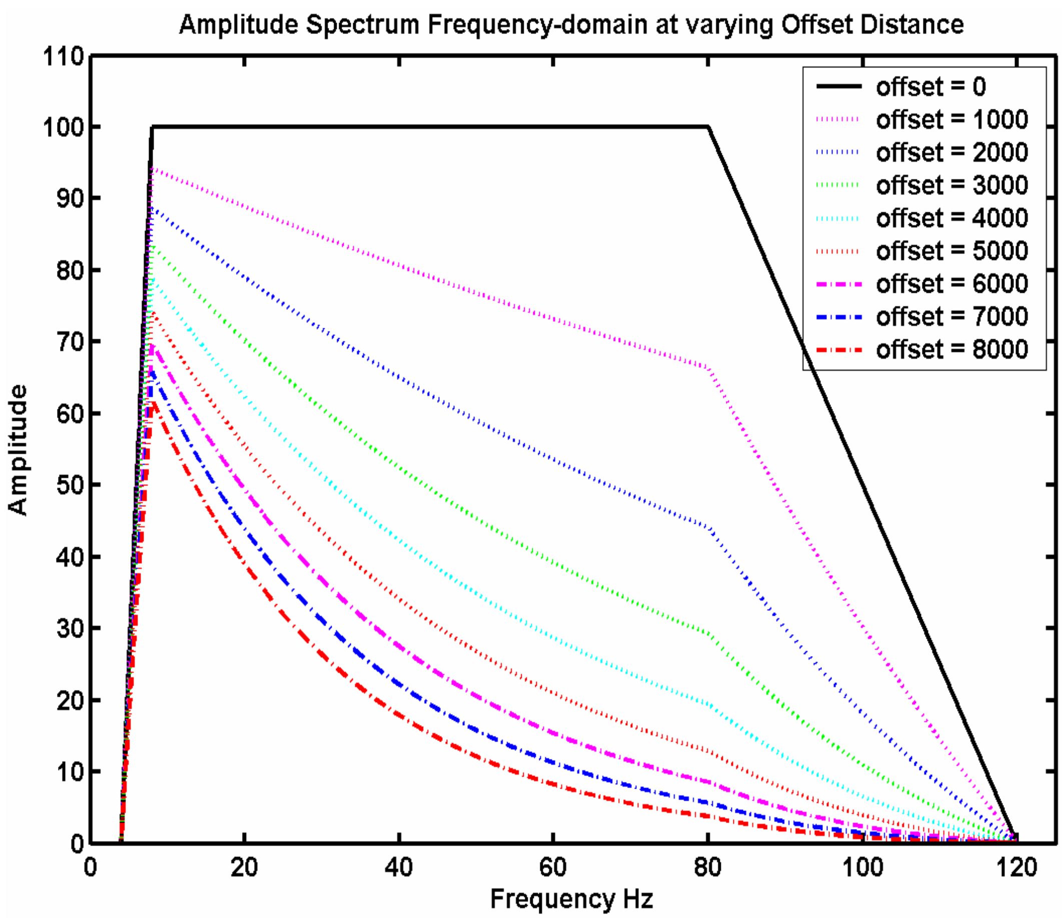

Figure 2.16b. Frequency domain amplitude spectrum, shows amplitude decay with changing offset distance and strong attenuation of the higher frequency components (MATLAB generated).

Figure 2.17 shows effect of interval Q applied to the synthetic seismogram in Figure 2.13. The trace in Figure 2.13 is amplitude balanced removing the effects of spherical divergence and transmission loss. Normal move-out (NMO) correction is applied to the CMP gather before interval anelastic attenuation for Q values = 10, 50 and 100 is applied. Comparison of Figure 2.13 to Figure 2.17 clearly shows presence of significant amplitude decay in the latter. Interval quality factors are applied to the horizons at 1000, 1200, and 2000 ms. The width of the interval is set to 40 to 50 ms. Evidently, these intervals show marked amplitude decay, and the section beneath the intervals shows a similar effect. The effect of the attenuation includes, first, an overall amplitude decay on each trace, as seen in the amplitude decrease from the top going down, and second a significant amplitude decrease at the specific intervals where the attenuation coefficient is large.

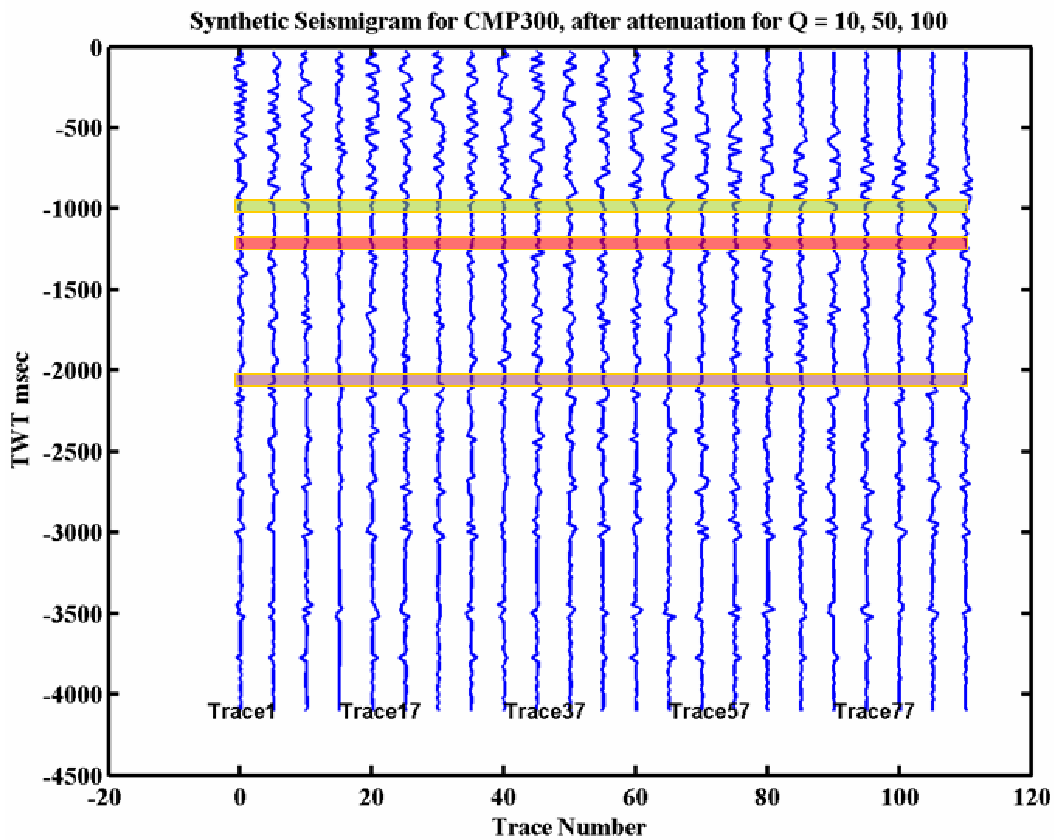

Figure 2.17 Synthetic trace of CMP#300, after amplitude decay due to an anelastic attenuation for Q = 10, 50 and 100. Q = 10 corresponds to light yellow, Q = 50 corresponds to light red, and Q = 100 corresponds to light magenta (MATLAB generated).

2.7 Summary and Conclusions

The layered Earth attenuates part of the propagating seismic wave energy by converting it to heat energy due to friction. Amplitude decay of the propagating wave through the earth layer is frequency dependent. In addition, attenuation depends also on the type of lithology, physical state, amount of pore volume, and degree of saturation. This attenuation is the intrinsic attenuation, which only depends on the above mentioned layer properties. The intrinsic attenuation is inversely related to the quality factor (Q), which is the measure of the energy dissipation per cycle of peak energy. Understanding the attenuative character of the Earth will help to characterize a layer, its constituents and its physical state. From this work, first one can see the effects of intrinsic attenuation on a reflection seismic. Second, the quality factor can be calculated for a pre-stack CMP gather from the power amplitude spectrum of selected horizons Equation 2.11. Third, the interval quality factor can be computed using Equation 12.12, which subsequently can be used to filter the whole seismic section by inverse Q filtering. Therefore, in conjunction with velocity information and other physical measurements we have observed attenuation can be used to characterize lithology and its contents on a reflection seismic section.

Before one attempts to apply this model to seismic, it is necessary to investigate the scale effects of the propagating wave, which will be discussed in the following chapter.

Chapter 3

COMPUTATIONAL AND EXPERIMENTAL INVESTIGATION OF SCALE EFFECT IN LAYERED MEDIA FOR 1D CASE

3.1 Introduction

Since reflection seismic provides information on a much larger scale than petrophysics, it behooves as to investigate scale effects. In general rocks exhibit compositional heterogeneity at different scales. In particular sedimentary rocks owing to their layering display pronounced directional heterogeneity. These variations are in mineralogical, petrological, and structural properties, to name a few. In addition, these heterogeneities affect rock properties such as elasticity, velocity, porosity, permeability, and pore-pressure. The scale of layering and heterogeneity that can be imaged and interpreted is directly related to the scale of the wavelength of the propagating wave through the medium. For a wave much larger than the layer thickness ($\lambda/d >> 1$) the medium is known to behave like a homogeneous or nearly homogeneous transversely isotropic (effective) medium (Backus, 1962), whose properties, such as densities are average densities and the elastic property coefficients are algebraic combinations of averages of the elastic properties (Backus, 1962; Mukerji et al., 1995). However, for a medium which has wavelength to layer ratio (λ/d) << 1, the layers behave as individual entities and the heterogeneous medium may be treated as a piecewise homogeneous medium with velocities that are faster than the effective medium. The pulse transmission technique, where a plane wave is propagated through a medium held between source and receiver transducers, is used for this experiment. The samples in this test are composite samples made up of layered stacks of aluminum and acrylic disks. The disks have different thickness, and the total thickness is 36.61 mm. However, the disks have the same diameter of 25.4 mm. The tests were run at different frequencies ranging between 125 kHz and 750 kHz. In this investigation factors such as constituent fraction, layer thickness, wavelength, and frequency are considered. The scale of heterogeneity and stratification that can be imaged and interpreted seismically affects wave propagation. The proper understanding of the scale effect in this experiment will help us extend our knowledge of the relationship between heterogeneity, velocity, and elastic parameters in a complex layered geology. Therefore, proper interpretation and imaging of these scale dependent variations and their relation to wave propagation play a significant role in seismic exploration and reservoir geophysics.

3.2 Objectives

The purpose of this work is to study the relationship between scale of heterogeneity and wavelength, and their effect on plane wave propagation, velocity dispersion, and waveform distortion in a layered medium. Based on the observations made the study will propose methods to compute velocity and elastic parameters. We will try to answer these questions:

What scale of heterogeneity will cause velocity dispersion and waveform distortion?

How thin is a layer to be summed into one composite unite?

What happens to the wave and its velocity between the two bounding limits?

3.3 Theoretical Background

There have been numerous theoretical, computational and experimental studies concerning wave propagation in stratified media (Postma, 1955; Backus, 1962; Sun et al, 1968; O' Doherty and Anstey, 1971; Scheonberger and Lavin, 1974; Berryman, 1979; Helberg, 1984; Malia and Carlson, 1984; Carcione et al, 1991; Mukerji et al., 1995 and Mavko et al, 1998). The majority of these studies can be grouped us either effective medium theory or ray theory. In the long wavelength limit case, theoretical and experimental results indicate when the wavelength is much larger than the layer thickness ($\lambda/d >> 1$), the medium behaves as a homogeneous transversely isotropic media (Postma 1955; Backus, 1962; Mukerji, 1995 and Mavko et al., 1998). Velocity for the equivalent isotropic medium is given by equation 3.1.

Equation 3.1 Equivalent Effective Medium

$$\frac{1}{\rho_{ave} V_{EMT}} = \sum_k \frac{f_k}{\rho_k V_k^2},$$

and $\rho_{ave} = \sum_k f_k \rho_k$

where f_k,ρ_k, and V_k are the volume fractions, densities, and velocities.

In the short wavelength limit case, when the wavelength is much smaller than the layer thickness, each layer of the medium behaves as an individual entity, and the medium can be treated as a piecewise medium (Mavko et al., 1998). In the short wavelength limit there is velocity dispersion due to multiple scattering effects, and the velocity through the medium is given by equation 3.2

Equation 3.2 Velocity for the short wavelength limit (Ray theory)

$$\frac{1}{V_{RT}} = \sum \frac{f_k}{V_k}$$

3.4 Ray Theory and Effective Medium Case

Waves propagating in a layered medium undergo attenuation and velocity dispersion caused by multiple scattering at the layer interface (Aki and Richards, 1980; Frazer, 1994, Mavko et al., 1998). For a wave propagating in a stratified media made up of two components that have phase velocities V_1 and V_2, densities ρ_1 and ρ_2, and thickness d_1 and d_2, dispersion ratio can be found from the well known Floquet solution equation 3.3 (Mavko et al, 1998)

Equation 3.3 Floquet Solution for Velocity Dispersion in two component medium

$$\cos\left[\frac{\omega(d_1+d_2)}{V}\right]=\cos\left(\frac{\omega d_1}{V_1}\right)\cos\left(\frac{\omega d_2}{V_2}\right)-\chi\sin\left(\frac{\omega d_1}{V_1}\right)\sin\left(\frac{\omega d_2}{V_2}\right)$$

where $\chi=\dfrac{(\rho_1V_1)^2+(\rho_2V_2)^2}{2\rho_1\rho_2V_1V_2}$

If the spatial period $d_1 + d_2$ is an integer multiple of one-half the wavelength, multiple reflections are in phase and add constructively, resulting in a large total accumulated reflection (Figure 3.4a). The frequency at which this Bragg scattering condition is satisfied is called Bragg frequency (Mavko et al., 1998).

In a layered media the effective phase slowness (inverse phase velocity) of the propagating wave depends on the relationship of thickness of the layers and the wavelength of the propagating wave. The effective phase slowness (1/velocity) can be expressed by equation 3.4 (Frazer, 1994; Mavko et al., 1998), S_{rt} is the ray theory slowness of the direct ray which does not undergo any reflection. Its value is the thickness-weighted average of individual layers. However, the S_{st} (stratigraphic slowness) results from multiple scattering within the layers. Kennett's (1974) invariant imbedding formulation for the transform function of a layered medium laid the basis for calculating the effective slowness and travel time (Figure 3.1). In addition, in the above method the response of a layered medium is generated by iteratively adding one layer at a time. The transmission coefficient of the added layer can be given by equation 3.5.

Equation 3.4 Effective Phase Slowness

$S_{eff} = S_{rt} + S_{st}$

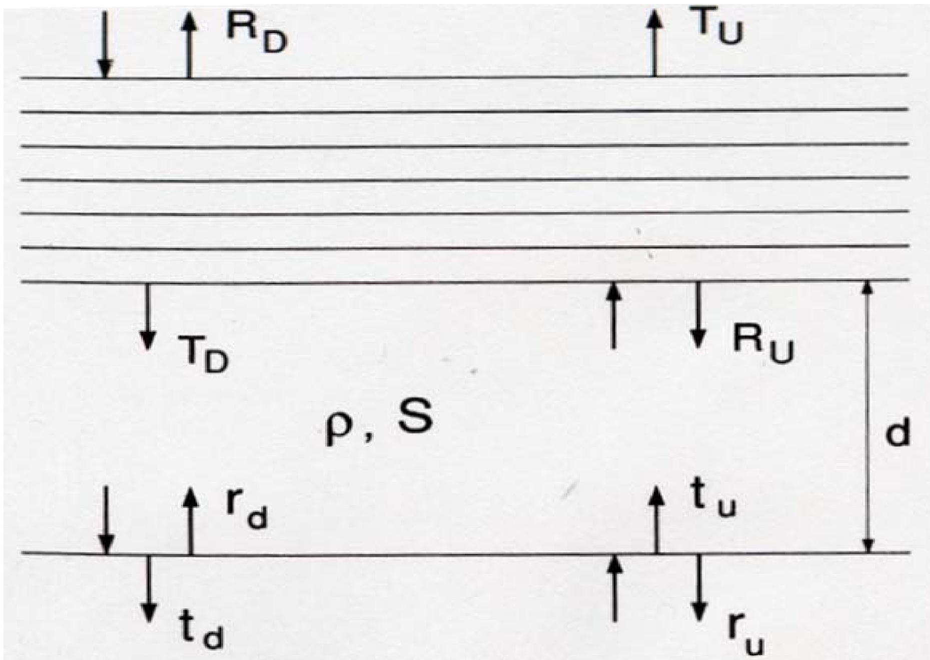

Figure 3.1 Kennett, 1974, Layer imbedding method, Frazer, 1994.

Equation 3.5 Transmission Coefficient of the added layer

$$T_D' = t_d\theta\left(1 - R_U\theta^2 r_d\right)T_D$$

where r_d, t_d, r_u and t_u are the up and down going reflection and transmission coefficients at the lower interface of the added layer (Figure 3.1), and $\theta = \exp(i\omega dS)$. For a complete stack of N layers the total transmission coefficient (T_D) is given by equation 3.6.

Equation 3.6 Transmission Coefficient for the complete stack of layers.

$$T_D = \prod_{n=1}^{N} t_d^n \theta^n \left\{1 - R_U \left[\theta^n\right]^2 r_d^n\right\}^{-1}$$

This can be expanded to equation 3.7 to show the intrinsic and stratigraphic parts.

Equation 3.7

$$T_D = \left[\prod_{n=1}^{N} \theta^n\right]\left[\prod_{n=1}^{N} t_d^n \left\{1 - R_d^n \left[\theta^n\right]^2 r_d^n\right\}^{-1}\right]$$

The first part of equation 3.7 is the intrinsic transmission operator for the particular layer in the stack of layers, and for large number of layers it has the value $\exp(i\omega DS_{in})$, where D is the thickness of the total stack and S_{in} is given by equation 3.8.

Equation 3.8 Intrinsic Transmission

$$S_{in} = \frac{S_1\langle d_1\rangle + S_2\langle d_2\rangle}{\langle d_1 + d_2\rangle}$$

where $\langle d_1 \rangle and \langle d_2 \rangle$ are the average thickness of the mean thicknesses of the two component medium. The second part of equation 3.7 is the stratigraphic filter exp(iωDS$_{st}$), where by it is given as equation 3.9

Equation 3.9 Stratigraphic Filter

$$\exp((i\omega DS_{st}) = \left[\prod_{n=1}^{N} t_d^{(n)} \left\{1 - R_U^{(n)} \left[\theta^{(n)}\right]^2 r_d^{(n)} \right\}^{-1} \right],$$

and taking the log of both sides, the stratigraphic filter expression gives by equation 3.10.

Equation 3.10 Stratigraphic Filter

$$S_{st} = \frac{1}{i\omega D} \sum_{n=1}^{N} \ln \left[t_d^{(n)} \left\{1 - R_U^{(n)} \left[\theta^{(n)}\right]^2 r_d^{(n)} \right\}^{-1} \right]$$

For a two component medium that has total thickness D, and layers with slowness (1/velocity) density, and thickness Si, ρi and di respectively.

3.5 Sample Preparation

Cylindrical samples of aluminum and acrylic disks were cut to different thicknesses to generate layers of various sizes, and then stacked alternatively to simulate a 1D layered medium for velocity analysis and elastic property measurements. The samples were prepared at Department of Physics and Astronomy laboratory, the University of Oklahoma. The individual disk length ranges from 1.395

mm to 11.16 mm for the acrylic, and from 3.181 mm to 25.45 mm for the aluminum. Based on the velocities (Table 3.1) of the two materials and the frequencies at which the measurements were run, the disk lengths range from 1/16th of the calculated wave length (λ) at 125 kHz to 3 times the calculated λ at 750 kHz (Table 3.2). The sample top and bottom surfaces were polished using 400 fine-grade sandpaper, to get a good coupling between the sample and transducer.

Material	Density (g/cc)	P-wave Vel. (m/s)	S-wave Vel. (m/s)	Wavelength (λ) mm @ 500 kHz		Impedance (g/cc)(m/s)
				P-wave	S-wave	P-wave
Acrylic	1.18	2730	1430	5.58	1.144	3221.4
Aluminum	2.69	6260	3080	12.725	2.464	16839.4
Titanium	4.5	6070	3310	4.856	2.648	27315

Table 3.1 Published material properties for acrylic, aluminum and endcaps (Titanium).

3.6 Experimental Procedure

This experimental work is geared toward understanding the interdependence between seismic wavelength (λ) and layering thickness (d) during seismic parameters measurement. It also tries to determine λ/d values that bound the long wavelength limit and the short wavelength limit. More importantly, this work attempts to demonstrate the effect of λ/d on reflection coefficient at layer interfaces.

Samples of aluminum and acrylic disks were used to simulate 1D stratified media. The aluminum and acrylic disk lengths were varied. In addition, experiments were done at several frequencies ranging from 125 kHz to 750 kHz. Choice of sample length was made based on published sound velocity values for aluminum and acrylic (Table 3.1), and the dominant frequency at which the measurements were done. Length of the aluminum disks range from 3.182 mm to 25.45 mm, while the acrylic disks ranged from 1.395 mm to 11.16 mm. This will generate a λ/d ratio ranging from 16 at 125 kHz to 0.333 at 750 kHz per disk. The compressional (P) wave, and two orthogonal shear (S1 and S2) wave velocity measurements were made on stacked alternating layers of acrylic and aluminum disks with a total thickness of 36.61 mm (figure 3.3a and 3.3b). Compressional and shear wave transducers, placed at both ends of the stack measure propagation velocity in three directions, one perpendicular, and two horizontal to the layering. The sample is placed in an impermeable jacket which also incased the two endcaps. A firm contact between sample and endcaps is achieved by applying sufficient pressure during sample mounting.

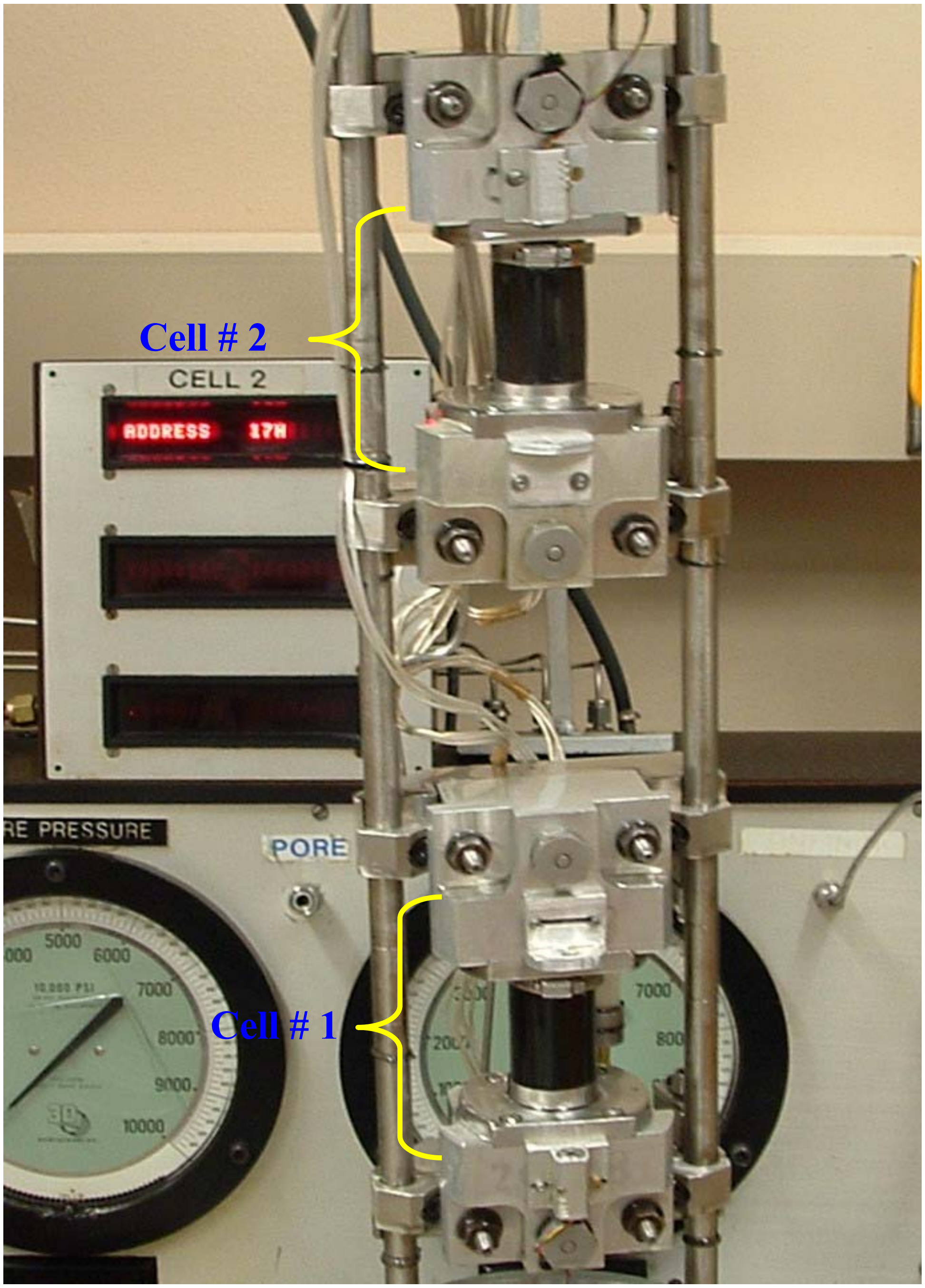

Figure 3.2 Ultrasonic pulse transmission velocity measurement assembly, showing two samples mounted at cell#1 and cell#2.

Sample Type (Thickness (*d*) mm)	**Sample Vel. (m/sec)**	**Frequency (kHz)**	**Wavelength to thickness ratio (λ/d)**
Acrylic (1.395)	2730	125	16
Acrylic (2.790)	2730	125	8
Acrylic (5.58)	2730	125	4
Acrylic (11.16)	2730	125	2
Aluminum (3.181)	6270	125	16
Aluminum (6.362)	6270	125	8
Aluminum (12.724)	6270	125	4
Aluminum (25.45)	6270	125	2
Acrylic (1.395)	2730	250	8
Acrylic (2.790)	2730	250	4
Acrylic (5.58)	2730	250	2
Acrylic (11.16)	2730	250	1
Aluminum (3.181)	6270	250	8
Aluminum (6.362)	6270	250	4
Aluminum (12.724)	6270	250	2
Aluminum (25.45)	6270	250	1
Acrylic (1.395)	2730	500	4
Acrylic (2.790)	2730	500	2
Acrylic (5.58)	2730	500	1
Acrylic (11.16)	2730	500	0.5
Aluminum (3.181)	6270	500	4
Aluminum (6.362)	6270	500	2
Aluminum (12.724)	6270	500	1
Aluminum (25.45)	6270	500	0.5
Acrylic (1.395)	2730	750	2.667
Acrylic (2.790)	2730	750	1.333
Acrylic (5.58)	2730	750	0.667
Acrylic (11.16)	2730	750	0.333
Aluminum (3.181)	6270	750	2.667
Aluminum (6.362)	6270	750	1.333
Aluminum (12.724)	6270	750	0.667
Aluminum (25.45)	6270	750	0.333

Table 3.2 Computed wavelength to thickness ratio (λ/d) of acrylic and aluminum disks

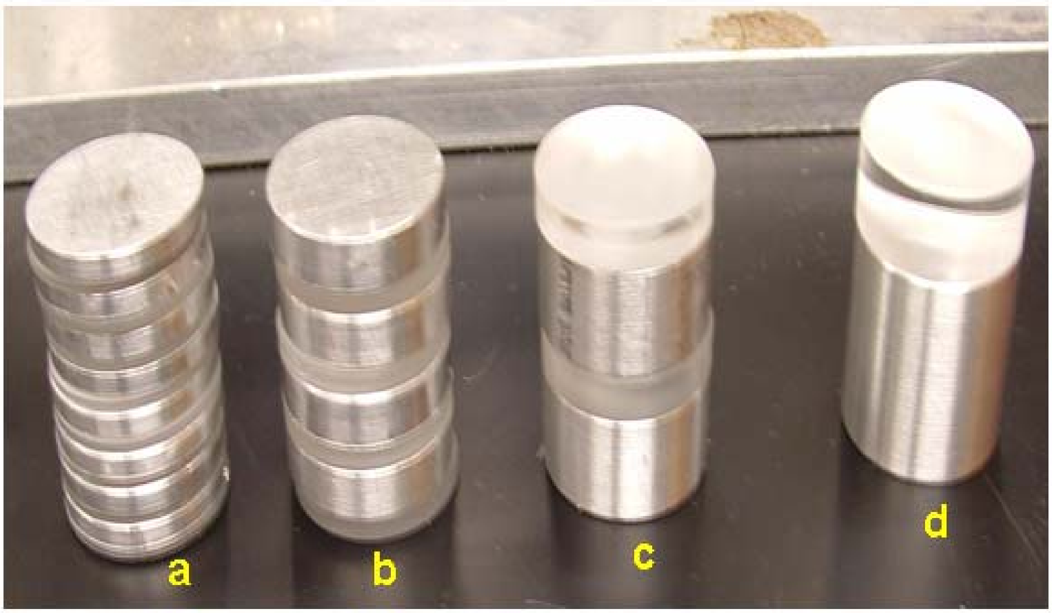

Figure 3.3a Single alternating acrylic and aluminum disk stacks a) 16 disks stack layers (λ/ d = 16 at 125 kHz), b) 8 disks stack (λ/ d = 8 at 125 kHz), c) 4 disks stack (λ/ d = 4 at 125 kHz) d) 2 disks stacks (λ/ d = 2 at 125 kHz).

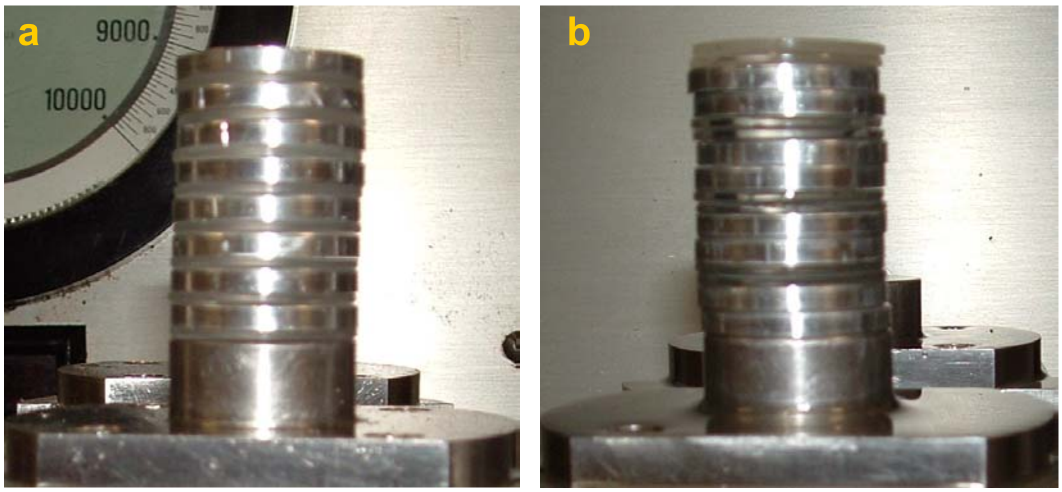

Figure 3.3b Acrylic/aluminum stacking arrangements a) Single alternating acrylic aluminum disks stack (λ/d = 16 at 125 kHz). b) Double alternating acrylic aluminum disks stack (λ/d = 8 at 125 kHz).

Sample No.	Disk Arrangement	No. of disks	Frequency kHz(λ/d)
12501	Ac/Al/Ac/Al/Ac/Al/Ac/Al/Ac/Al/Ac/Al/Ac/Al/Ac/Al	16	125 (16)
12502	Ac/Al/Ac/Al/Ac/Al/Ac/Al	8	125 (8)
12503	Ac/Al/Ac/Al	4	125 (4)
12504	Ac/Al	2	125 (2)
12505	AcAc/AlAl/AcAc/AlAl/AcAc/AlAl/AcAc/AlAl	16	125(8)
12506	AcAc/AlAl/AcAc/AlAl	8	125(4)
12507	AcAc/AlAl	4	125(2)
12508	AcAcAcAc/AlAlAlAl/AcAcAcAc/AlAlAlAl	16	125(4)
12509	AcAcAcAc/AlAlAlAl	8	125(2)
12510	AcAcAcAcAcAcAcAc/AlAlAlAlAlAlAlAl	16	125(2)
25001	Ac/Al/Ac/Al/Ac/Al/Ac/Al/Ac/Al/Ac/Al/Ac/Al/Ac/Al	16	250 (8)
25002	Ac/Al/Ac/Al/Ac/Al/Ac/Al	8	250(4)
25003	Ac/Al/Ac/Al	4	250 (2)
25004	Ac/Al	2	250 (1)
25005	AcAc/AlAl/AcAc/AlAl/AcAc/AlAl/AcAc/AlAl	16	250(4)
25006	AcAc/AlAl/AcAc/AlAl	8	250(2)
25007	AcAc/AlAl	4	250(1)
25008	AcAcAcAc/AlAlAlAl/AcAcAcAc/AlAlAlAl	16	250(2)
25009	AcAcAcAc/AlAlAlAl	8	250(1)
25010	AcAcAcAcAcAcAcAc/AlAlAlAlAlAlAlAl	16	250(1)

Table 3.3 Acrylic (Ac) and aluminum (Al) disks arrangements in the layered stack.

Table 3.3 Continued

50001	Ac/Al/Ac/Al/Ac/Al/Ac/Al/Ac/Al/Ac/Al/Ac/Al/Ac/Al	16	500 (4)
50002	Ac/Al/Ac/Al/Ac/Al/Ac/Al	8	500 (2)
50003	Ac/Al/Ac/Al	4	500 (1)
50004	Ac/Al	2	500 (0.5)
50005	AcAc/AlAl/AcAc/AlAl/AcAc/AlAl/AcAc/AlAl	16	500(2)
50006	AcAc/AlAl/AcAc/AlAl	8	500(1)
50007	AcAc/AlAl	4	500(0.5)
50008	AcAcAcAc/AlAlAlAl/AcAcAcAc/AlAlAlAl	16	500(1)
50009	AcAcAcAc/AlAlAlAl	8	500(0.5)
50010	AcAcAcAcAcAcAcAc/AlAlAlAlAlAlAlAl	16	500(0.5)
75001	Ac/Al/Ac/Al/Ac/Al/Ac/Al/Ac/Al/Ac/Al/Ac/Al/Ac/Al	16	750 (2.67)
75002	Ac/Al/Ac/Al/Ac/Al/Ac/Al	8	750 (1.33)
75003	Ac/Al/Ac/Al	4	750 (0.67)
75004	Ac/Al	2	750 (0.33)
75005	AcAc/AlAl/AcAc/AlAl/AcAc/AlAl/AcAc/AlAl	16	750(1.33)
75006	AcAc/AlAl/AcAc/AlAl	8	750(0.67)
75007	AcAc/AlAl	4	750(0.33)
75008	AcAcAcAc/AlAlAlAl/AcAcAcAc/AlAlAlAl	16	750(0.67)
75009	AcAcAcAc/AlAlAlAl	8	750(0.33)
75010	AcAcAcAcAcAcAcAc/AlAlAlAlAlAlAlAl	16	750(0.33)

3.7 Experimental Results and Discussion

Results from the experimental work on stacks of acrylic and aluminum disks that simulate a 1D layer medium (Figures 3.3a and b) are presented here. The measurements on the stacks were conducted using different combinations of disk arrangements (Figure 3.3a and b) and (Table 3.3). The tests were also done at four different frequencies (125 kHz, 250 kHz, 500 kHz and 750 kHz), and pressure values were varied (i.e. 1000 psi, 2000 psi and 3000 psi). Results from these measurements include time trace of the propagating wave and P- and S-wave velocities. Measurement at low frequency (125 kHz) with wavelength to thickness ratio (λ/d) >>1 such as in Figure 3.4d shows the wave propagating through a stack of 16 disk layers could not differentiate individual layers or the interfaces between individual layers. However, increasing special distance between the layers, for the same frequency value, which decreased the λ/d ratio, has increased the ability of the wave to pick the individual layer boundaries, but not the individual layers. In addition, this increase in frequency has generated velocity dispersion (Figures 3.5a and b). Multiple scattering of seismic waves in a heterogeneous medium causes velocity dispersion and waveform distortion (Liu and Schmitt, 2002).

Further increase in frequency and layer thickness has increased the ability of the propagating wavelet to distinguish individual layers and layer boundaries (Figures 3.5c and d). Here, individual layers and the interfaces between layers are clearly distinguished, and the layer thickness is larger than the $\delta b/2\sqrt{6}$ limit of Ricker, 1953. Figure 3.4a and b show strong dispersion and higher observed velocity than the computed velocity (i.e. early arrival time break). The λ/d in the two figures are in the specular scattering (Ray theory) and Mie scattering range, where there is a marked velocity increase (Mavko et al., 1998). Figure 3.4c shows the observed velocity is slower than the computed velocity and the λ/d is in the Rayleigh scattering. However, Figure 3.4d, which has λ/d above the Rayleigh scattering region shows the computed and observed velocities are close in value, which is a characteristic of an equivalent isotropic medium.

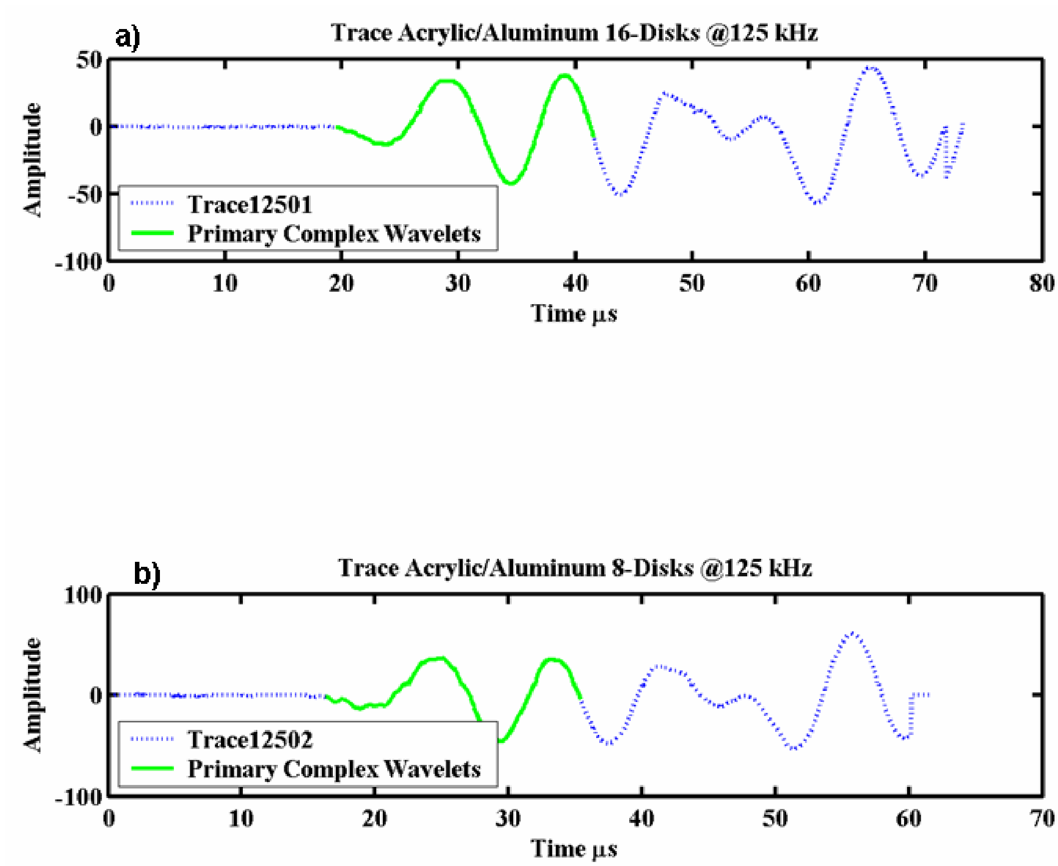

Figure 3.4a Trace for acrylic aluminum layers @ 125 kHz run: a) 16 disks with alternating layers of acrylic and aluminum ((λ/d = 16), b) 8 disks with alternating layers of acrylic and aluminum ((λ/d = 8).

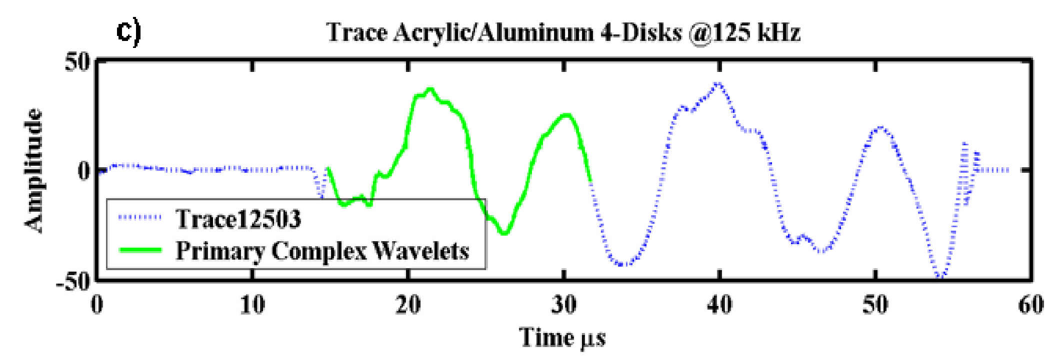

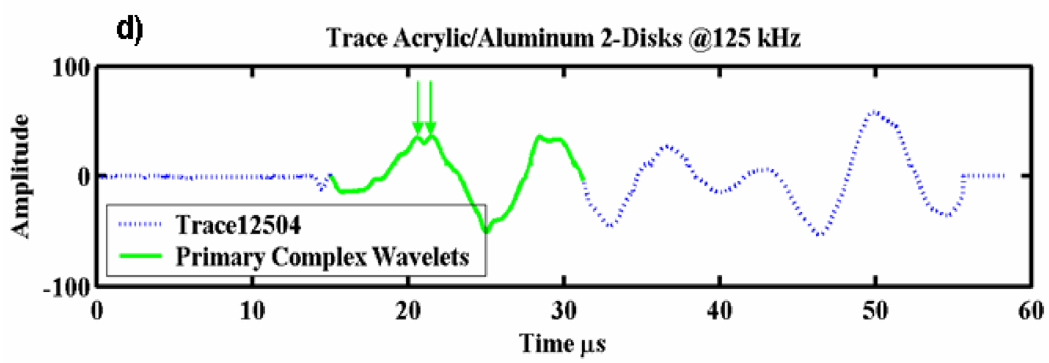

Figure 3.4 Continued …: c) 4 disks with alternating layers of acrylic and aluminum (λ/d = 4), d) 2 disks with alternating layers of acrylic and aluminum ((λ/d = 2).

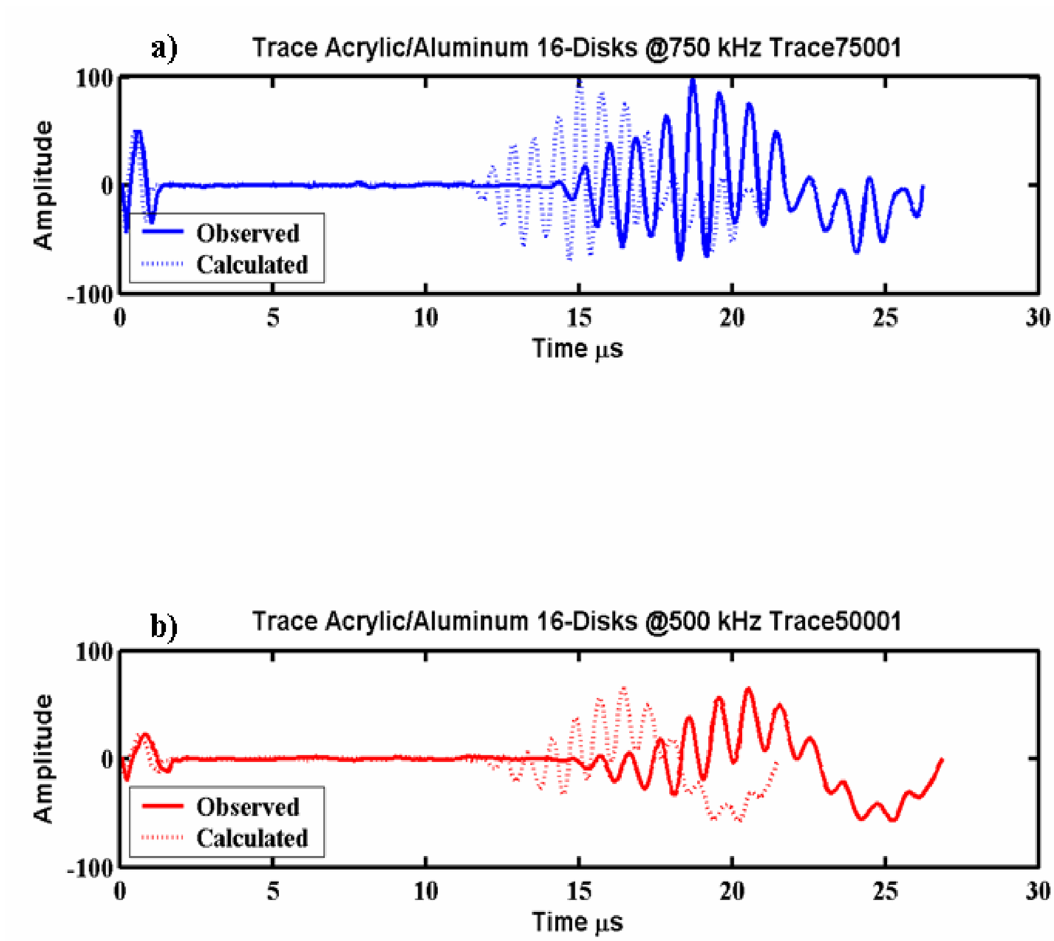

Figure 3.5 Time traces for wave propagation through two component medium at constant thicknesses: a) 16 alternating disk stacks (λ/d = 2.67), b) 16 alternating disk stacks (λ/d = 4).

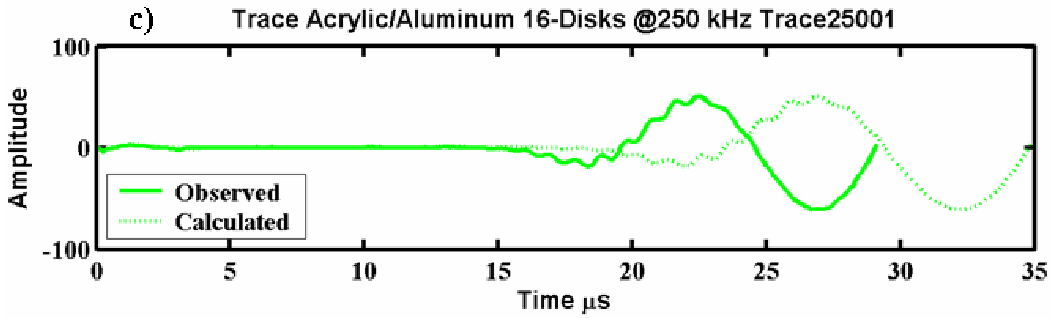

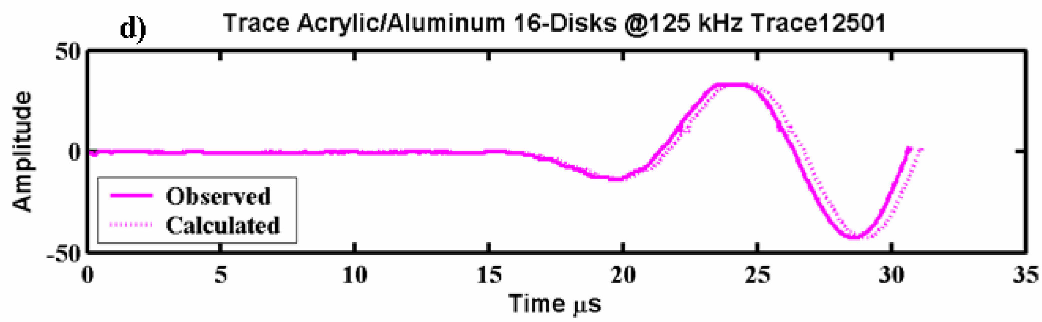

Figure 3.5 continued…: c) 16 alternating disk stacks ($\lambda/d = 8$), and d) 16 alternating disk stacks ($\lambda/d = 16$).

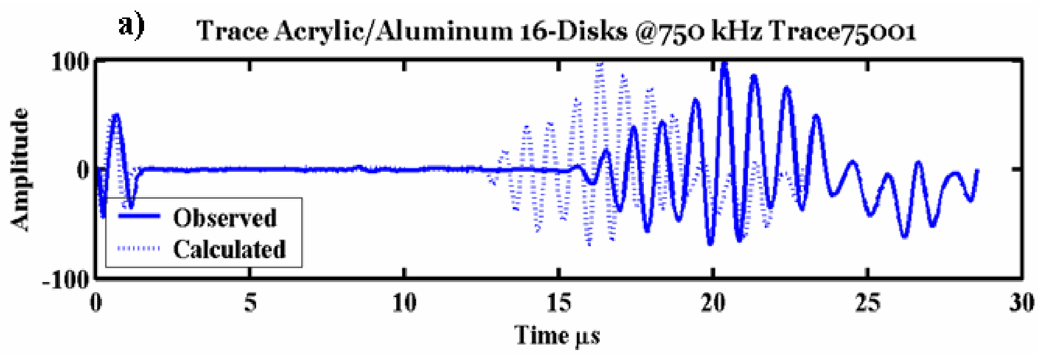

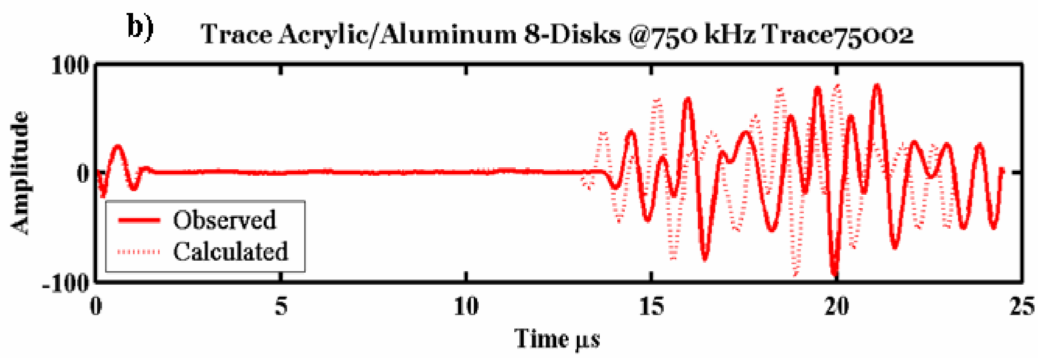

Figure 3.6 Time traces for wave propagation through two component medium at different thicknesses: a) 16 alternating disk stacks (λ/d = 2.67), b) 8 alternating disk stacks (λ/d = 1.333).

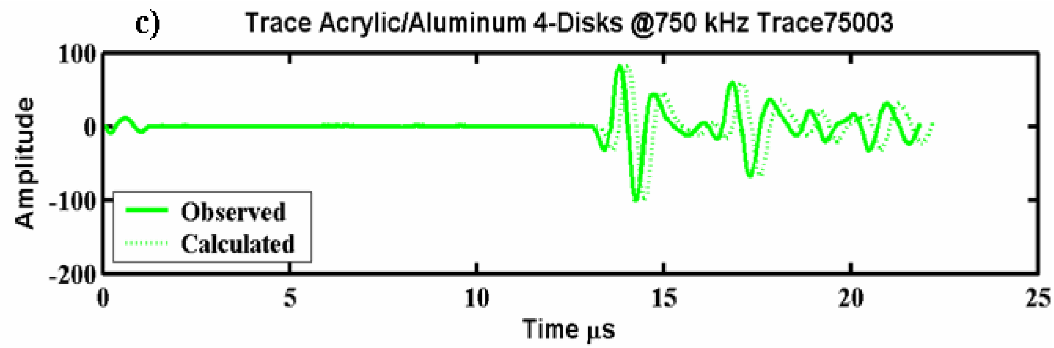

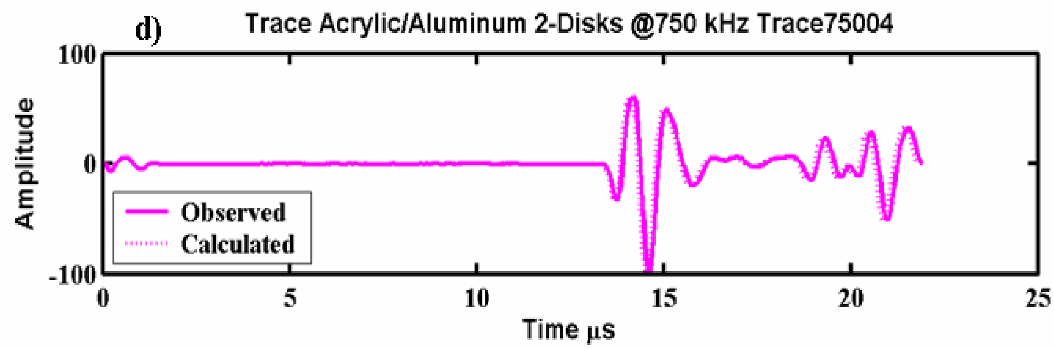

Figure 3.6 continued …: c) 4 alternating disk stacks (λ/d = 0.667), and d) 2 alternating disk stacks (λ/d = 0.333).

Observed velocity values from experimental work are tabulated in Table 3.4. In addition, Figures 3.7 through Figure 3.9 are generated based on the compressional velocity values from Table 3.5, at different confining pressure . In Figures 3.7 through 3.9 we see a general velocity decrease with increasing λ/d. There are three distinct regions on all the graphs, which are characterized by different degrees of velocity decrease with increasing λ/. The first part between 0.1 and 4 λ/d, here the velocity trend observed is gentle, but in the second part between 4 and 10 λ/d values there is a steep decline in velocity, and in the third part, for λ/d greater than 10 the velocity decrease trend completely changes showing a slight increase. The first part of the graphs corresponds to the dispersion region of specular scattering (Ray Theory) up to Mie scattering (Mavko et al., 1998). Then, the second portion of the graph relates to the region between the Mie scattering and Rayleigh scattering, and the λ/d ≈ 10 to the Rayleigh scattering region (Mavko et al., 1998) .

Based on the observation made, there are three regions of velocity dispersion. The first is where λ/d < 4, with very low dispersion and the medium can be expressed using Ray theory. Here, dispersion is small and the medium is constituted by individual homogeneous entities. Second the region between the Mie and Rayleigh scattering, where there is significant velocity dispersion. Finally, the region beyond the Rayleigh scattering can be represented by an effective medium (Backes, 1962; Marion and Coudin, 1992; Mukerji at al., 1995; Mavko et al., 1998; and Liu and Schmitt, 2002).

P-wave and S-wave Velocities for Single Alternating Acrylic and Aluminum Disk Stacks, 16 Disks							
λ/d	Frequency	Pp1_vel	Pp2_vel	Pp3_vel	Sp1_vel	Sp2_vel	Sp3_vel
16	125 kHz	3448	3583	3514	3141	3252	3195
8	250 kHz	3569	3744	3870	2005	2050	2097
4	500 kHz	3728	3759	3790	2121	2097	2050
2.67	750 kHz	3838	3846	3879	2225	2309	2225

P-wave and S-wave Velocities for Single Alternating Acrylic and Aluminum Disk Stacks, 8 Disks							
λ/d	Frequency	Pp1_vel	Pp2_vel	Pp3_vel	Sp1_vel	Sp2_vel	Sp3_vel
8	125 kHz	3524	3593	3524	1988	2010	2055
4	250 kHz	4262	4282	4302	2257	2257	2303
2	500 kHz	4333	4333	4353	2368	2425	2444
1.333	750 kHz	4322	4353	4374	2464	2504	2525

P-wave and S-wave Velocities for Single Alternating Acrylic and Aluminum Disk Stacks, 4 Disks							
λ/d	Frequency	Pp1_vel	Pp2_vel	Pp3_vel	Sp1_vel	Sp2_vel	Sp3_vel
4	125 kHz	3728	3806	3806	2198	2172	2172
2	250 kHz	4498	4565	4565	2532	2532	2568
1	500 kHz	4515	4543	4554	2634	2657	2657
0.667	750 kHz	4515	4543	4571	2721	2721	2721

P-wave and S-wave Velocities for Single Alternating Acrylic and Aluminum Disk Stacks, 2 Disks							
λ/d	Frequency	Pp1_vel	Pp2_vel	Pp3_vel	Sp1_vel	Sp2_vel	Sp3_vel
2	125 kHz	3740	3665	3740	2688	2688	2770
1	250 kHz	4406	4406	4448	3252	3206	3252
0.5	500 kHz	4427	4427	4465	2728	2728	2778
0.333	750 kHz	4411	4427	4448	2451	2451	2812

P-wave and S-wave Velocities for Double Alternating Acrylic and Aluminum Disk Stacks, 16 Disks							
λ/d	Frequency	Pp1_vel	Pp2_vel	Pp3_vel	Sp1_vel	Sp2_vel	Sp3_vel
8	125 kHz	3583	3806	4151	1941	1941	1941
4	250 kHz	4151	4151	4228	1992	1992	1992
2	500 kHz	4267	4328	4369	2005	2027	2073
1.333	750 kHz	4308	4297	4287	2027	2027	2073

Table 3.4 P-wave and S-wave velocities for acrylic and aluminum disks 1D layer case

Table 3.4 Continued

P-wave and S-wave Velocities for Double Alternating Acrylic and Aluminum Disk Stacks, 8 Disks							
λ/d	Frequency	Pp1_vel	Pp2_vel	Pp3_vel	Sp1_vel	Sp2_vel	Sp3_vel
4	125 kHz	3524	3593	3593	2471	2471	2471
2	250 kHz	4262	4302	4343	2680	2712	2745
1	500 kHz	4312	4312	4374	2728	2804	2778
0.667	750 kHz	4302	4343	4343	2778	2812	2812
P-wave and S-wave Velocities for Double Alternating Acrylic and Aluminum Disk Stacks, 4 Disks							
λ/d	Frequency	Pp1_vel	Pp2_vel	Pp3_vel	Sp1_vel	Sp2_vel	Sp3_vel
2	125 kHz	4059	4151	4248	2252	2252	2280
1	250 kHz	4248	4248	4267	2438	2438	2412
0.5	500 kHz	4267	4308	4433	2315	2338	2338
0.33	750 kHz	4292	4313	4338	2498	2532	2532
P-wave and S-wave Velocities for Quadruple Alternating Acrylic and Aluminum Disk Stacks, 16 Disks							
λ/d	Frequency	Pp1_vel	Pp2_vel	Pp3_vel	Sp1_vel	Sp2_vel	Sp3_vel
4	125 kHz	3524	3665	3665	2649	2612	2612
2	250 kHz	4364	4395	4416	2680	2712	2712
1	500 kHz	4395	4427	4448	2830	2804	2830
0.667	750 kHz	4416	4416	4459	3555	3611	3501
P-wave and S-wave Velocities for Quadruple Alternating Acrylic and Aluminum Disk Stacks, 8 Disks							
λ/d	Frequency	Pp1_vel	Pp2_vel	Pp3_vel	Sp1_vel	Sp2_vel	Sp3_vel
2	125 kHz	4151	4151	4248	2252	2280	2280
1	250 kHz	4248	4267	4348	2387	2412	2438
0.5	500 kHz	4267	4308	4338	2464	2532	2498
0.333	750 kHz	4318	4338	4390	2532	2568	2604
P-wave and S-wave Velocities for Octuple Alternating Acrylic and Aluminum Disk Stacks, 4 Disks							
λ/d	Frequency	Pp1_vel	Pp2_vel	Pp3_vel	Sp1_vel	Sp2_vel	Sp3_vel
2	125 kHz	4072	4165	4072	2374	2344	2314
1	250 kHz	4312	4333	4343	2612	2634	2612
0.5	500 kHz	4282	4312	4364	2728	2704	2753
0.333	750 kHz	4322	4333	4353	2778	2795	2812

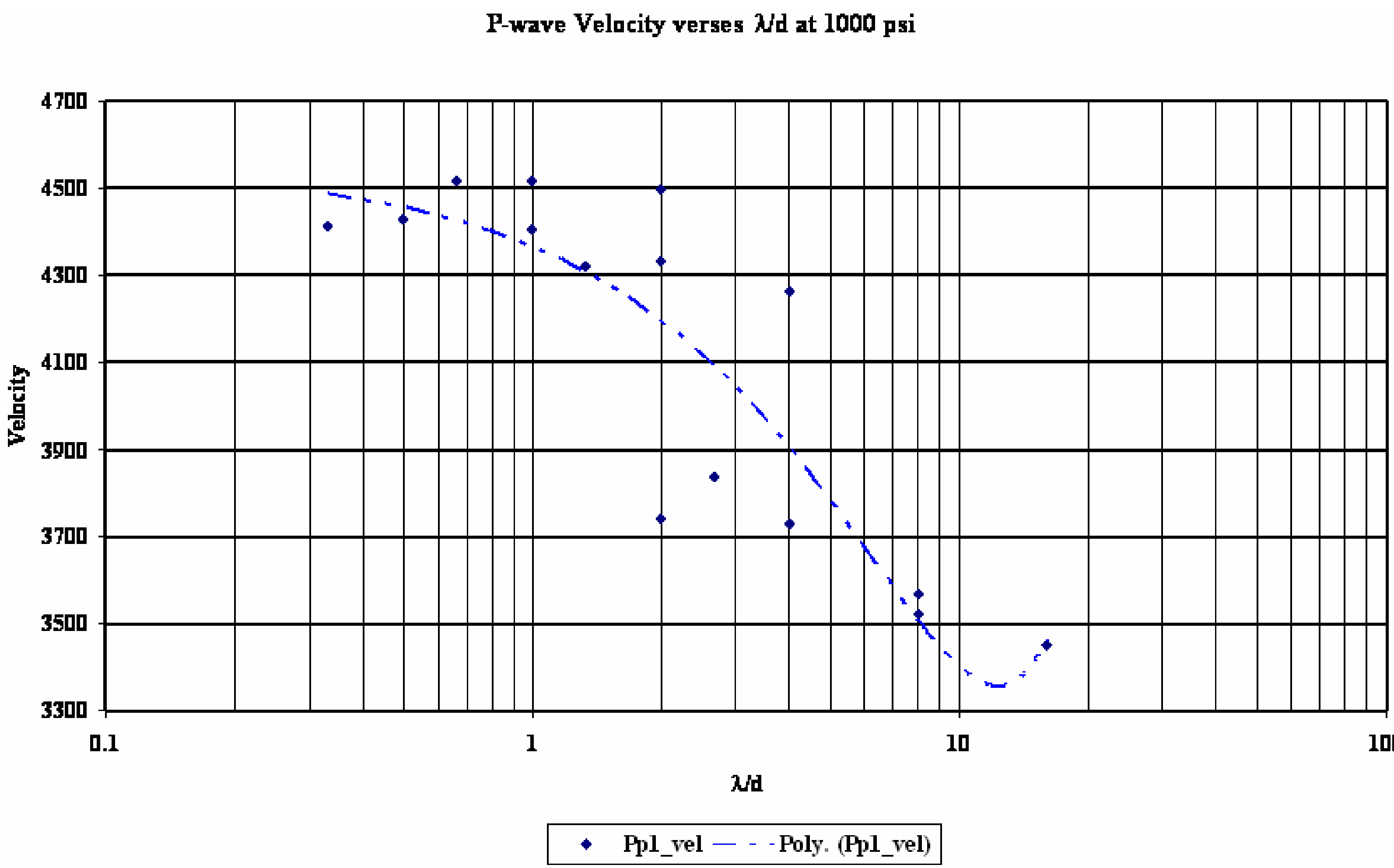

Figure 3.7 P- wave velocity verses λ/d for layered acrylic and aluminum disks at confining pressure = 1000 psi.

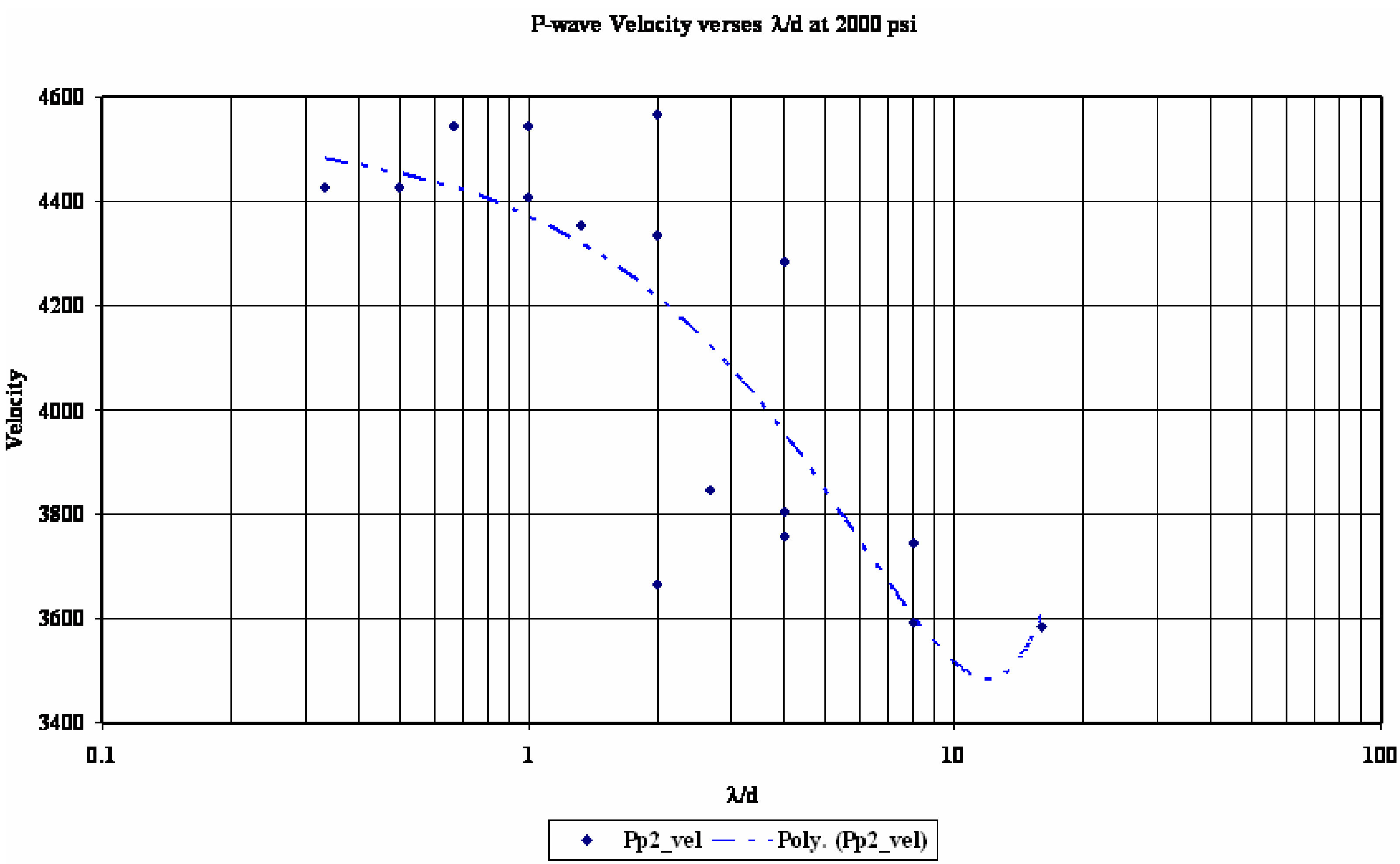

Figure 3.8 P- wave velocity verses λ/d for layered acrylic and aluminum disks at confining pressure = 2000 psi.

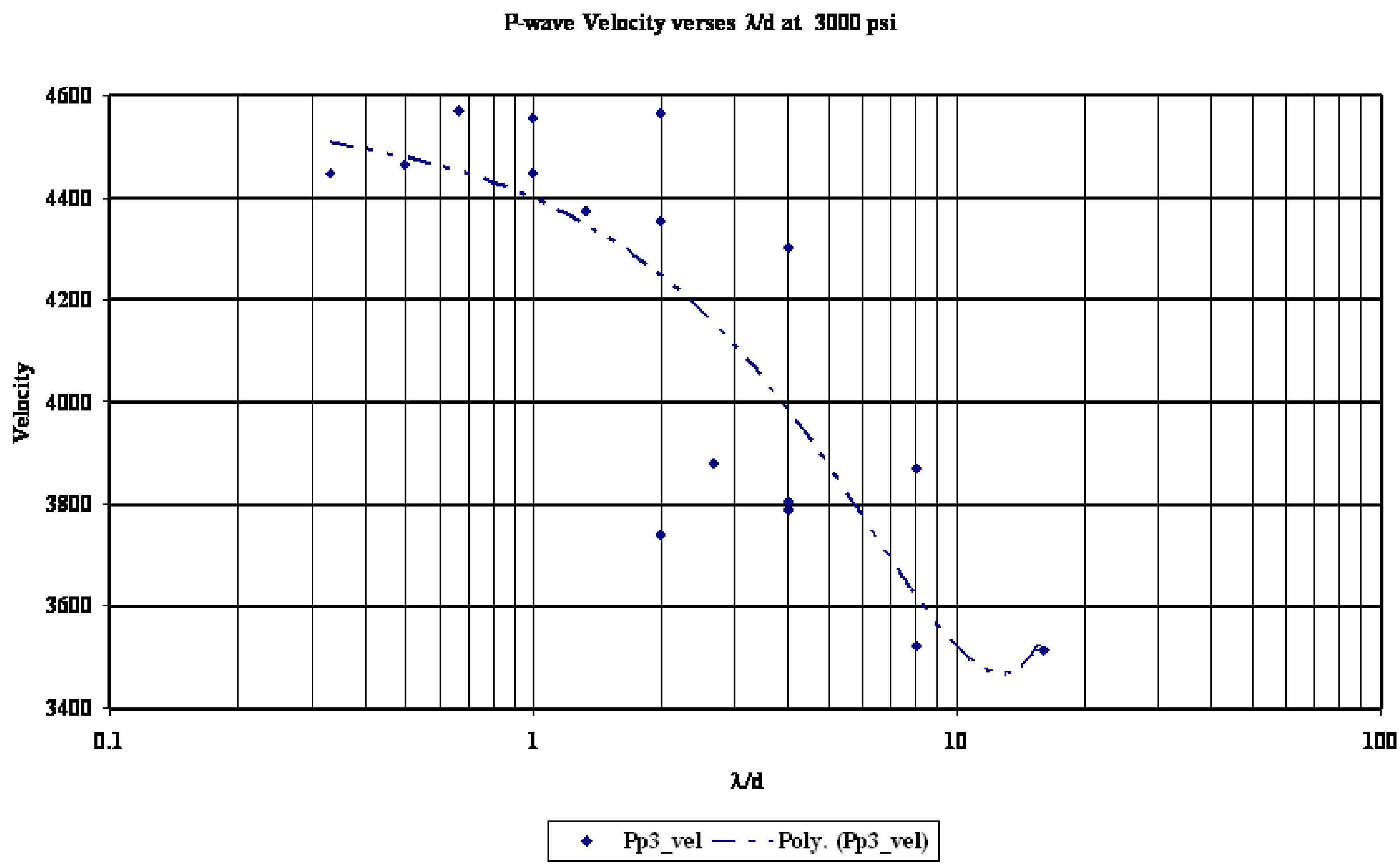

Figure 3.9 P- wave velocity verses λ/d for layered acrylic and aluminum disks at confining pressure = 3000 psi.

3.8 Summary and Conclusions

From the computational and experimental observation made, scale of heterogeneity and wavelength of the wavelet propagating through the medium play important role in shaping the way the velocity of the medium computed. For the long wavelength limit, by applying the equivalent medium theory of Backus (1962), it is possible to replace fine layered units by an equivalent thicker homogeneous transversely isotopic layer. However, for the short wavelength case, each layer behaves as a piecewise homogeneous medium. Therefore, the velocity in this case can be computed for the individual entity. In each extreme case velocity dispersion is very small, and there is less velocity deviation. However, for the case in between the extreme cases velocity dispersion is very high, and the velocity dispersion can be computed Floquets solution (Mavko et al., 1998). It is evident that with increasing dispersion amplitude of the propagating wave also affected. Depending on the phase and spacial separation of the medium, the interfering wave complexes interact constructively or destructively. When the spatial period $d_1 + d_2$ is an integer multiple of one-half the wavelength, multiple reflections are in phase and add constructively, resulting in a large total accumulated reflection (Figure 3.4a).

Now, one needs to apply these important aspects of bed thickness to wavelength relationship to the actual rocks in the subsurface.

Chapter 4

LABORATORY MEASUREMENT OF INTRINSIC ATTENUATION AND QUALITY FACTOR ON CORE SAMPLES

4.1 Introduction

Seismic waves propagating through the earth are attenuated by a number of processes, and these processes include conversion of some fraction of the elastic energy to heat energy due to friction. Proper understanding of the attenuative property of the earth has two important implications in seismic exploration and reservoir geophysics. First, seismic wave amplitudes dissipate as waves propagate through an anelastic medium, and this reduction in amplitude is generally frequency dependent. Second, the intrinsic attenuation (α), the exponential decay constant of the amplitude of a plane wave traveling in a homogeneous medium, and quality factor (Q), the internal friction or dissipation factor, reveal much information, such as lithology, physical state, fluid content, and degree of saturation (Toksoz and Johnston, 1981).

Laboratory measurements, using the wave propagation method, of compressional velocity (V_p), shear velocity (V_s), attenuation coefficient, and quality factor were conducted on a reference sample and core samples collected from Well C-276 in La Concepcion field, Venezuela. Wave propagation experiments are classified into two principal techniques based on their use of pulse-echo or pulse-through transmission techniques. For this research the pulse-through transmission technique is used to measure velocities (V_p and V_s), intrinsic attenuation, and quality factor. A spectral ratio, which is by far the most commonly used technique in seismology (Ward and Toksoz, 1971), is used to calculate the intrinsic attenuation and quality factor. Cylindrical samples (25.4 mm in diameter) of aluminum (reference sample) and core samples of different length were prepared for measurement. The experiment was carried out in a pressure vessel on jacketed samples, and it was performed at 750 kHz. The confining pressure was varied (5372 psi, 5448 psi, and 5753 psi) to simulate borehole condition. However, the pore pressure was kept constant. On-screen velocity picking was conducted for compressional velocity (V_p), and shear velocities (V_{s1} and V_{s2}) from the first break of the trace display. Finally, the velocities (V_p and V_s) were plotted against Q_p and Q_s values.

The results from these plots indicate there are significant correlations between V_p, V_s, Q_p and Q_s. In addition, the Q_p/Q_s plot show a better correlation to porosity and permeability than the V_p/V_s plot. A better understanding of the absorptive property of the earth should enhance the efficiency of seismic exploration work.

4.2 Objectives

The importance of this investigation is to experimentally measure velocity, intrinsic attenuation coefficients and quality factor of core samples collected from a well in La Concepcion Field, Venezuela. The results from these measurements will be used to constrain the velocity, intrinsic attenuation coefficients and quality factors computed from well log and 3D seismic data of the same field.

4.3 Sample Preparation

Cylindrical core samples representing a source and seal unit (La Luna Formation), and reservoir unit (Cogollo Group) were collected between 10450 and 11541 ft depth of Well C-276. A total of 62 samples were gathered, of which 46 samples were ready for analysis. Most of the samples are cored vertically the bedding plane; however, there are a few samples which are cored horizontally the bedding plane. The samples vary in length from 21.22 mm to 42.40 mm, and the average length is 34.21 mm. The path of the pulse wave from the source to the receiver and the rock sample length (d) should be greater than one wavelength of the pulse ($d/\lambda > 1$). In this experiment, the average wavelength of the pulse is 6.1 to 8.53 mm. The sample diameter ranges between 25.77 mm to 25.33 mm with the mean value for the sample diameter being 25.18 mm. To avoid cancellation of the direct first arrival amplitude by interference from waves reflected off the sample sidewalls, the sample length should be less than five times the sample diameter. Accurate velocity estimation can only be achieved in samples with length to diameter ratio (d/a) less than five. In addition, this range of sample diameters helps to prevent a waveguide effect, a geometric diffraction, because the sample radius average of 12.59 mm exceeds the wave length of the ultrasonic pulse wavelength that is transmitted along the sample. When sample radius (r) < λ, the waveguide effect attenuates and slows the propagating wave, which causes the wave to travel at a reduced velocity- bar velocity- as r becomes smaller and smaller with respect to λ (Schreiber et al., 1973). The samples generally have grains and pores smaller than 0.8 mm; this helps to avoid multiple scattering of the ultrasonic wave by pores and grains in the rock sample. Furthermore, the wavelength of the transmitted pulse should be at least three times larger than the largest grain and/or pore size ($\lambda_s/d_s > 3$) in the sample (Plona and Tsang, 1979). To obtain a good coupling with the transducer during measurement, the two ends of the core samples are polished smooth. A very fine grade (400) sand paper is used to polish the samples.

4.4 Sample Description

The samples collected came from four formations, the La Luna, the Marca, the Lisure, and the Apon Formations. The last three formations make up the Cogollo group, a reservoir unit in the region. The La Luna Formation is generally a mixed carbonate with inter-layered shale (Figure 4.1). The La Luna Formation is both the source and sealing rock in the field. The Cogollo Group is a mixed carbonate with interbeds of siliciclastic layers at the base, and becomes a clean carbonate at the top. The lower three formations that belong to the Cogollo Group (Marca, Lisure, and Apon) make the reservoir unit in the La Concepcion Field. The formations are mainly limestone, with some diagenetic dolomite and minor quartz wackestone interbeds (Figure 4.2). In general, porosity is poor to moderate, and permeability is very low (Table 4.3) in the samples collected. Diagenesis is prevalent, especially cementation. Dolomitization is not uncommon, and it ranges from partial dolomitization (dolomite rhombs floating in sparite ground mass) to complete dolomitization (Figure 4.3).

Figure 4.1. Core sample from Well C-276, La Concepcion Field, La Luna Formation. Sample shows thinly laminated shale with fracture; fracture is filled calcite (depth 10431’1”).

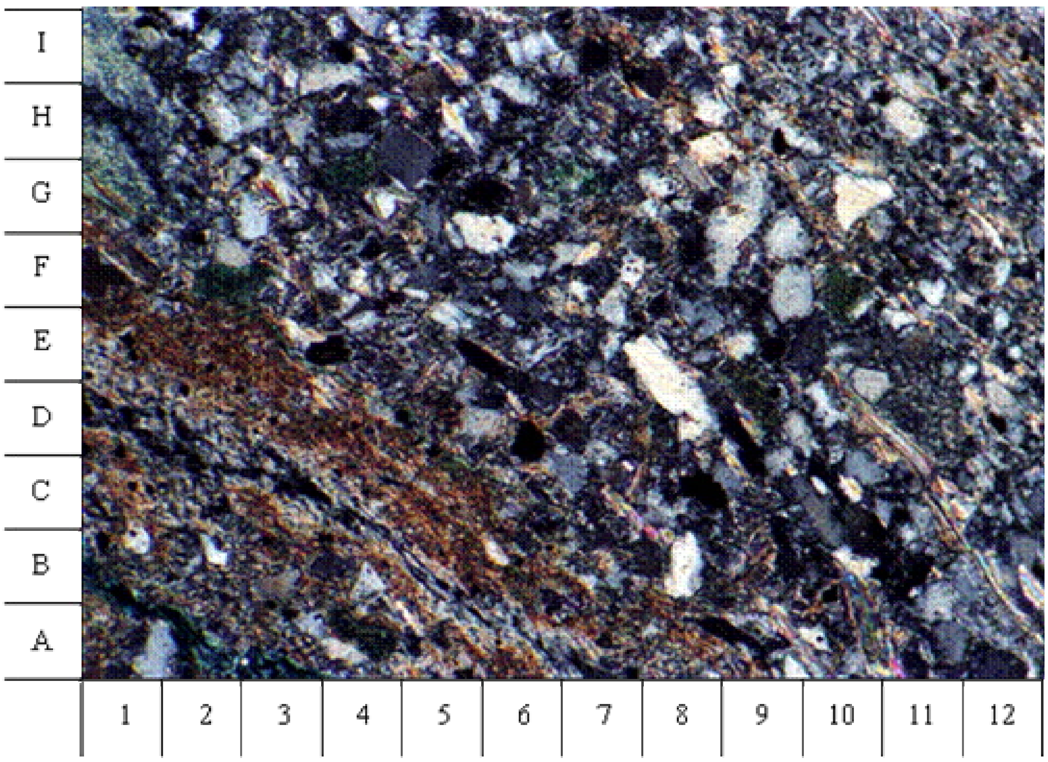

Figure 4.2. Thin section from the La Luna Formation, with layering indicated by preferred orientation of elongate grains of micas and quartz.

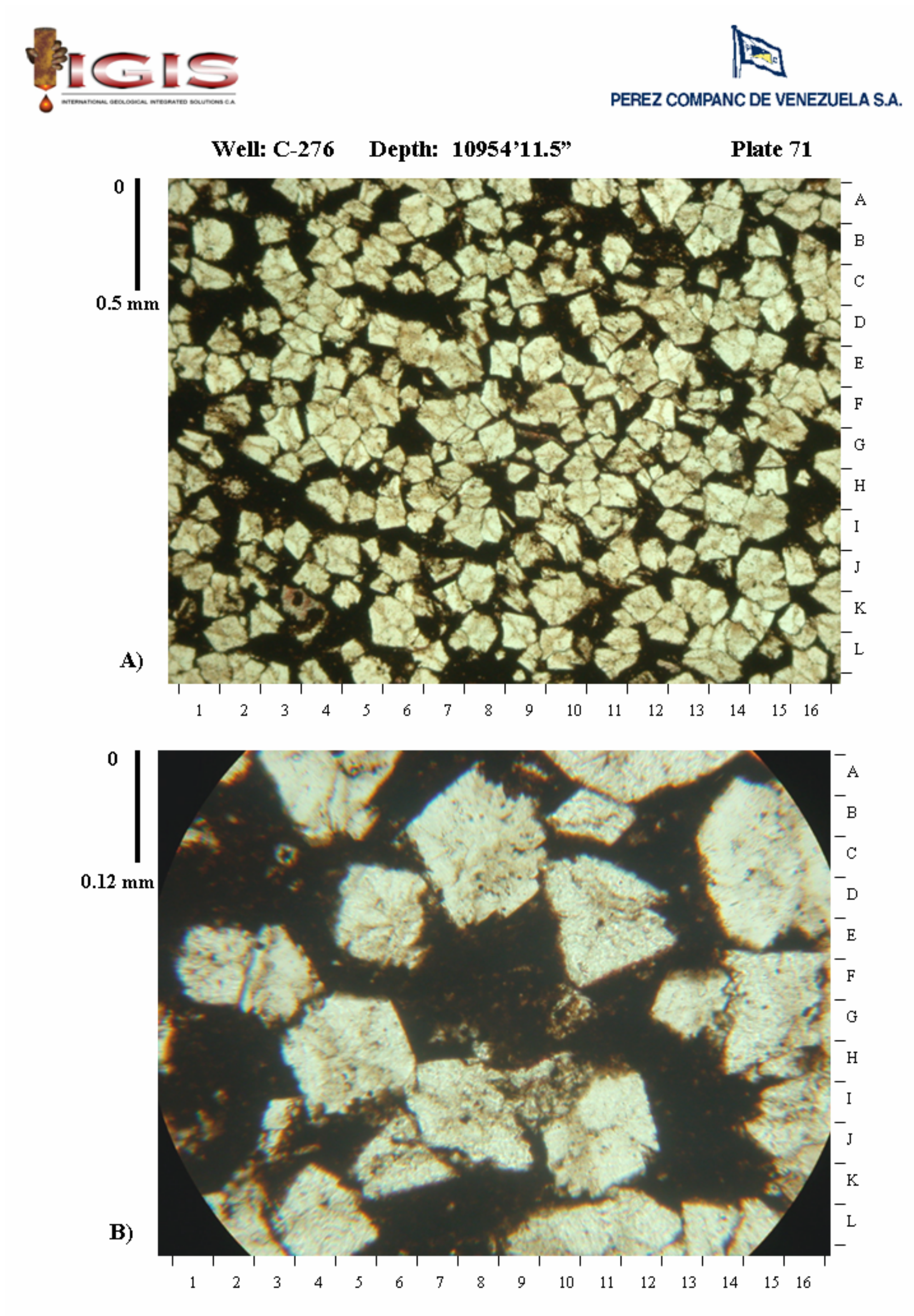

Figure 4.3. Thin section of dolomite from the Cogollo Group with inter-crystaline porosity and dead oil filling porosity (depth 10954’11.5”).

4.5 Velocity and Attenuation Measuring Apparatus

Measurement of P-wave and S-wave velocities was carried out in a pressure vessel (figure 4.4), and the samples were jacketed in an impermeable rubber-sheath (Figures 4.4 and 4.5). The measuring pressure vessel consists of a cylindrical vessel that encases the transducers, the samples, the electrical wiring, and a fluid connected to pressure pumps and pressure gauge via small tubes. There are two recording cells, a top and a bottom one, each with a top and a bottom transducer (Figure 4.4). In addition, each cell holds the sample to be measured; the sample covered with an impermeable rubber-sheath is held in between the two transducers. The transducers have piezoelectric crystals that generate and record ultrasonic pulse (Figure 4.5).

Pulse Transmission Technique Measurement Assembly

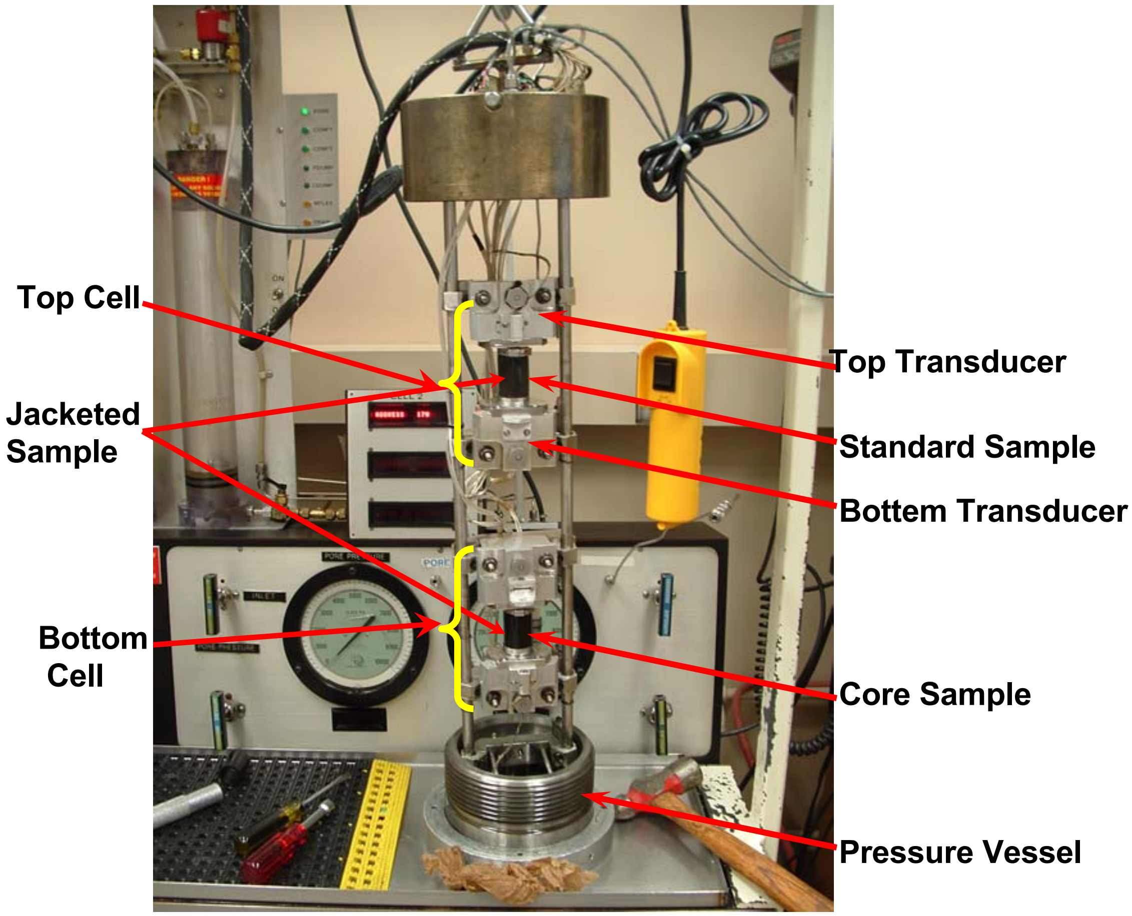

Figure 4.4. Through-pulse transmission measuring pressure vessel assembly.

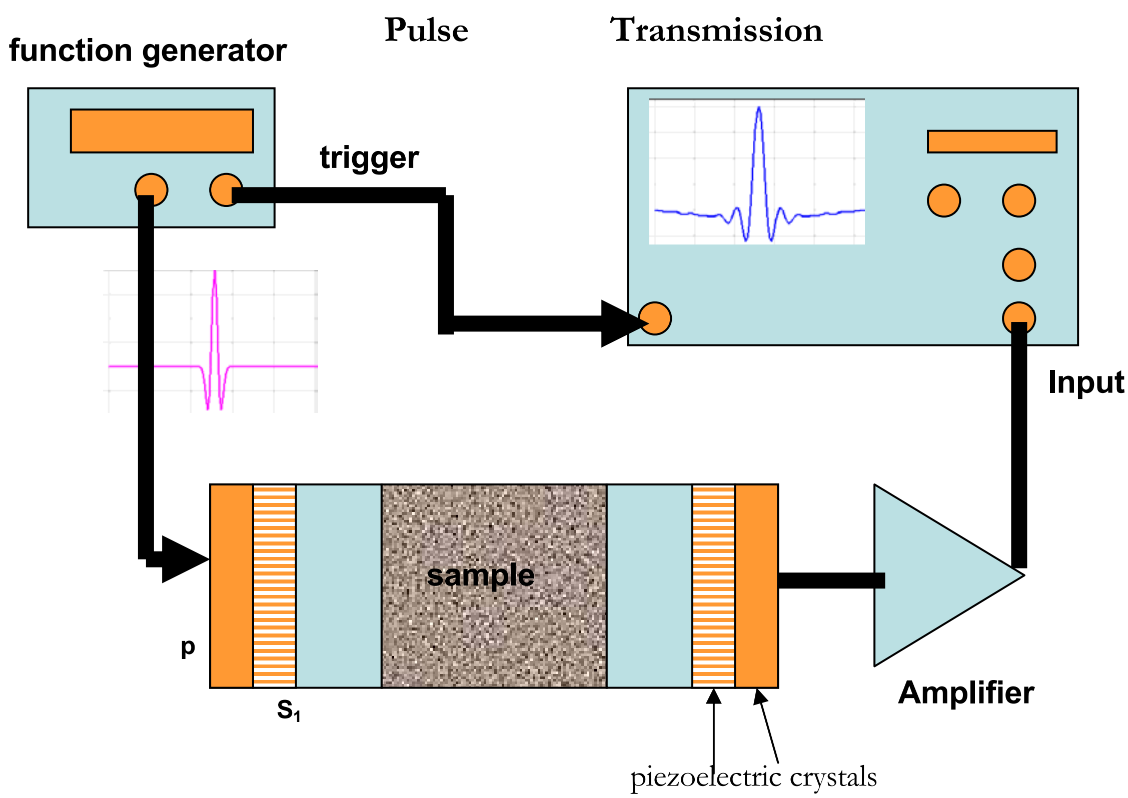

Figure 4.5. Schematic diagram of pulse transmission technique. By connecting the wires, we can select the proper combination of P and S transducers (after Dr. Sondergeld).

4.6 Velocity Measurement

In ultrasonic through-pulse transmission, velocities (V_p, V_{s1} and V_{s2}) are measured indirectly from the recorded travel-time of the transient pulse (ultrasonic pulse). In this experiment the software used to record the transient pulse travel time accounts for the time delay through the endcaps (Figure 4.6). However, the velocity computed from the trace curve (Figure 4.7) is calculated using Equation 4.1.

Equation 4.1 Velocity calculated from direct arrival time.

$$V_{ij} = \frac{D}{t_T - t_{ec}}$$

where V_{ij} is either P-velocity or S-velocities; D is length of the sample; t_T is one-way total travel time (i.e. travel time through the top and bottom endcaps and the sample), and t_{ec} is travel time through the two endcaps.

In this velocity computation the measured travel time is a one-way travel time. Moreover, during velocity measurement, one end of the transducer served as a source while the other end served as a receiver (Figure 4.6), and vice versa. In addition, a time trace is generated from this measurement (Figure 4.7). This time trace shows multiple reflections generated by wave bouncing back and forth in between the top and the bottom interfaces (Figure 4.6). Therefore, the complete time trace section contains the first break, the primary reflector, and multiple reflectors (Figure 4.7). Throughout the velocity measurement processes the confining pressure is varied to simulate subsurface condition, but the pore pressure is kept constant by venting it out to the atmosphere. The calculation for confining pressure is performed assuming a normal pressure gradient, and a value of 0.50 psi/ft. Three depth points, at the top, in the middle, and at the bottom of the section were selected for the confining pressure computation. However, all the samples were measured using the three confining pressure values (i.e. top pressure = 5231 psi at 10462 ft, middle pressure = 5448 psi at 10896.3, and bottom pressure = 5753 psi at 11506.8). The outputs for each sample from the velocity measurements include, P-wave velocity, S1-wave velocity, and S2-wave velocity at each confining pressure points (Table 4.1). In addition, elastic parameters such as bulk modulus (K) and shear modulus (μ) are calculated from the P-wave, S-wave and density information (Table 4.2). Measured P-wave and S-wave velocities and density verses depth are given in Table 4.1, and plotted in Figure 4.8. Furthermore, V_p and V_s at each pressure point are calculated and presented in Table 4.1.

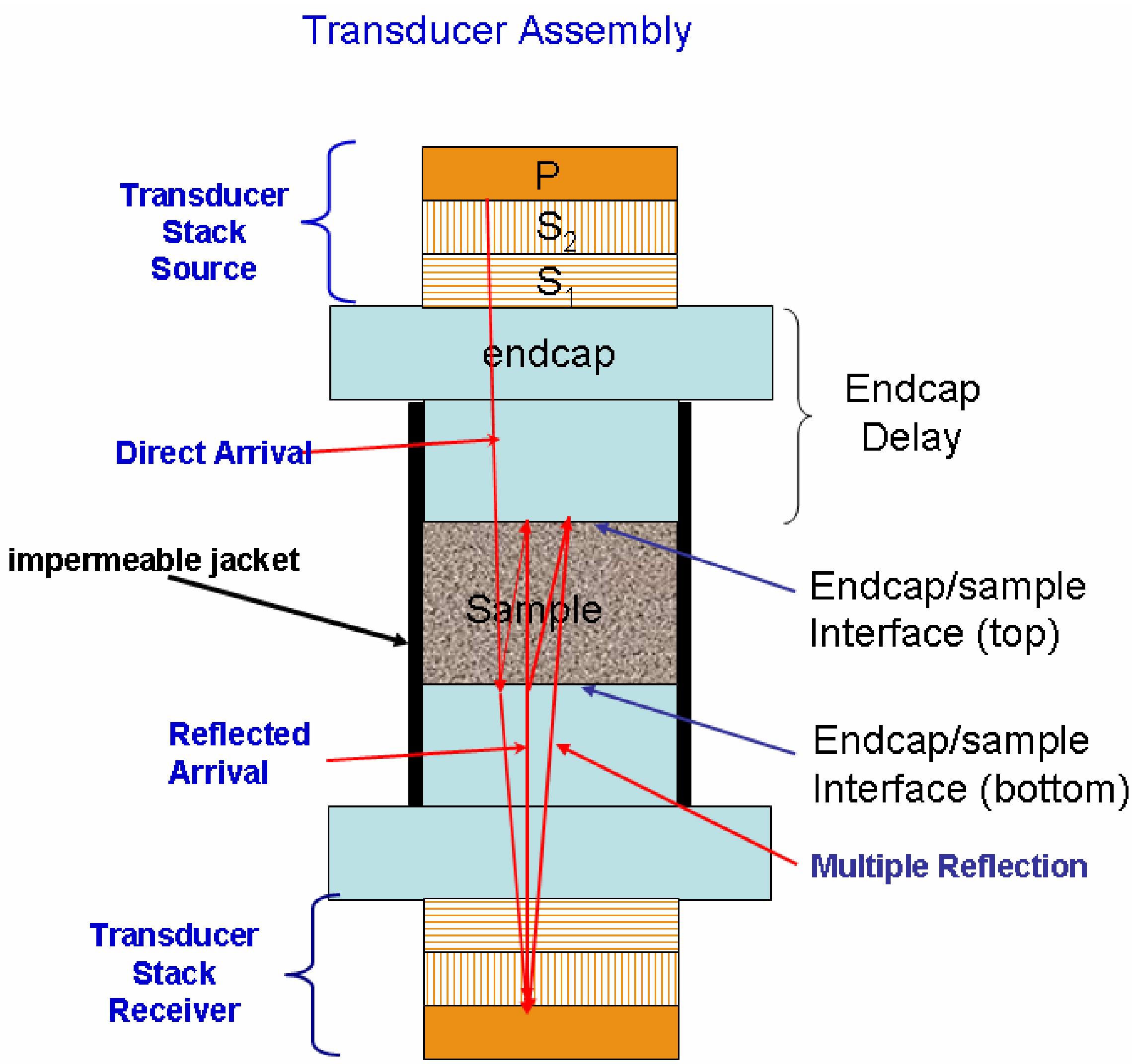

Figure 4.6 Schematic diagram of transducer assembly with jacketed sample, shows interface boundaries (blue arrows), ray path (red arrows), and source and receiver transducer (modified after Dr. Sondergeld).

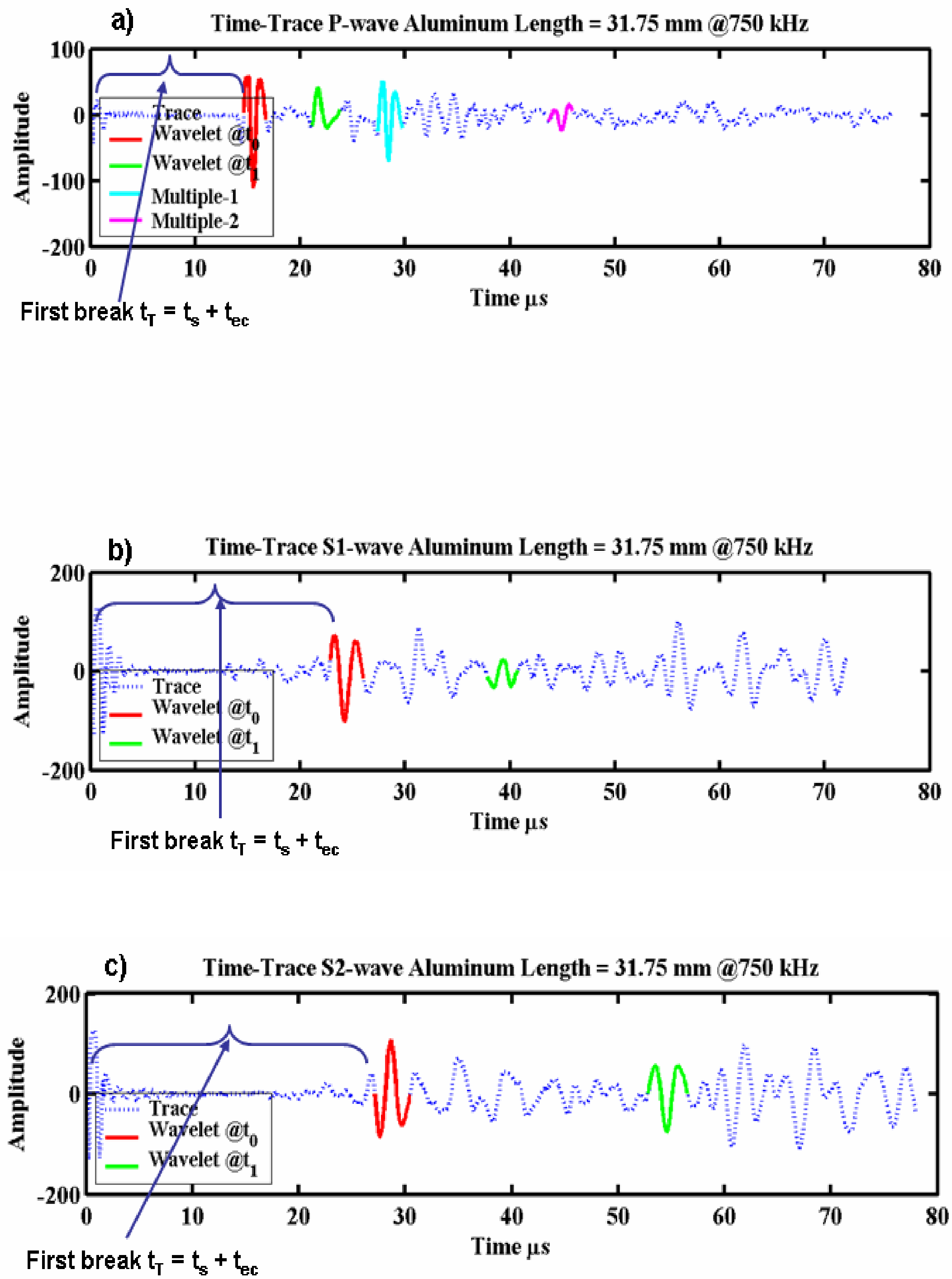

Figure 4.7 Time-trace plot, a) P-wave, b) S1-wave, and c) S2-wave, showing First break, reflections, and multiple reflections due to reverberation.

Depth(ft)	Vp P=5231 psi	Vp P=5448 psi	Vp P=5753 psi	Vs1 P=5231 psi	Vs1 P=5448 psi	Vs1 P=5753 psi	Vs2 P=5231 psi	Vs2 P=5448 psi	Vs2 P=5753 psi	ρ(gm/cc)
10455.3	5719	5735	5742	2810	2815	2815	3430	3437	3437	2.41
10464.1	5959	5981	6015	3239	3258	3278	3235	3248	3268	2.66
10465.9	6047	6060	6098	2843	2860	2883	3493	3502	3528	2.633
10468.7	5393	5460	5471	3007	3077	3077	3029	3082	3100	2.595
10470.1	5044	5065	5101	2708	2716	2741	3102	3118	3129	2.233
10488.2	6369	6378	6416	2941	2956	2976	3584	3577	3629	2.666
10510.5	5952	5996	6041	3220	3233	3233	3185	3198	3224	2.674
10523.5	5576	5591	5620	3000	3017	3034	3120	3138	3166	2.582
10543.6	5571	5603	5683	3073	3083	3093	2904	2916	2929	2.66
10765.7	5931	5950	5977	2653	2657	2662	3097	3102	3113	2.68
10816.9	3185	3199	3228	1773	1779	1787	1783	1783	1798	2.633
10832	4329	4356	4384	2386	2386	2406	2615	2615	2664	2.686
10899.9	5661	5697	5762	2764	2768	2781	3388	3401	3420	2.632
10922.1	6104	6125	6190	3274	3281	3293	3212	3212	3247	2.661
10954.9	4775	4810	4870	2573	2586	2590	2856	2864	2890	2.705
10955.5	6105	6125	6174	3371	3386	3402	3350	3368	3380	2.724
10998.3	6266	6285	6294	2937	2937	2949	3559	3559	3577	2.684
11027.3	5578	5617	5632	3141	3151	3166	3163	3188	3208	2.847
11133.8	6138	6138	6201	2866	2882	2893	3426	3441	3465	2.662
11135.9	6307	6338	6369	3697	3740	3783	3296	3322	3365	2.684
11163.9	6447	6472	6520	2933	2958	2971	3716	3746	3756	2.667
11198.7	5748	5763	5826	3188	3206	3226	3034	3047	3060	2.687

Table 4.1 Core samples P-wave and S-wave velocities, and density verses samples depth (dry samples are measured, velocity in m/sec, and P = confining pressure).

Depth(ft)	Vp P=5231 psi	Vp P=5448 psi	Vp P=5753 psi	Vs1 P=5231 psi	Vs1 P=5448 psi	Vs1 P=5753 psi	Vs2 P=5231 psi	Vs2 P=5448 psi	Vs2 P=5753 psi	ρ(gm/cc)
11214.8	5159	5188	5238	2756	2768	2776	3187	3203	3220	2.635
11220.5	4666	4695	4737	2842	2855	2868	2827	2840	2858	2.649
11242.5	5451	5482	5543	2811	2823	2860	3303	3308	3331	2.69
11259.5	6043	6077	6148	3240	3248	3262	3211	3221	3250	2.648
11283.2	6013	6024	6076	2604	2608	2620	2983	2999	3014	2.643
11290.8	5070	5101	5140	2804	2822	2842	2806	2825	2854	2.48
11293.5	5068	5097	5141	2488	2495	2513	2982	3012	3048	2.415
11300.9	5235	5286	5337	2876	2891	2917	2909	2919	2951	2.51
11301.5	5531	5569	5623	2740	2747	2758	3290	3306	3322	2.618
11307.9	5669	5714	5752	3139	3148	3159	3141	3150	3164	2.663
11322	5633	5702	5772	2669	2675	2701	3399	3419	3483	2.598
11330.2	5656	5682	5745	3096	3107	3120	3109	3123	3136	2.621
11345.6	6130	6197	6287	2900	2915	2937	3617	3655	3689	2.687
11347.7	5775	5799	5869	3463	3479	3513	3442	3463	3489	2.693
11363	5214	5254	5306	2710	2724	2739	3602	3625	3652	2.626
11390.6	5080	5115	5158	2950	2960	2983	2920	2934	2957	2.68
11408	5130	5160	5213	2588	2595	2607	2998	3003	3023	2.724
11442.1	5516	5542	5577	2684	2704	2717	2702	2719	2753	2.664
11450.9	4631	4691	4753	2235	2235	2249	2833	2848	2871	2.644
11484.2	6238	6280	6394	2877	2889	2913	3530	3557	3575	2.663
11504.5	6293	6331	6449	3350	3364	3394	3339	3346	3368	2.682
11520	5459	5485	5520	2734	2738	2756	3235	3247	3259	2.65
11529.4	6198	6231	6242	3328	3340	3359	3318	3331	3356	2.686
11541.1	6085	6117	6148	3197	3203	3220	3177	3194	3217	2.672

Table 4.1 Continued

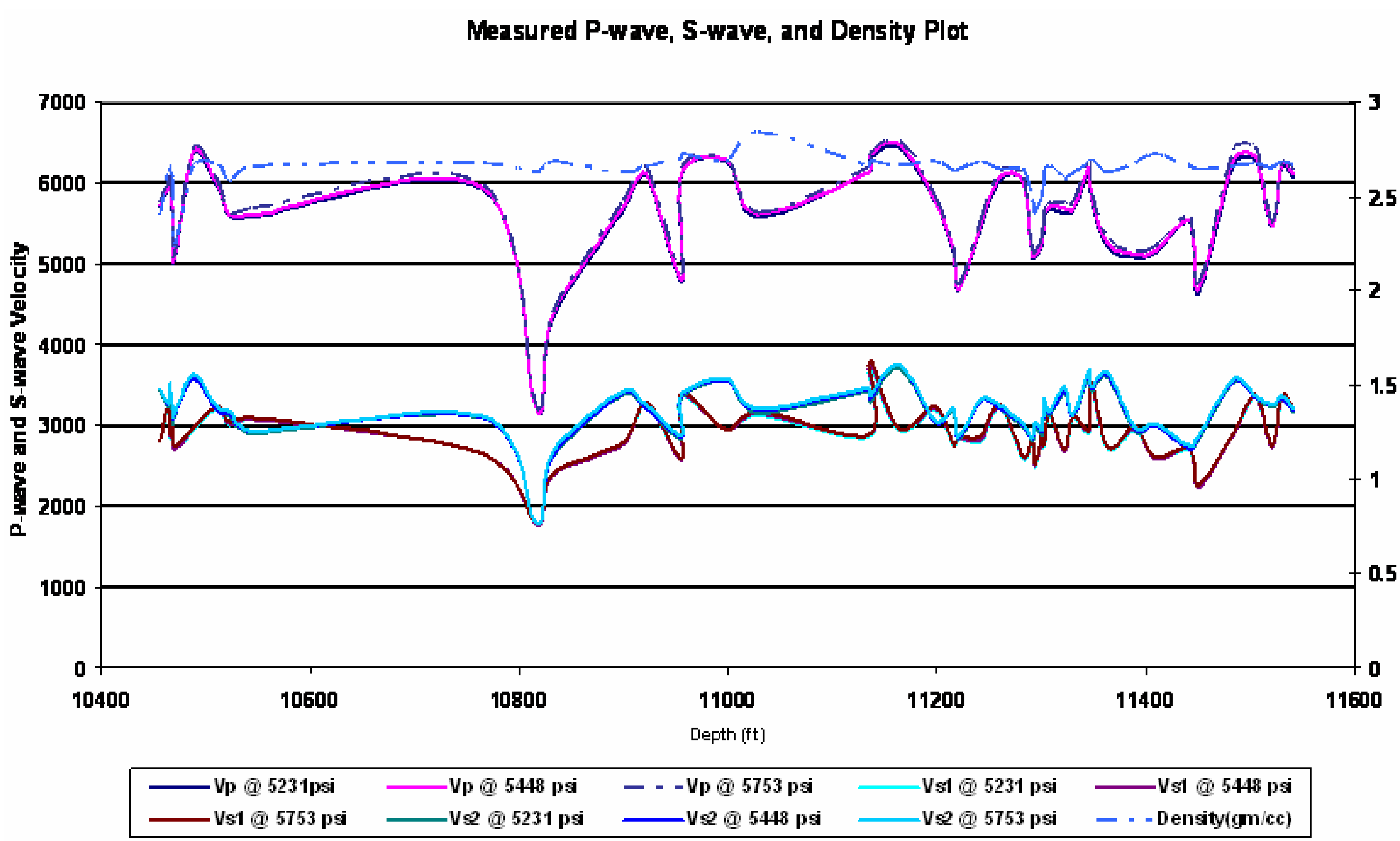

Figure 4.8. P-wave, S-wave and density verses depth plot, figure shows P-wave velocity at top and the two S-wave velocities at the bottom, and density curve shown above P-wave velocity curves.

Depth(ft)	k@ 5231 psi	k@ 5448 psi	k@ 5753 psi	μ_1 @ 5231 psi	μ_1 @ 5448 psi	μ_1 @ 5753 psi	μ_2 @ 5231 psi	μ_2@ 5448 psi	μ_2 @ 5753 psi
10455.3	1.04E+08	1.05E+08	1.05E+08	1.90E+07	1.91E+07	1.91E+07	2.84E+07	2.85E+07	2.85E+07
10464.1	1.32E+08	1.33E+08	1.34E+08	2.79E+07	2.82E+07	2.86E+07	2.78E+07	2.81E+07	2.84E+07
10465.9	1.25E+08	1.25E+08	1.27E+08	2.13E+07	2.15E+07	2.19E+07	3.21E+07	3.23E+07	3.28E+07
10468.7	1.07E+08	1.10E+08	1.10E+08	2.35E+07	2.46E+07	2.46E+07	2.38E+07	2.46E+07	2.49E+07
10470.1	7.87E+07	7.93E+07	8.05E+07	1.64E+07	1.65E+07	1.68E+07	2.15E+07	2.17E+07	2.19E+07
10488.2	1.39E+08	1.40E+08	1.41E+08	2.31E+07	2.33E+07	2.36E+07	3.42E+07	3.41E+07	3.51E+07
10510.5	1.32E+08	1.33E+08	1.35E+08	2.77E+07	2.79E+07	2.79E+07	2.71E+07	2.73E+07	2.78E+07
10523.5	1.11E+08	1.12E+08	1.13E+08	2.32E+07	2.35E+07	2.38E+07	2.51E+07	2.54E+07	2.59E+07
10543.6	1.16E+08	1.17E+08	1.20E+08	2.51E+07	2.53E+07	2.54E+07	2.24E+07	2.26E+07	2.28E+07
10765.7	1.19E+08	1.20E+08	1.21E+08	1.89E+07	1.89E+07	1.90E+07	2.57E+07	2.58E+07	2.60E+07
10816.9	3.77E+07	3.81E+07	3.86E+07	8.27E+06	8.33E+06	8.41E+06	8.37E+06	8.37E+06	8.51E+06
10832	7.07E+07	7.14E+07	7.24E+07	1.53E+07	1.53E+07	1.56E+07	1.84E+07	1.84E+07	1.91E+07
10899.9	1.11E+08	1.12E+08	1.15E+08	2.01E+07	2.02E+07	2.04E+07	3.02E+07	3.04E+07	3.08E+07
10922.1	1.37E+08	1.38E+08	1.40E+08	2.85E+07	2.86E+07	2.89E+07	2.75E+07	2.75E+07	2.81E+07
10954.9	8.55E+07	8.67E+07	8.83E+07	1.79E+07	1.81E+07	1.81E+07	2.21E+07	2.22E+07	2.26E+07
10955.5	1.43E+08	1.44E+08	1.46E+08	3.10E+07	3.12E+07	3.15E+07	3.06E+07	3.09E+07	3.11E+07
10998.3	1.36E+08	1.37E+08	1.37E+08	2.31E+07	2.31E+07	2.33E+07	3.40E+07	3.40E+07	3.43E+07
11027.3	1.26E+08	1.27E+08	1.28E+08	2.81E+07	2.83E+07	2.85E+07	2.85E+07	2.89E+07	2.93E+07
11133.8	1.29E+08	1.30E+08	1.32E+08	2.19E+07	2.21E+07	2.23E+07	3.12E+07	3.15E+07	3.20E+07
11135.9	1.56E+08	1.58E+08	1.60E+08	3.67E+07	3.75E+07	3.84E+07	2.92E+07	2.96E+07	3.04E+07
11163.9	1.41E+08	1.43E+08	1.45E+08	2.29E+07	2.33E+07	2.35E+07	3.68E+07	3.74E+07	3.76E+07
11198.7	1.25E+08	1.26E+08	1.28E+08	2.73E+07	2.76E+07	2.80E+07	2.47E+07	2.49E+07	2.52E+07

Table 4.2 Core samples bulk modulus (k) and shear modulus (μ1 and μ2) at three different pressure points (5231 psi, 5448 psi, and 5753 psi)

Depth(ft)	k@ 5231 psi	k@ 5448 psi	k@ 5753 psi	μ_1 @ 5231 psi	μ_1 @ 5448 psi	μ_1 @ 5753 psi	μ_2 @ 5231 psi	μ_2@ 5448 psi	μ_2 @ 5753 psi
11214.8	9.68E+07	9.78E+07	9.94E+07	2.00E+07	2.02E+07	2.03E+07	2.68E+07	2.70E+07	2.73E+07
11220.5	8.62E+07	8.72E+07	8.85E+07	2.14E+07	2.16E+07	2.18E+07	2.12E+07	2.14E+07	2.16E+07
11242.5	1.08E+08	1.09E+08	1.12E+08	2.13E+07	2.14E+07	2.20E+07	2.93E+07	2.94E+07	2.98E+07
11259.5	1.34E+08	1.35E+08	1.38E+08	2.78E+07	2.79E+07	2.82E+07	2.73E+07	2.75E+07	2.80E+07
11283.2	1.19E+08	1.20E+08	1.22E+08	1.79E+07	1.80E+07	1.81E+07	2.35E+07	2.38E+07	2.40E+07
11290.8	8.97E+07	9.09E+07	9.22E+07	1.95E+07	1.98E+07	2.00E+07	1.95E+07	1.98E+07	2.02E+07
11293.5	8.20E+07	8.28E+07	8.42E+07	1.50E+07	1.50E+07	1.52E+07	2.15E+07	2.19E+07	2.24E+07
11300.9	9.65E+07	9.81E+07	1.00E+08	2.08E+07	2.10E+07	2.14E+07	2.12E+07	2.14E+07	2.19E+07
11301.5	1.06E+08	1.08E+08	1.09E+08	1.96E+07	1.98E+07	1.99E+07	2.83E+07	2.86E+07	2.89E+07
11307.9	1.21E+08	1.22E+08	1.24E+08	2.62E+07	2.64E+07	2.66E+07	2.63E+07	2.64E+07	2.67E+07
11322	1.07E+08	1.09E+08	1.12E+08	1.85E+07	1.86E+07	1.89E+07	3.00E+07	3.04E+07	3.15E+07
11330.2	1.17E+08	1.18E+08	1.21E+08	2.51E+07	2.53E+07	2.55E+07	2.53E+07	2.56E+07	2.58E+07
11345.6	1.31E+08	1.34E+08	1.37E+08	2.26E+07	2.28E+07	2.32E+07	3.52E+07	3.59E+07	3.66E+07
11347.7	1.33E+08	1.34E+08	1.37E+08	3.23E+07	3.26E+07	3.32E+07	3.19E+07	3.23E+07	3.28E+07
11363	9.71E+07	9.85E+07	1.00E+08	1.93E+07	1.95E+07	1.97E+07	3.41E+07	3.45E+07	3.50E+07
11390.6	1.00E+08	1.01E+08	1.03E+08	2.33E+07	2.35E+07	2.39E+07	2.29E+07	2.31E+07	2.34E+07
11408	9.60E+07	9.70E+07	9.87E+07	1.82E+07	1.83E+07	1.85E+07	2.45E+07	2.46E+07	2.49E+07
11442.1	1.07E+08	1.08E+08	1.09E+08	1.92E+07	1.95E+07	1.97E+07	1.95E+07	1.97E+07	2.02E+07
11450.9	7.43E+07	7.58E+07	7.76E+07	1.32E+07	1.32E+07	1.34E+07	2.12E+07	2.14E+07	2.18E+07
11484.2	1.33E+08	1.35E+08	1.39E+08	2.20E+07	2.22E+07	2.26E+07	3.32E+07	3.37E+07	3.40E+07
11504.5	1.46E+08	1.48E+08	1.53E+08	3.01E+07	3.04E+07	3.09E+07	2.99E+07	3.00E+07	3.04E+07
11520	1.05E+08	1.06E+08	1.08E+08	1.98E+07	1.99E+07	2.01E+07	2.77E+07	2.79E+07	2.81E+07
11529.4	1.43E+08	1.44E+08	1.45E+08	2.97E+07	3.00E+07	3.03E+07	2.96E+07	2.98E+07	3.03E+07
11541.1	1.35E+08	1.37E+08	1.38E+08	2.73E+07	2.74E+07	2.77E+07	2.70E+07	2.73E+07	2.77E+07

Table 4.2 Continued

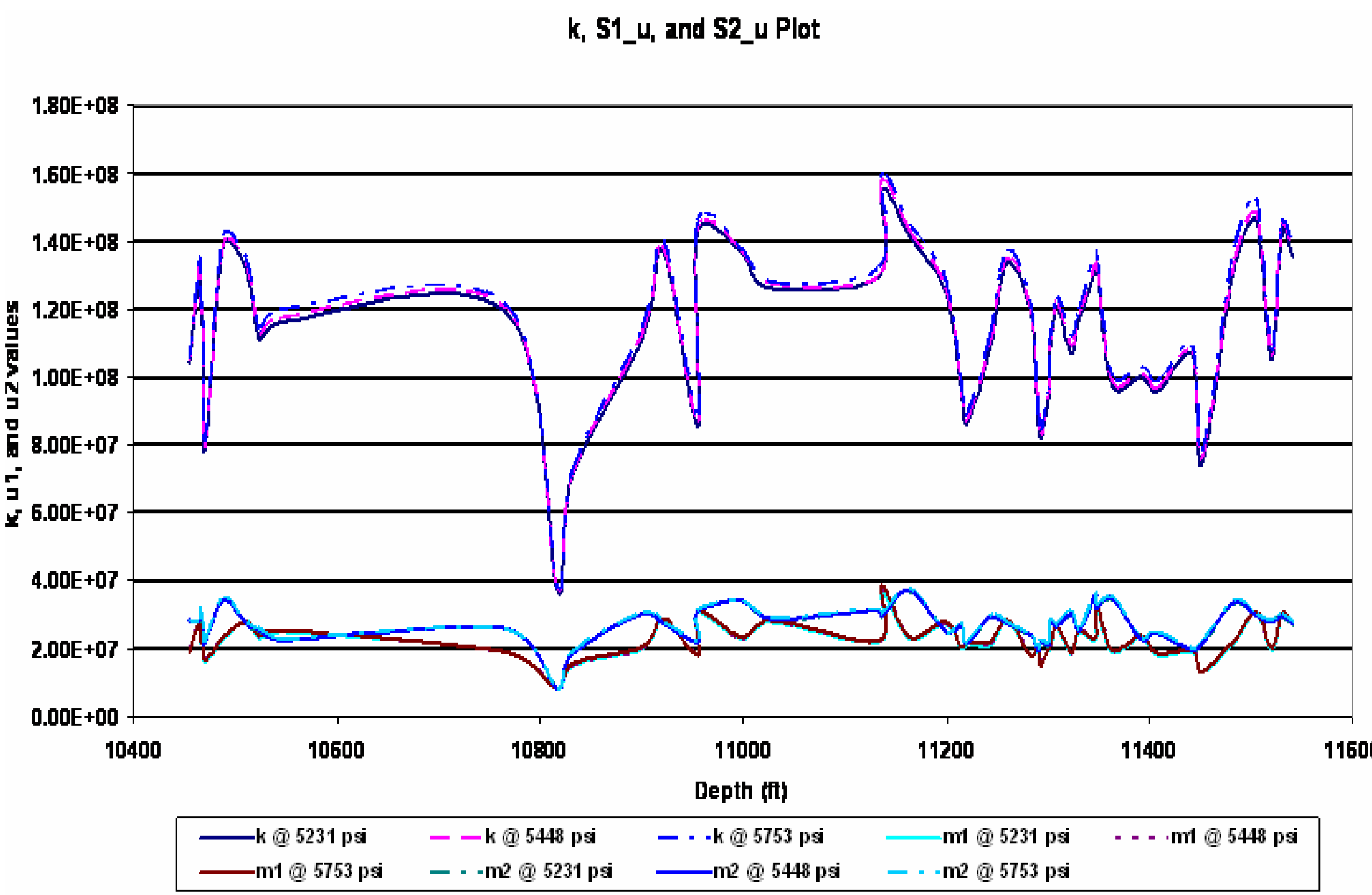

Figure 4.9. Bulk modulus (k) and shear modulus (μ) verses depth plot, figure shows k at top, and the two μ at the bottom.

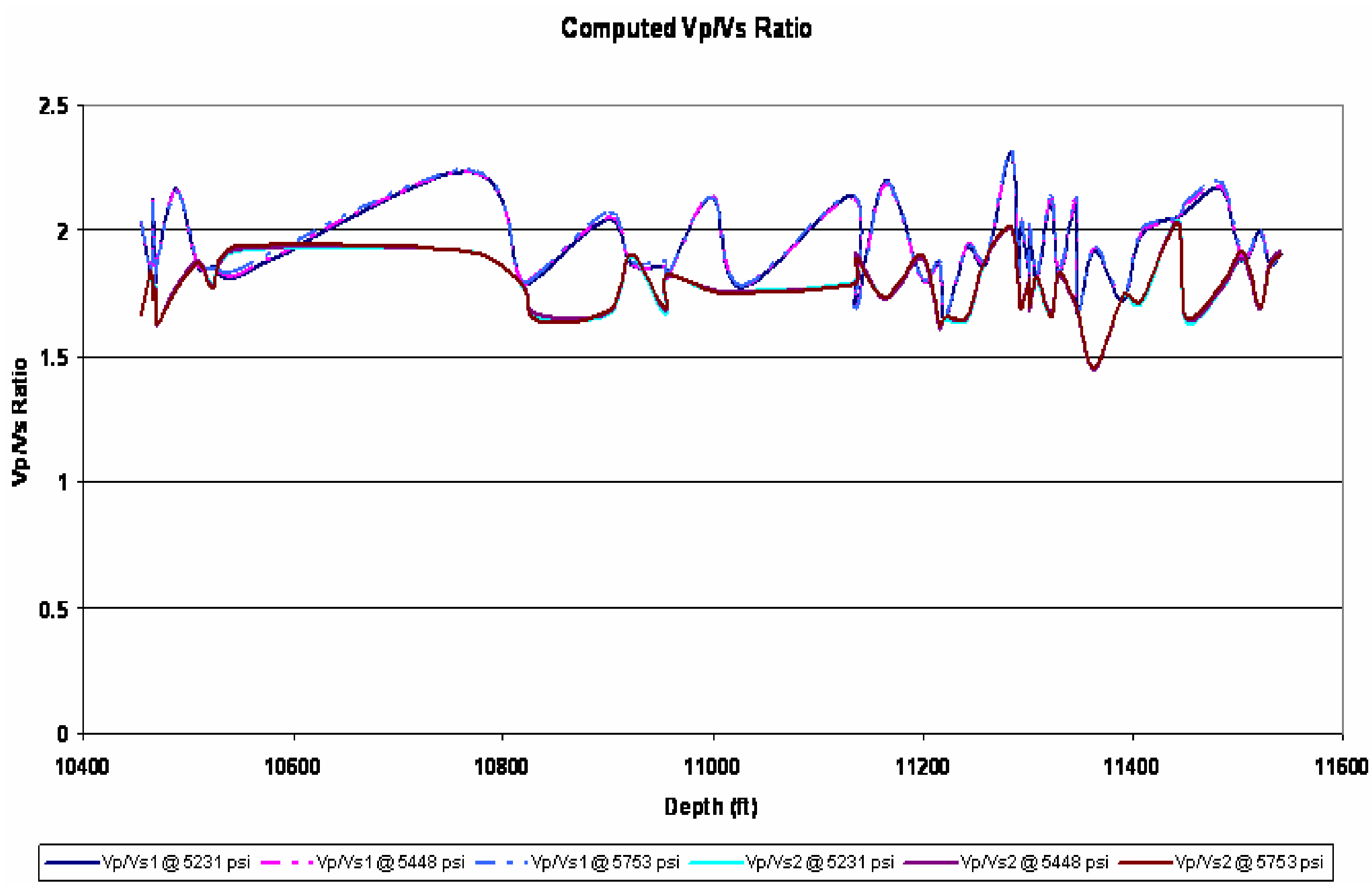

Figure 4.10. V_p/V_s plot verses depth, figure shows V_p/V_{s1} at top and the V_p/V_{s2} at the bottom.

4.6 Attenuation Measurement

In the laboratory attenuation is generally measured by one of several techniques. These include the resonant bar method (Birch and Bancroft, 1938; Born, 1941; Gardner et al., 1964; Spetzler and Anderson, 1968); amplitude decay of multiple reflections (Peselnick and Zietz, 1959); slow stress strain cycling (Jackson, 1969); or a pulse transmission method (Kuster and Toksoz, 1974; Tittman et al., 1974; Watson and Wunschel, 1973). Accurate measurement of intrinsic attenuation is a tricky task and it seriously limits the utilization of anelastic rock properties, both in the laboratory and in the field. Seismic wave amplitudes are strongly affected by geometric spreading, reflection, and scattering in addition to intrinsic attenuation. So, it is important to account for the aforementioned factors while calculating intrinsic attenuation and quality factor. By using a reference sample, such as aluminum, with very small attenuation ($\alpha \approx 0$) and similar geometry to the sample, the geometric and transmission loss can be resolved. In addition, the pulse transmission technique is most suited for use in pressure vessels with jacketed and saturated samples (Figures 4.5), provided correction can be made for geometric factors such as beam spreading and reflections as mentioned above.

A pulse transmission technique, is the method used in this work to measure attenuation coefficient (α) and quality factor (Q), where the amplitude decay of a seismic signal traveling through a sample is measured at the opposite end. In the pulse transmission technique a spectral ratio method is applied to compute α and Q. Spectral ratio is by far the most common technique used in seismology, and it allows for the elimination of many of the problem associated with other wave-propagation methods (Toksoz et al., 1979), where a reference sample such as aluminum with similar geometry is measured together with the desired sample. In the spectral ratio method, the log amplitude spectral ratio of a reference sample to a core sample is plotted against the frequency of the pulse. From the slope of this plot the α of the sample is calculated. Then Q is computed from the α value obtained. This technique relies on the fact that high frequencies are preferentially attenuated relative to low frequencies. A media with high intrinsic attenuation (α), or low quality factor (Q) dissipate more than those media with low (α). In general, the spectral amplitude of a propagating wave in a given media at a given frequency may be expressed by equation 4.1, (Ward and Toksoz 1971).

Equation 4.1

$$A(f,x) = GA_r(f)\exp(-\alpha^* f)$$

where G includes geometric spreading, and transmission and reflection coefficients. A_r is the receiver response and α* is given by equation 4.2.

Equation 4.2 Attenuation

$$\alpha = \pi \int_{path} dx / QV$$

This is valid for frequency independent Q. In addition, the above expression is also valid for slowly varying Q in the frequency band of interest. For a plane wave propagating through a medium (reference sample such as aluminum) placed in between two transducers (i.e. a source transducer and a receiver transducer) the wave power spectrum including the geometric factor at the receiver transducer is expressed as

Equation 4.3 Amplitude power spectrum for reference sample

$$A_r(\omega) = S(\omega)e^{-\alpha_r(\omega)D}G_r(\lambda_r aD)T_{r1}T_{r2}$$

where αr is the attenuation coefficient of the reference sample; *D* is the length of the reference sample; T_{r1} and T_{r2} are the transmission coefficients from the transmitter endcap to the reference sample and from the reference sample to the receiver endcap; and $G_r(\lambda r,a,D)$ is a geometric diffraction correction term. The geometric diffraction correction is a function of the wave length term $\lambda_r = V_r/f_c$, and radius of the sample (a). The same way for a plane wave propagating in a rock sample the power spectrum can be given by equation 4.4.

Equation 4.4

$$A_s(\omega) = S(\omega)e^{-\alpha_s(\omega)D}T_{s1}T_{s2}G_s(\lambda_s, a, D)$$

where S(ω) is the power spectra of the source wave; α_s is the attenuation coefficient of the measured rock sample; L is the length of the rock sample; T_{s1} and T_{s2} are the transmission coefficients from the transmitter endcaps into the rock sample and from the rock sample into the receiver endcaps respectively; and Gs(λs,a,α) is the geometric diffraction correction term. Since the $T_{r1} = 1 - R_{r1}$, and $T_{r2} = 1 - R_{r2}$; and $R_{r1} = - R_{r2}$, which is the same for the measured rock sample, the ratio of the power spectra of the sample to the reference sample, after taking the logarithm, and dropping attenuation of the reference sample ($\alpha_r \approx 0$), the attenuation of the rock sample can be expressed by equation 4.4.

Equation 4.4

$$\alpha_s(\omega) = \frac{1}{D}Ln\left[\frac{A_r(\omega)}{A_s(\omega)}\frac{(1-R_s^2)}{\left(1-R_r^2\right)}\right] - \frac{1}{D}Ln\left[\frac{G_s\left(\lambda_s, a, D\right)}{G_s\left(\lambda_s, a, D\right)}\right]$$

If the geometric shape of the reference sample and the rock sample are the same, and measurement on both samples is conducted under identical environment, then the geometric diffraction loss term in equation 4.4 reduces to 0, and equation 4.4 can be rewritten as equation 4.5.

Equation 4.5 Equation for α can be obtained from the slope of the log ratio

$$\alpha_s(\omega) = \frac{1}{D} Ln\left[\frac{A_r(\omega)}{A_s(\omega)} \frac{(1-R_s^2)}{\left(1-R_r^2\right)}\right]$$

then the quality factor of the rock sample can be expressed by Equation 4.6.

Equation 4.6 quality factor (Q) in terms of attenuation coefficient α per wavelength.

$$\frac{1}{Q} = \frac{\alpha(dB/\lambda)}{8.686\pi}$$

4.7 Results and Discussion

Pulse transmission technique with spectral ratio is used to determine attenuation coefficients and quality factor (Q) values relative to a reference sample with a very low attenuation (e.g. aluminum). The samples used in this acoustic measurement system are cylindrical samples with 2.54 cm diameter, and variable in length. Transmitter and receiver transducers, each 2.54 cm in diameter, are mounted at opposite ends of the sample (Figure 4.4). During velocity and attenuation coefficient computation only one way travel time is measured. However, for attenuation coefficient calculation two-way transmission loss effect is considered (equation 4.5). The sample to be studied and the reference samples have exactly the same geometry and shape (Figure 4.11). Essentially, two measurements are made using identical procedure, one on the rock sample of interest and the second on the reference sample (aluminum). In Figure 4.8 P-wave and S-wave velocities, and density verses depth of core samples are shown. According to the figure no significant change on both P-wave and S-wave velocities is observed due to pressure change. All the P-wave and S-wave velocities at different pressure (5231 psi, 5448 psi, and 5753 psi) plot together. The velocities for both the reference and core sample are calculated from the first break travel time (Figure 4.7), which is the one way travel time through either the core sample or reference sample plus the travel time through the endcaps (equation 4.1). Figure 4.12 shows two plots of time-trace amplitude verses time, the first for the core sample and the second for the reference sample. Transmission loss corrections are applied to both the reference and core sample amplitude, because the endcaps are made of titanium alloy. The time-trace plots given for both the reference and core sample are plotted amplitude verses one-way time. Furthermore, these traces include multiples, and only those multiples which are clearly identified are marked. Attenuation coefficients for the core sample are calculated from the log amplitude spectral ratio slope of the reference sample and core sample (Figure 4.13a and b). From the computed attenuation coefficients quality factor (Q) values for each sample is calculated using the relation given in Equation 4.6. In addition, the Q values calculated are for P-wave (Q_p) and S-waves (Q_s), these values are given in Table 4.3. Figure 4.14 show V_p/V_s and Q_p/Q_s, porosity, and permeability verses depth plots. Based on the observation from the plots in Figure 4.13, there is a general correlation between low V_p/V_s and Q_p/Q_s and high porosity and permeability (green circled regions). Thus, the observed porosity and permeability values of the samples are characterized by very low porosity and permeability. Porosity values show a wide range of variation, but very few samples have porosity value greater then 5 percent, while most samples have porosity value ranging between 1.5 and 5 percent.

Similarly, permeability of the samples displays wide variations, but only a handful of samples have permeability value greater than 3 mD. Most of the samples have permeability less than 0.1 mD. In Figure 4.15, V_p/V_s and Q_p/Q_s verses porosity are plotted, and from the plot very little relation can be seen. However, in Figure 4.16 V_p/V_s and Q_p/Q_s verses permeability values are plotted and there is a better relationship. In general, the trend observed is a decrease in both porosity and permeability with increasing V_p/V_s and Q_p/Q_s.

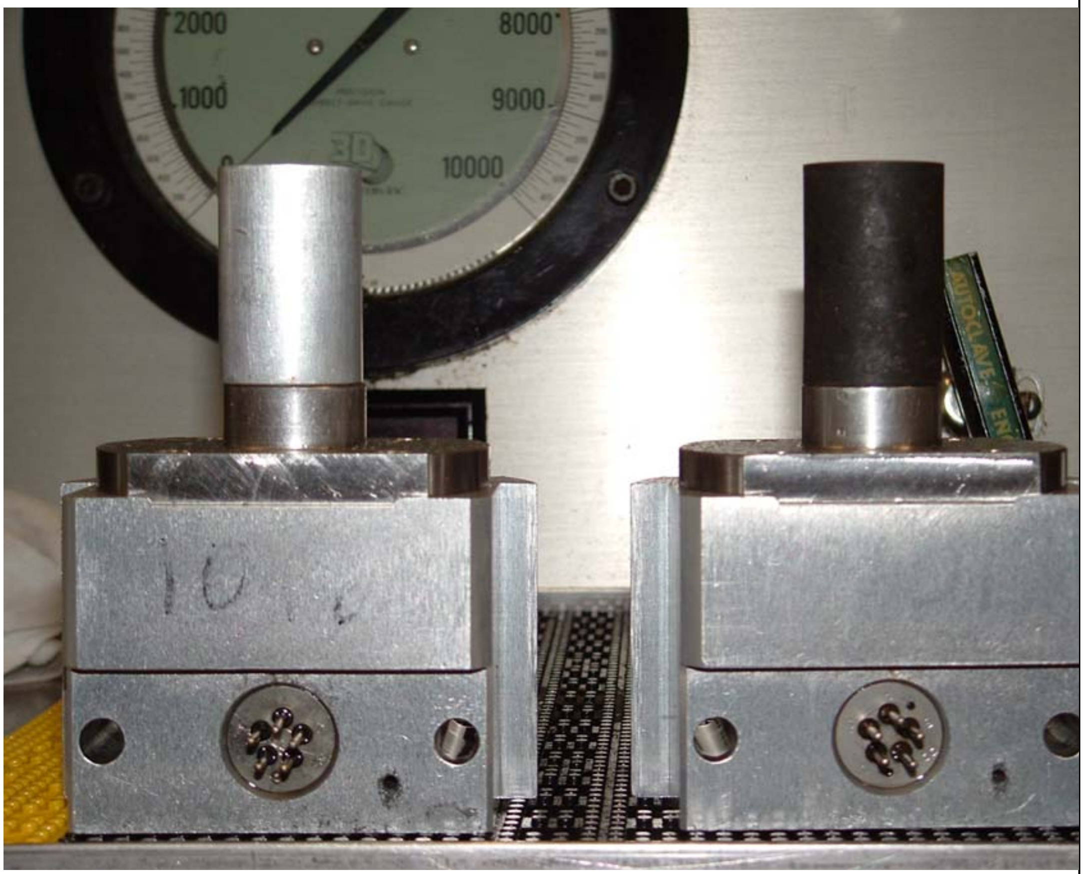

Figure 4.11 Reference sample (aluminum) left, and core sample right.

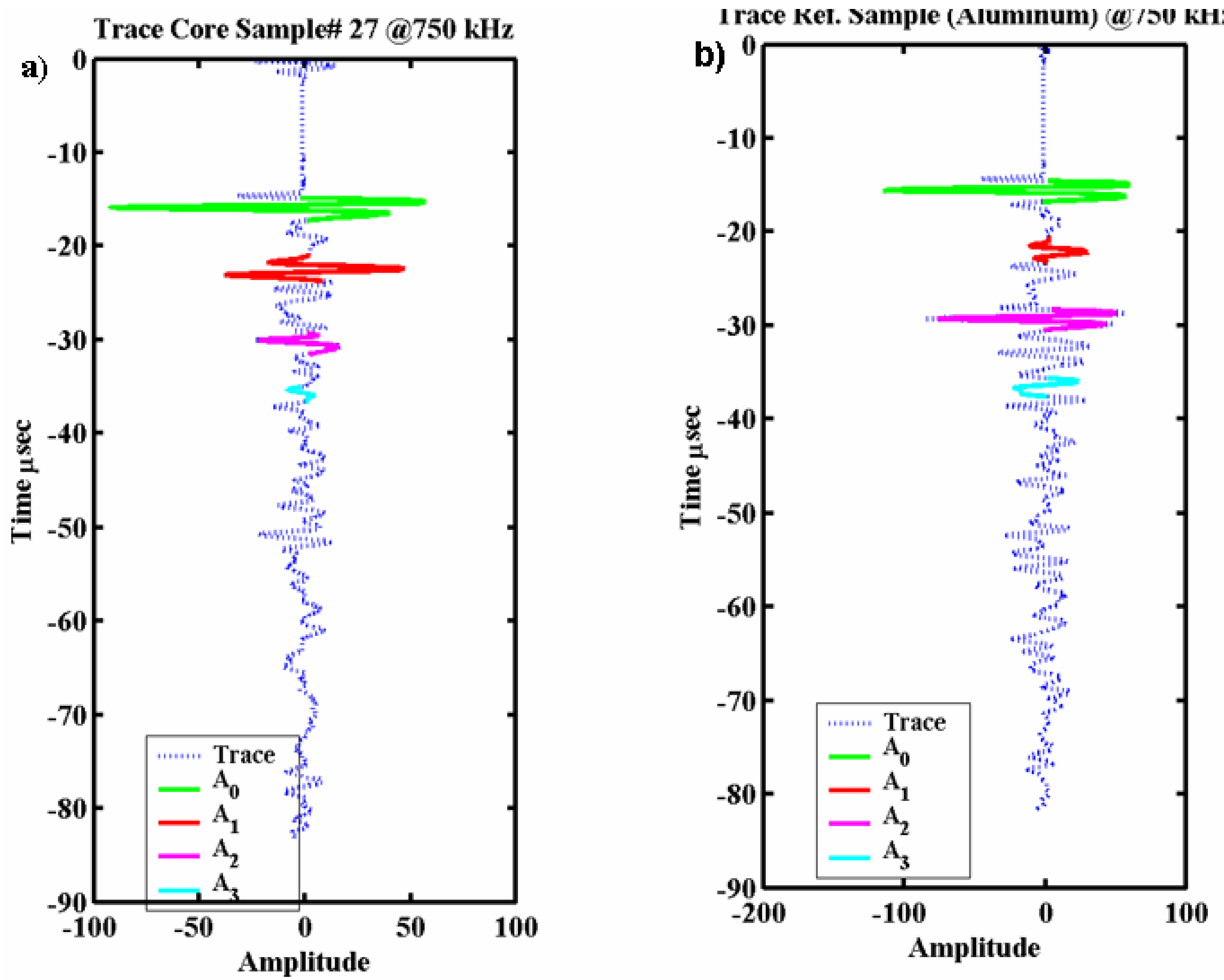

Figure 4.12. Traces of a) core sample # 27, and b) reference sample (aluminum) measurement were done at 750 kHz, trace shows first break (green), primary reflector (red), and multiples (magenta and cyan).

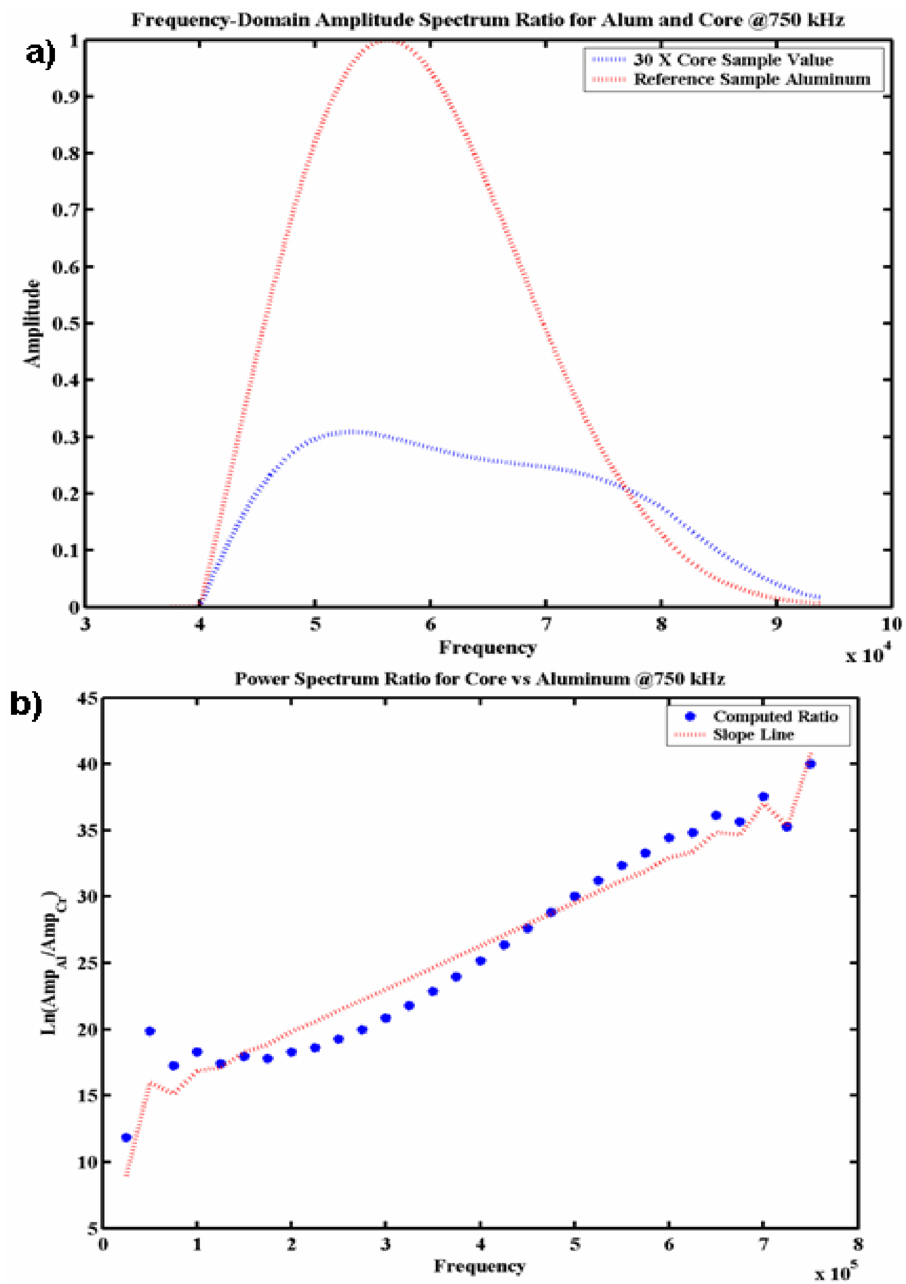

Figure 4.13. a) Frequency-domain amplitude spectrum for reference sample (red), and core sample (blue); b) log amplitude spectral ratio of aluminum and core sample.

Depth	Vp5231/Vs5231	Qp/5231/Qs5231	Porosity	Permeability
10455.3	2.04	3.70	1	0.002
10464.1	1.84	0.78	2.8	0.02
10465.9	2.13	1.12	2.8	0.1
10468.7	1.79	0.51	3	1
10470.1	1.86	1.08	4	3
10488.2	2.17	0.45	1.5	0.15
10510.5	1.85	2.31	2	2
10523.5	1.86	2.45	2.2	0.6
10543.6	1.81	1.59	4	0.008
10765.7	2.24	2.46	2	0.015
10816.9	1.80	8.64	4	0.004
10832	1.81	1.18	1.5	0.05
10899.9	2.05	1.46	3.5	3
10922.1	1.86	1.77	1.5	0.3
10954.9	1.86	2.40	1	0.005
10955.5	1.81	5.68	2	0.03
10998.3	2.13	1.63	1.2	0.003
11027.3	1.78	1.01	6	6
11133.8	2.14	1.54	1	0.15
11135.9	1.71	1.08	1	0.15
11163.9	2.20	1.11	1.5	1
11198.7	1.80	1.23	1.2	0.002
11214.8	1.87	3.87	3.5	0.008
11220.5	1.64	1.80	2.5	0.08
11242.5	1.94	1.00	4	0.15
11259.5	1.87	2.55	3	0.05
11283.2	2.31	1.11	2.2	0.02
11290.8	1.81	1.85	4	0.9
11293.5	2.04	2.84	4	1
11300.9	1.82	4.67	7	0.1
11301.5	2.02	0.50	7	0.1
11307.9	1.81	2.27	3.5	0.015
11322	2.11	2.49	3.2	0.015
11330.2	1.83	0.99	3.2	0.008
11345.6	2.11	5.42	2	0.006
11347.7	1.67	5.12	2	0.006
11363	1.92	1.47	1.5	0.006
11390.6	1.72	1.39	1.5	0.01
11408	1.98	0.44	6	0.05
11442.1	2.06	0.60	1.5	0.003
11450.9	2.07	1.72	3	0.4
11484.2	2.17	2.91	3	0.03
11504.5	1.88	5.33	2	0.005
11520	2.00	1.48	1.5	0.005
11529.4	1.86	0.71	3	0.3
11541.1	1.90	2.11	0.5	0.05

Table 4.3 Core sample V_p/V_s, Q_p/Q_s, porosity and permeability with sample depth (after Murat, 2001).

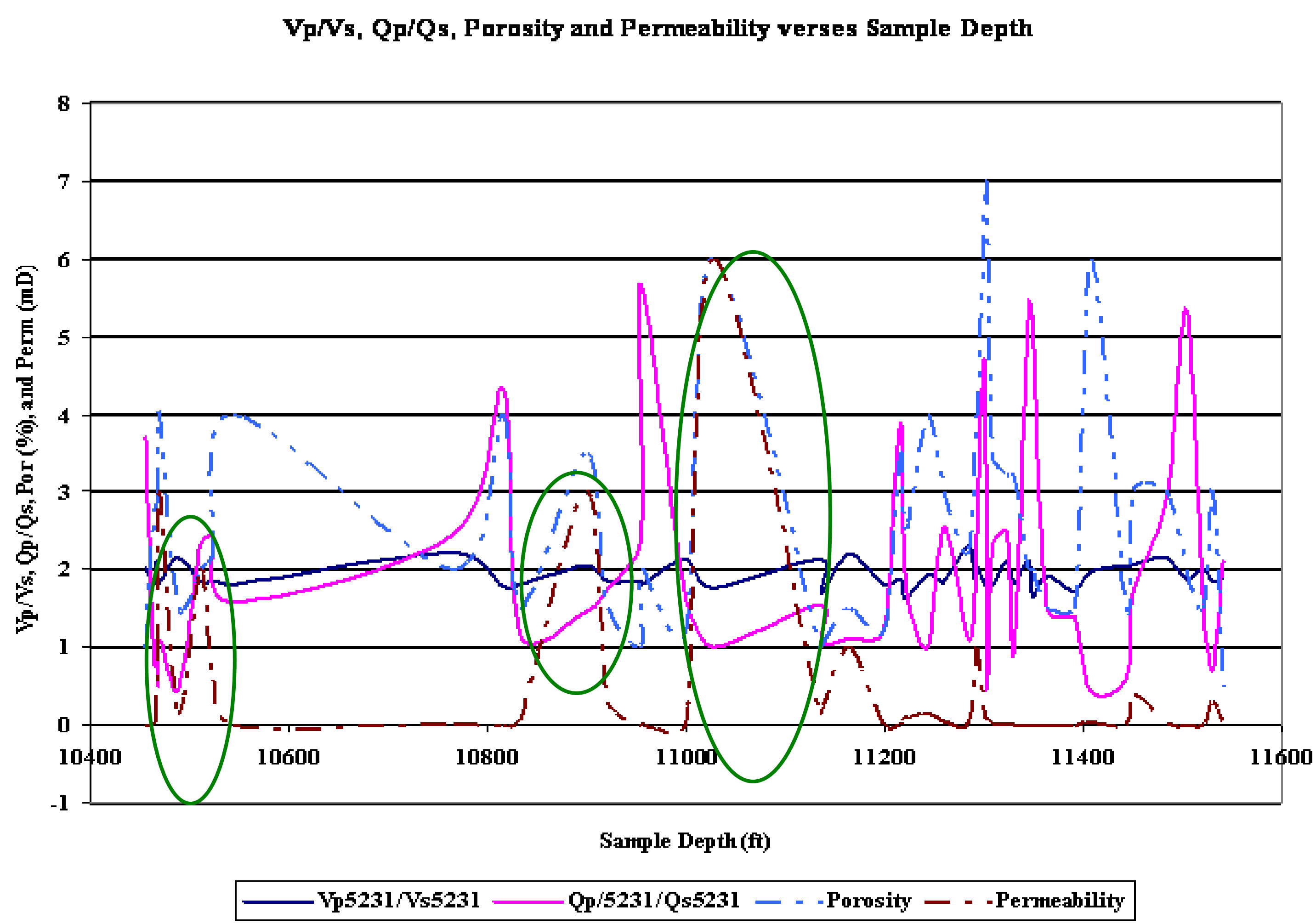

Figure 4.14. P-wave and S-wave velocity ratio, P-wave and S-wave quality factor ratio, porosity and permeability verses depth plot.

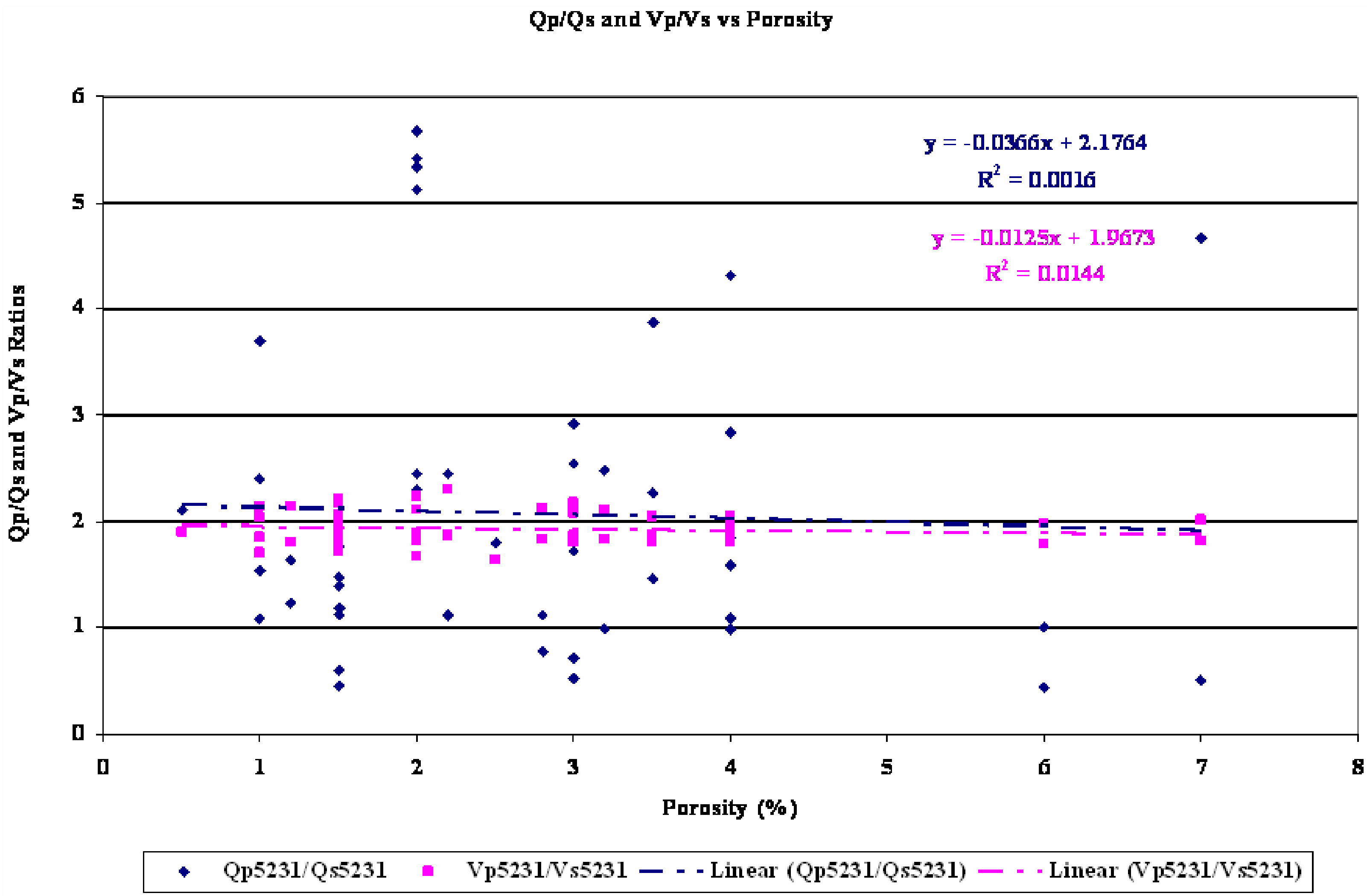

Figure 4.15. Q_p/Q_s and V_p/V_s vs Porosity plots; regression lines drawn for both Q_p/Q_s (blue) and V_p/V_s (magenta).

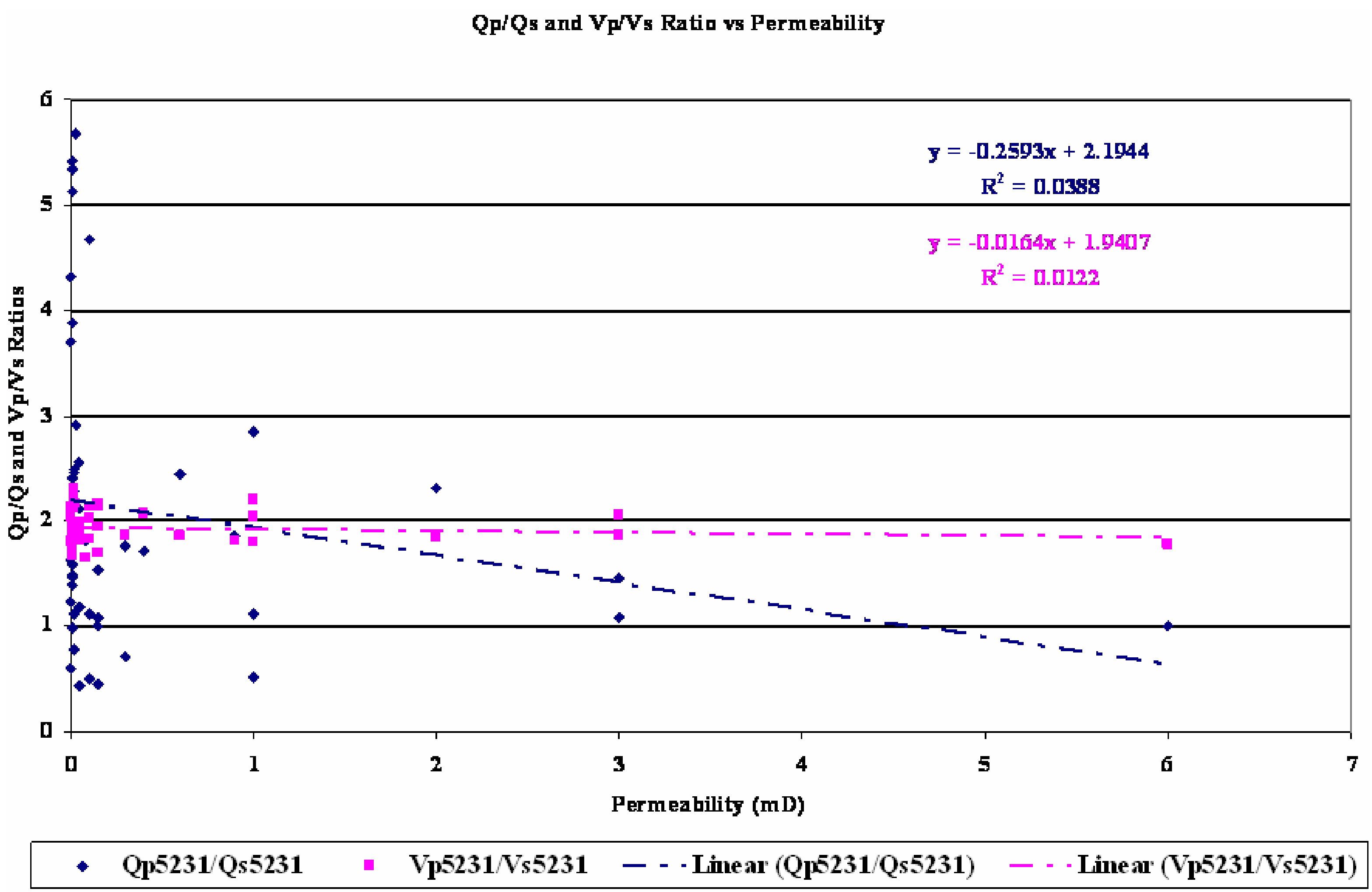

Figure 4.16. Q_p/Q_s and V_p/V_s vs Permeability; regression lines drawn for both Q_p/Q_s (blue) and V_p/V_s ratio (magenta).

4.8 Summary and Conclusions

Rocks can be distinguished by their velocity, density, elastic parameters and anelastic parameters. Furthermore, rock properties, lithology, physical state and degree of saturation can be characterized by the above mentioned parameters. Anelastic parameters of a rock include attenuation coefficient (α), the exponential decay constant of the amplitude of a plane wave propagating in a homogeneous medium, and quality factor (Q), the internal friction or dissipation factor. Laboratory measurement, on core samples and reference samples (aluminum), using pulse-through transmission technique, allowed computation of P-wave and S-wave velocities, and compressional and shear quality factors. Corrections such as geometric spreading are accomplished by using the reference sample. In addition, transmission loss correction is done based on the knowledge of sample and endcap velocities and density information. Computed results of V_p, V_s, Q_p, Q_s, V_p/V_s, and Q_p/Q_s for each sample plotted verses sample depth have indicated their relationship with the available porosity and permeability information. Therefore, if properly computed, V_p, V_s, Q_p, Q_s, V_p/V_s, and Q_p/Q_s can be used to characterize a reservoir formation in conjunction with other hydrocarbon indicators.

Chapter 5

GEOLOGICALLY CONSTRAINED, ESTIMATION AND ANALYSIS OF QUALITY FACTOR (Q) FROM SONIC LOG AND 3D SEISMIC DATA

5.1 Introduction

Quality factor (Q) values are estimated from full-wave sonic log and 3D reflection seismic data, and results are compared to Q values from 46 core samples collected from the same well. The compressional and shear wave sonic log, and density log recorded in Well C-276 between the 10400 ft and 11600 ft interval are used to compute compressional wave quality factor (Q_p) and shear wave quality factor (Q_s). In addition, Q_p is estimated from a CMP-gather extracted from 3D reflection seismic data. Reliable estimation of quality factor from seismic data can lead to improved methods for the prediction of petrophysical properties.

Reflection seismic amplitude decay results from a number of decay processes. These factors include spherical divergence, transmission loss, intrinsic attenuation (frictional adsorption), dispersion (stratigraphic filter), and mode conversion. Spherical divergence and transmission loss decays are generally redistribution of seismic energy, and they are balanced during seismic processing. Amplitude balance (Program Gain Control), and noise filtering (General Purpose Band-pass Filter) processes are performed on the CMP-gathers. On the other hand, intrinsic attenuation, dispersion and mode conversion involve energy transformation. The intrinsic attenuation, quantified by quality factor (Q) has a significant impact on surface reflection seismic data (Dasgupta and Clarks, 1998). Furthermore, the anelastic loss of seismic energy is linked to petrophysical properties such as porosity, permeability and clay content (Murphy, 1982 and 1984; Peacock, et al., 1994; Best, et al., 1994; Best and McCann, 1995; and Dasios et al., 2001). In addition, the frictional absorption preferentially attenuates the high frequencies, and thus this lengthens the dominant signal wavelength and period, which degrades resolution. However, by applying inverse Q filtering to the seismic data, the quality can be enhanced, and the resolution of the seismic section improved.

Attenuation measurements together with other hydrocarbon indicators (DHI) can be useful as they may find application in the following fields: reservoir characterization for predicting petrophysical properties from seismic data; over pressure zone detection; time-laps methods for improving detection and monitoring of petroleum production.

5.2 Objectives

The objective of this work is, in the first part, to compute quality factor (Q) from the sonic log from Well C-276, and then correlate the result to Q values calculated from core samples of the same well. In the second part, Q values from reflection seismic CMP-gathers are estimated, and then correlated with estimated Q values to Q values for Well C-276. Finally, the calculated Q values from the well are applied for inverse Q filtering CMP-gathers, extracted from a 2D line close to Well C-276, which is extracted from a 3D seismic volume.

5.3 Quality Factor (Q) Estimation from the Well-Log

Compressional and shear wave attenuation, quantified by quality factor (Q), are estimated from the full-wave sonic from Well C-276. The computation is performed using the log spectral ratio (LSR) method. The LSR method estimates attenuation by comparing the amplitude spectra of two pulses measured at two different receivers. The pulses are generated from the same source. Attenuation is estimated by applying least-square linear regression fitted to the logarithm of the spectral ratio of the two pulses within the selected frequency band. The LSR method is based on the equation given below (Dasios et al., 2001), equation 5.1.

$$\ln \frac{|A(\omega, x)|}{|A(\omega, x_r)|} = \ln \frac{|G|}{|G_r|} - \frac{\omega}{\omega_r}\left(t^* - t_r^*\right)$$

where $A(\omega,x)$ and $A(\omega,x_r)$ are the amplitude spectra for two receivers at distance x and x_r, respectively from the source, while G and G_r are the geometric spreading factors, which are assumed frequency independent, and ω is the radial frequency. Then t^* is the cumulative attenuation given by equation 5.2

$$t^* = \int \frac{Q^{-1}(s)}{v(s)} ds$$

where Q(s) is the quality factor, $v(s)$ is the velocity and s is distance traveled by the ray path.

For estimation of Q_p and Q_s from Well C-276, the amplitude spectra of both the P-wave and S-wave arrivals from a reference receiver 1 (near-offset) and target receiver 8 (far-offset) are used. Then, attenuation coefficient (α) is calculated from the slope of the least square regression line of the logarithm of the spectral ratio plotted against the selected frequency bandwidth. In addition, for the given frequency range Q is assumed independent of frequency.

In Figures 5.1a and b P- and S- sonic velocities (blue dashed lines) from Well C-276 are shown for the section between 10300 ft and 11600 ft. In addition, P- and S-wave velocities (green dots) measured from core samples in the same interval are overlain on the same figures for correlation. From Figure 5.1a it can be observed that there is a good correlation between P-wave sonic velocity and P-wave velocity from core sample. However, the correlation between S-wave sonic velocity and S-wave velocity from the core samples is relatively poor. The density log from Well C-276 (blue dashed line) is shown in Figure 5.2, and the density values (green dots) measured from the core samples are also superimposed on the density log. The two density measurements, the log and core samples, show a very good correlation. Figures 5.3a and b show both reflectivity series and synthetic seismogram for the section between 10300 ft and 11600 ft, generated from the density and velocity information in Figures 5.1 and 5.2. The synthetic trace is filtered using a zero phase 50 Hz filter. Quality factor values are computed for both P- and S-wave sonic logs, and are presented on

Figures 5.4a and b (blue dashed lines). In addition, P- and S-wave Q values measured from the core samples (green dots) are overlain onto the P- and S-wave sonic Q graphs. Based on observation from Figure 5.4a and b, there is a good match between Q_p and Q_s from sonic and Q_p and Q_s from core samples. However, upon close investigation Q_p from sonic and Q_p from core samples show better correlation compared to Q_s from sonic and Q_s from core samples.

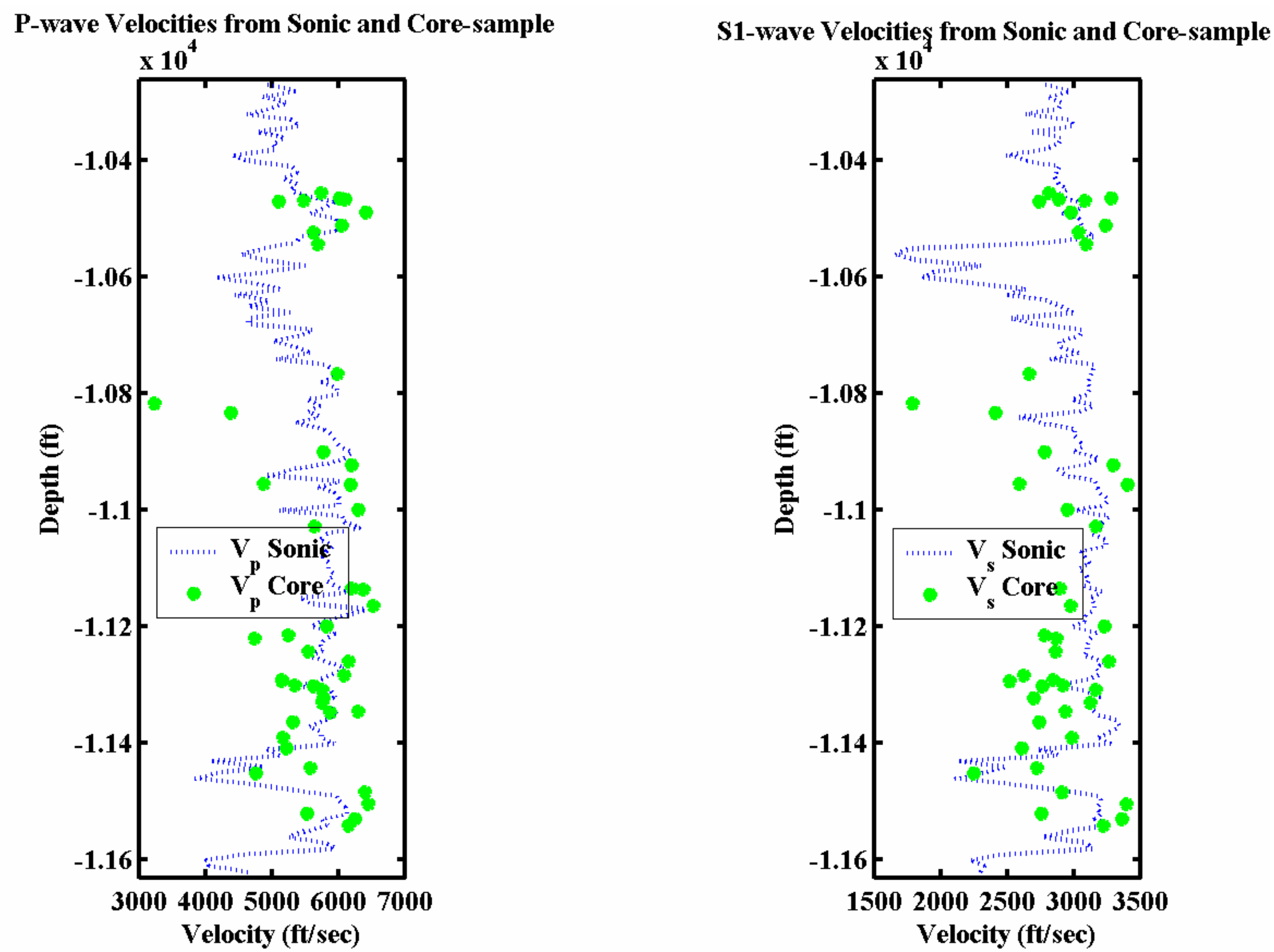

Figure 5.1 P- and S- wave sonic velocities (blue dashed lines), and P- and S-wave velocities from core samples (green dots) from Well C-276, a) P-wave sonic and P-wave core sample velocities, b) S-wave sonic and core sample velocities.

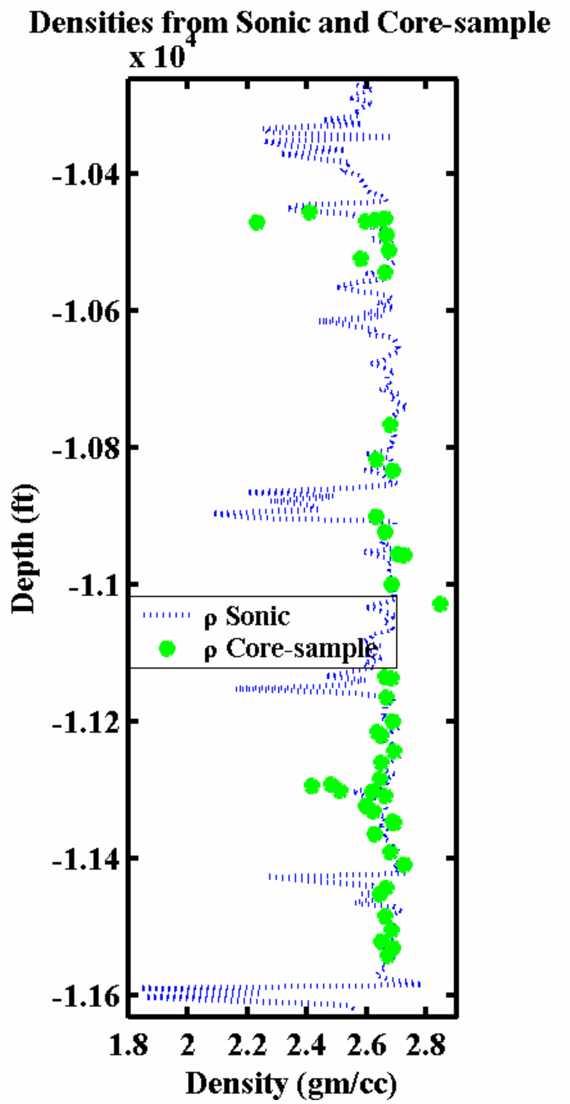

Figure 5.2 Density log (blue dashed line), and density from core samples (green dots) from Well C-276.

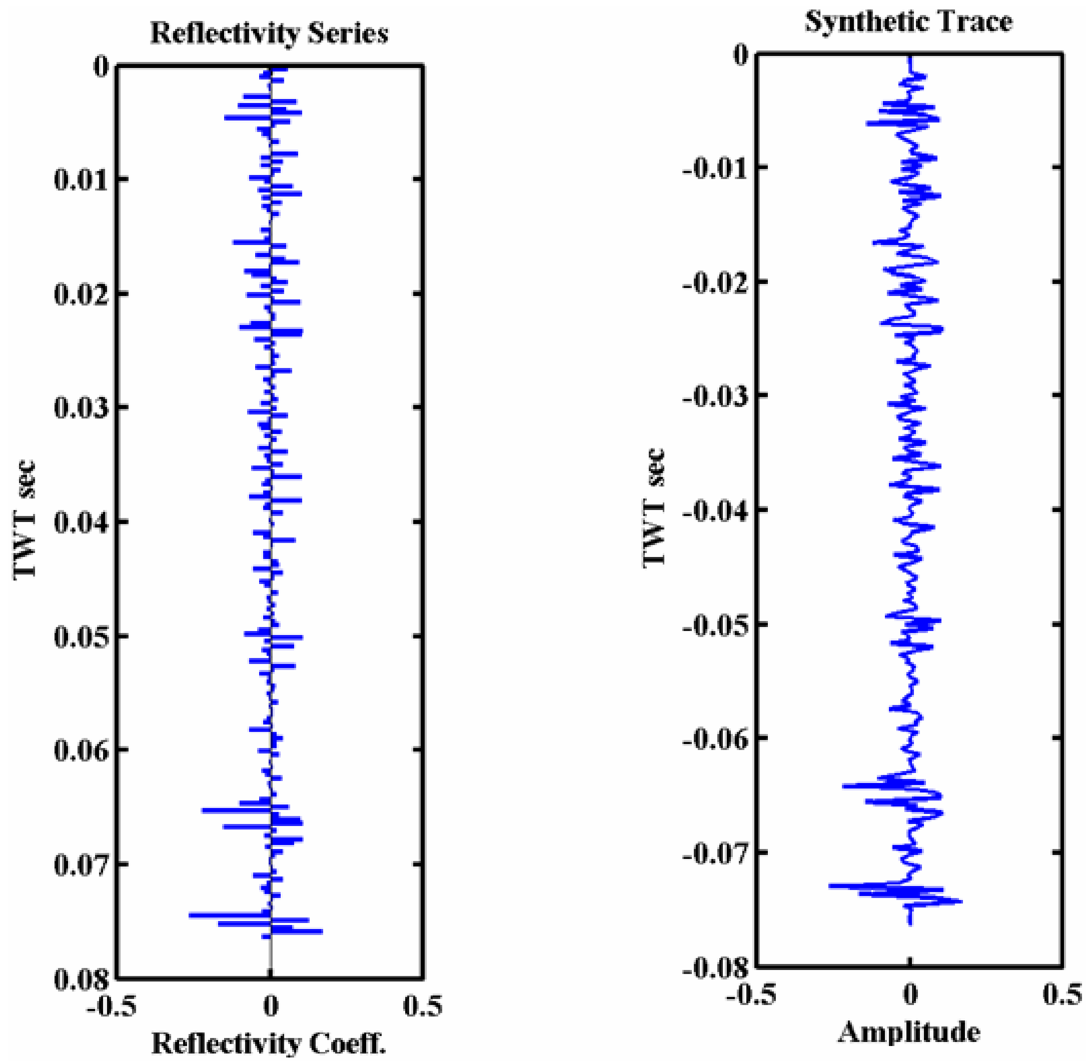

Figure 5.3a P-wave reflectivity series, and b) Synthetic seismogram, generated from velocity and density logs between the intervals 10300 ft and 11600 ft from Well C.

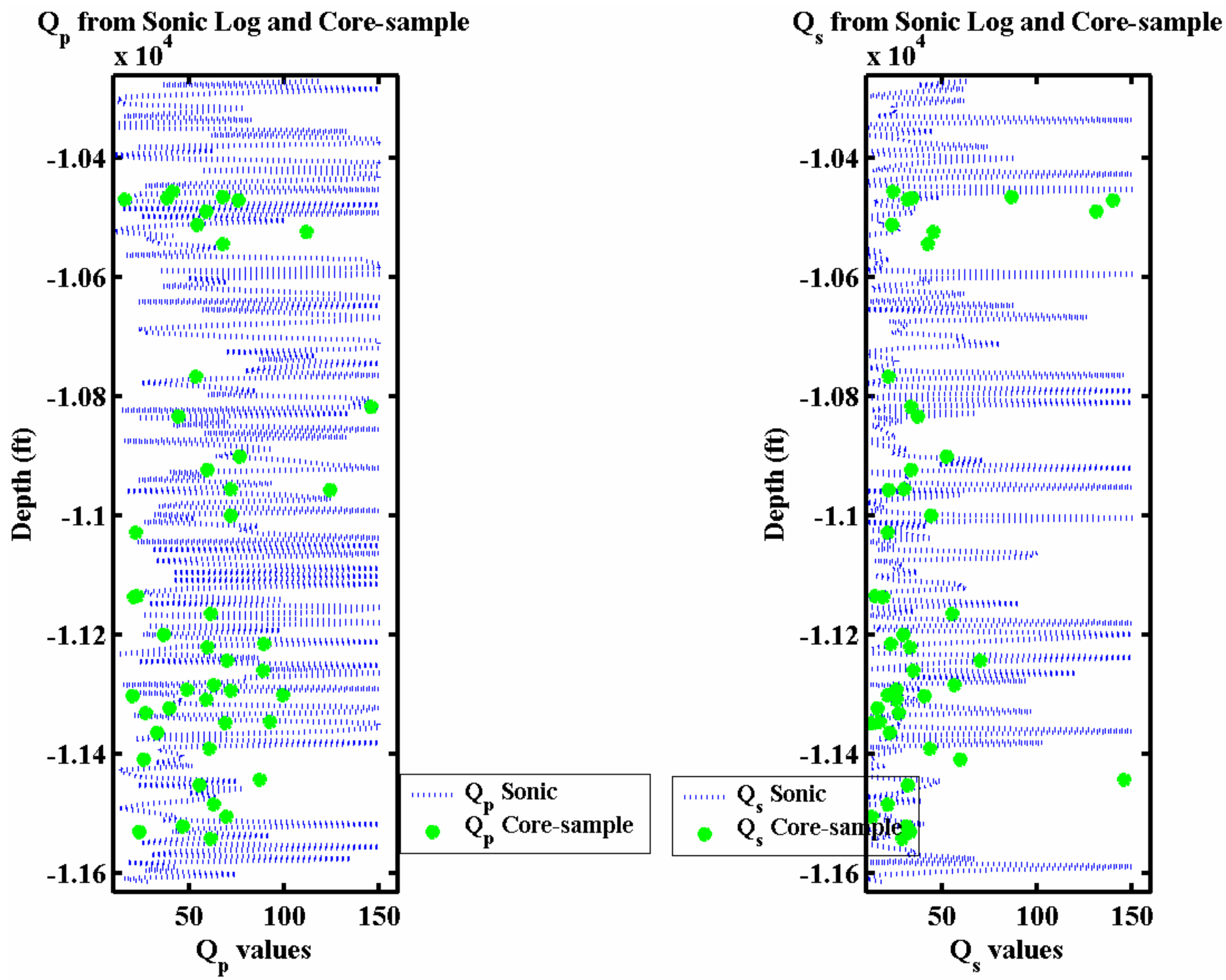

Figure 5.4. P- and S- wave sonic Q (blue dashed lines), and P- and S-wave Q from core samples (green dots) from Well C-276, a) P-wave sonic and P-wave core sample Q, b) S-wave sonic and core sample Q.

5.4 Seismic Data Processing

A 3D seismic data for quality factor (Q) analysis is from the La Concepcion Field (Figure 1.1). The 3D survey is located between 10:28:00N and 10:48:00N latitude, and 71:36:00W and 72:04:00W longitude. A 2D line (Inline171) shown in Figure 5.6 is extracted from the 3D volume, and tied to a synthetic trace from Well C-276. Then, a CMP-gather (CMP 722) is extracted from the 2D line (Figure 5.7) for processing and Q estimation. Figures 5.7 and 8 show the data have a low signal to noise ratio, specially the frequency noise. Then, to increase the signal to noise ratio, the data are filtered using General-Purpose-Band-Pass Filter (Low-cut = 4, Low-pass = 8, High-pass = 30 and High-cut = 50); compare Figures 5.7 and 5.8 with Figures 5.9 and 10. Next, CMP-gathers 720, 721 and 722 are program-control gained to recover the amplitude decay due to spherical divergence and transmission loss (Figure 5.10). In addition, on the amplitude balanced CMP-gathers shown in Figure 5.10, RMS velocity picking is performed interactively through data-driven-interactive (DDI) processing, and the picked RMS velocity panel is shown as an overlay on the CMP-gathers (Figure 5.11). The interactively picked RMS velocity, tabulated as time and velocity pair, is saved into velocity file for later use. Then, a normal move out (NMO) correction is applied to CMP-gathers, using the RMS velocity file generated earlier, to prepare the data for Q estimation and analysis. The NMO corrected CMP-gathers are shown in Figure 5.11. Even though, stretching correction was applied during NMO correction, the far offset traces still exhibit stretching characterized by wavelet broadening. Therefore, only ten traces are extracted from the CMP-gather 721, and Figure 5.12

shows the location of the traces selected, to minimize the effect of stretching during NMO correction. Besides, the traces are reduced to mitigate the effect of mode conversion due to large offset. The pre-conditioned and selected traces are converted to text format, and then exported to MATLAB for interval Q estimation using Equation 2.11 (Dasgupta and Clark, 1998). A MATLAB script is written to compute the interval quality factor. Log spectral ratio (LRS) method is used to estimate the attenuation factor. The calculated interval Q is plotted verses Two-Way-Time (TWT) and shown in Figure 5.13, and then compared with Q measurement from core samples collected from Well C-276.

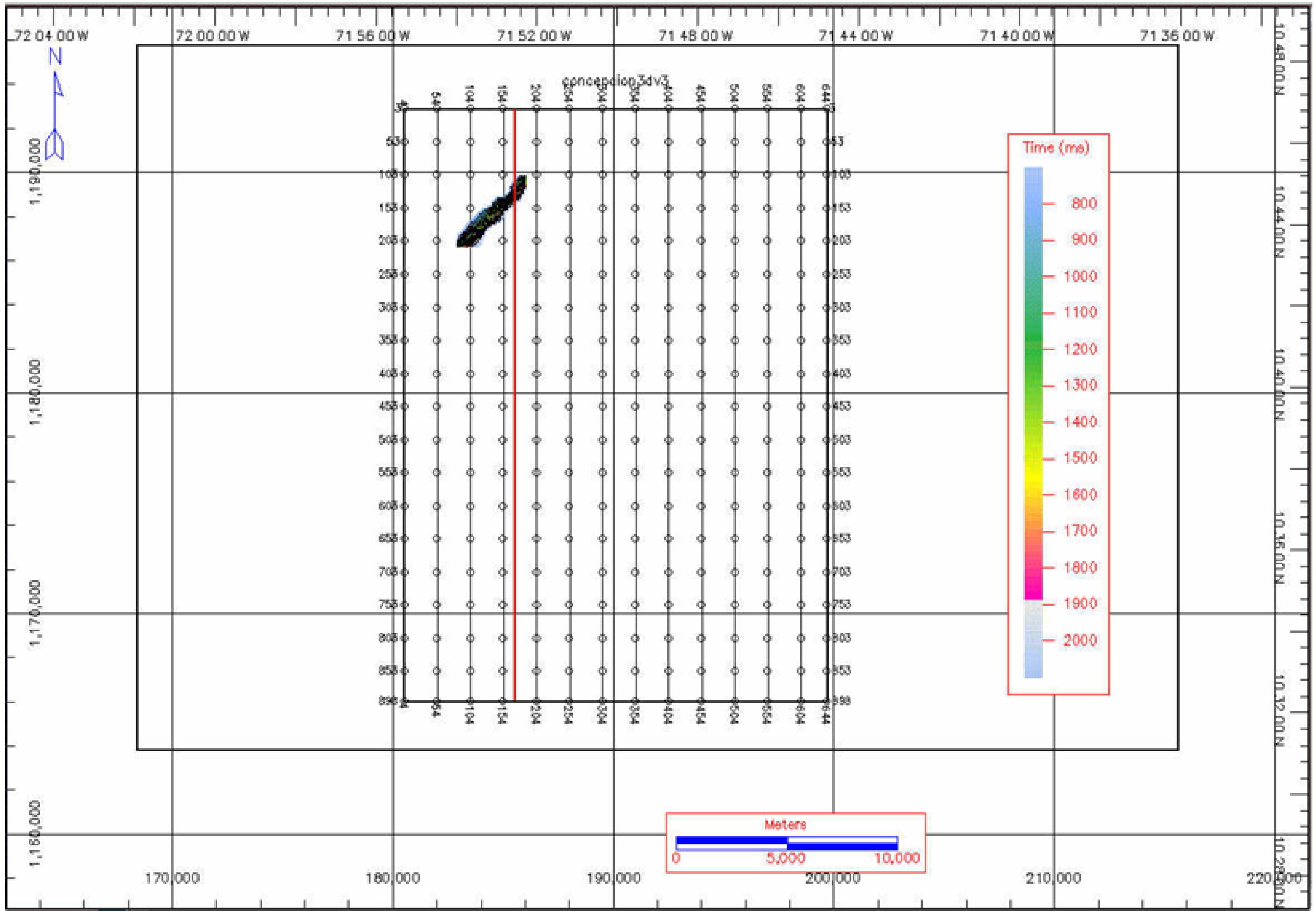

Figure 5.5 Location map of La Concepcion 3D survey (red solid line = Inline171)

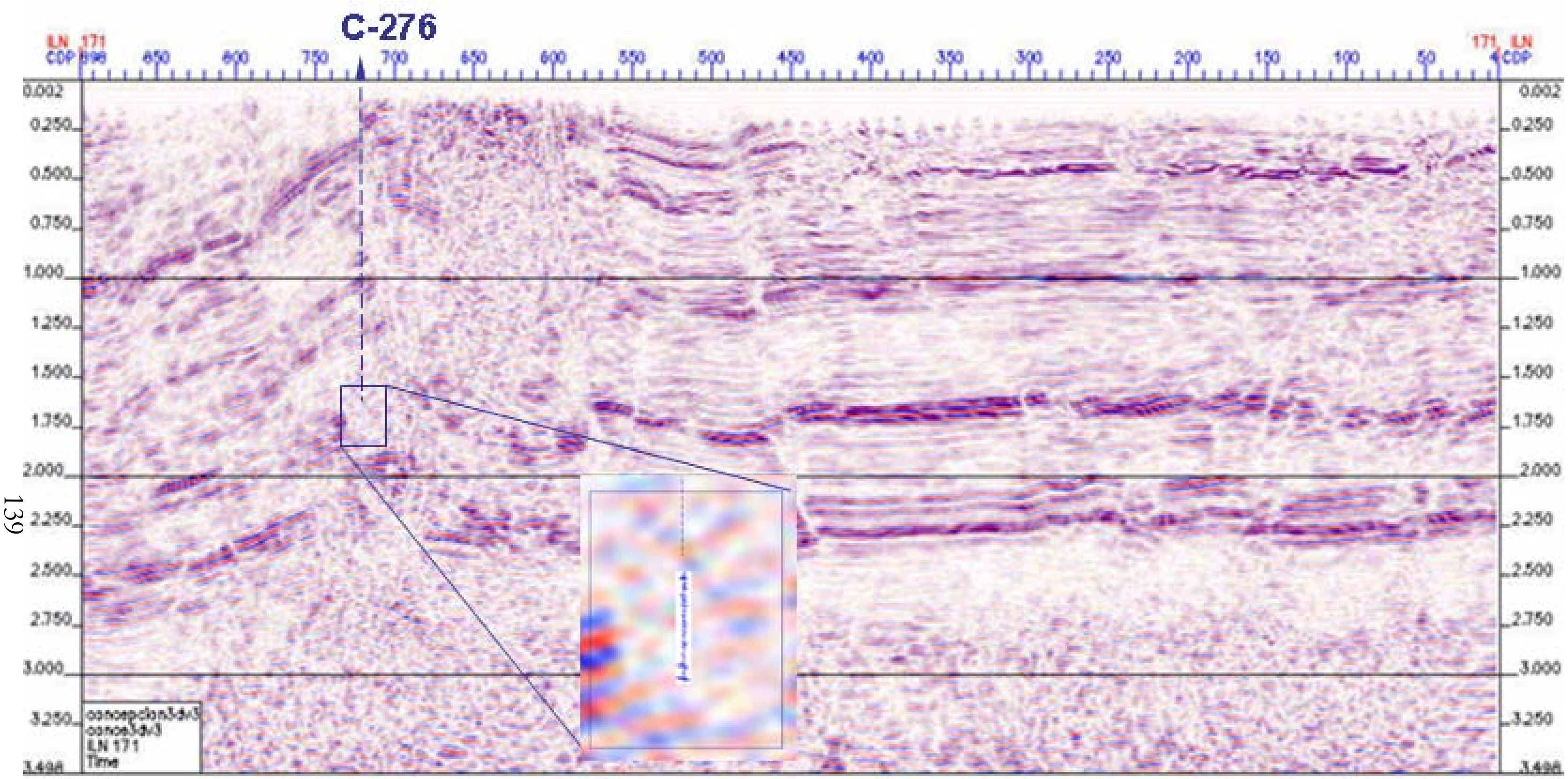

Figure 5.6. Inline171 with synthetic seismogram from Well C-276 (detail indicated with inset)

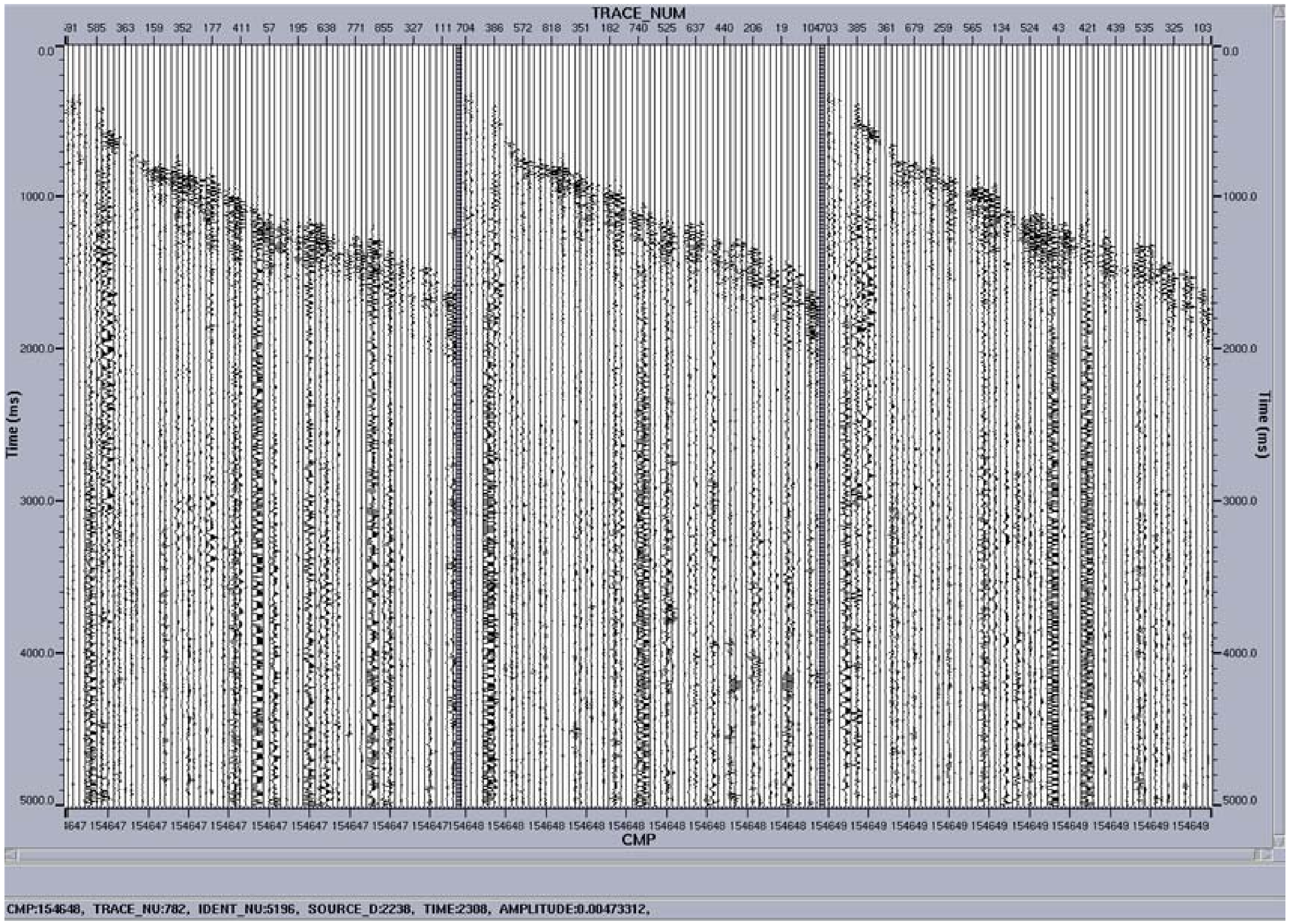

Figure 5.7 Raw CMP-gathers 720, 721 and 722, Pre- program gain, band-pass filtering and NMO correction.

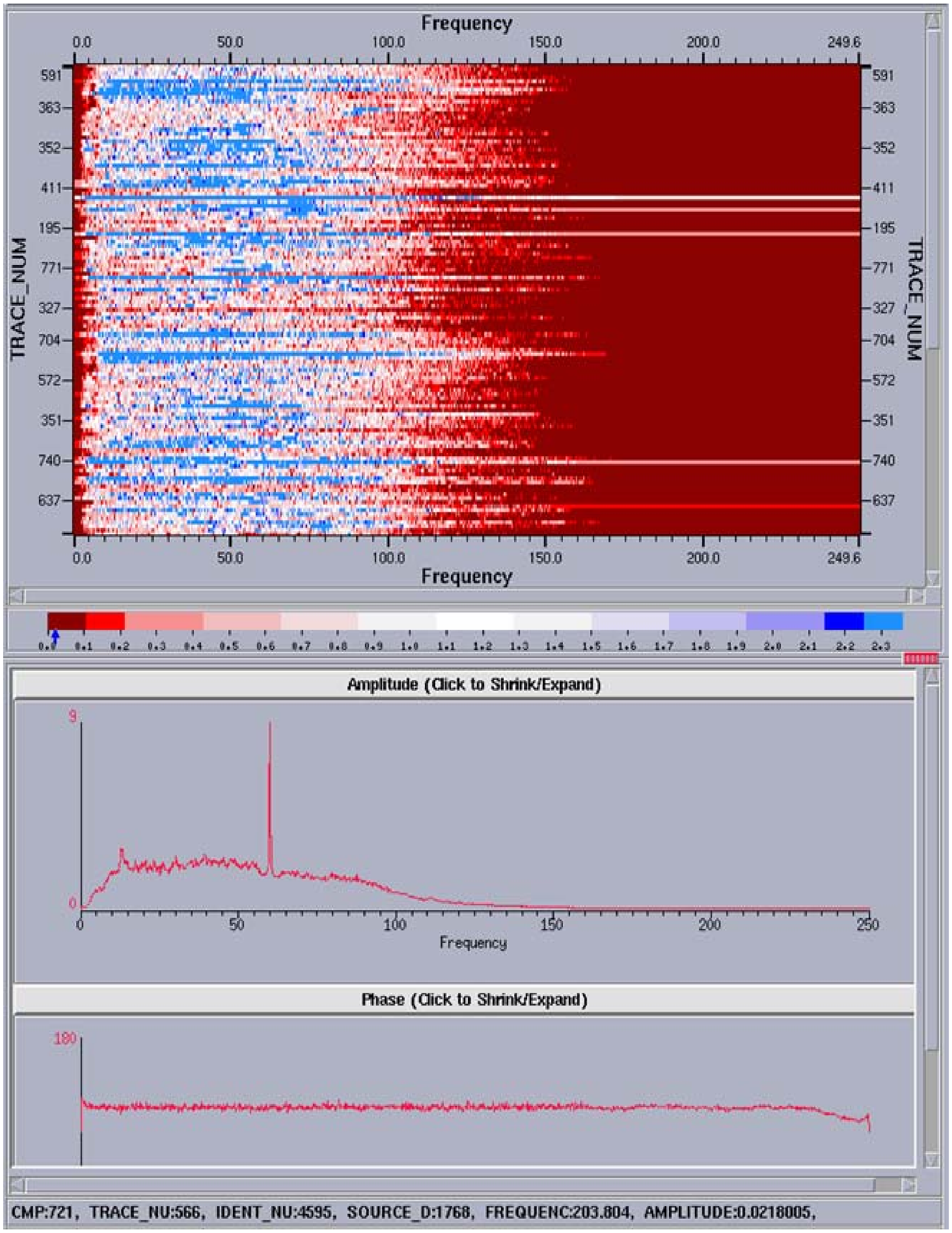

Figure 5.8 Raw CMP-gathers amplitude and phase spectra plot in the frequency domain before band-pass filtering

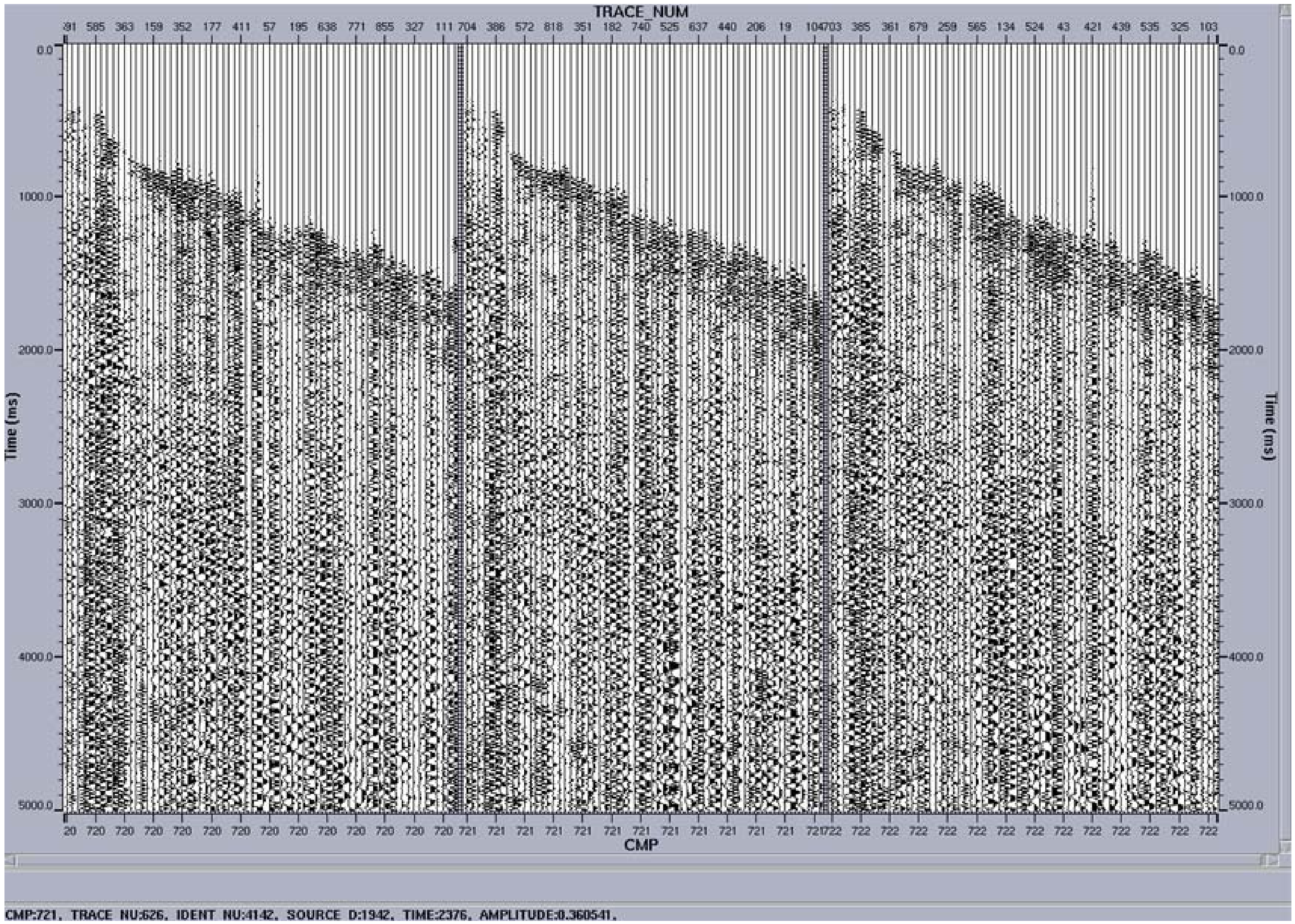

Figure 5.9 CMP-gathers post- program gain and band-pass filtering.

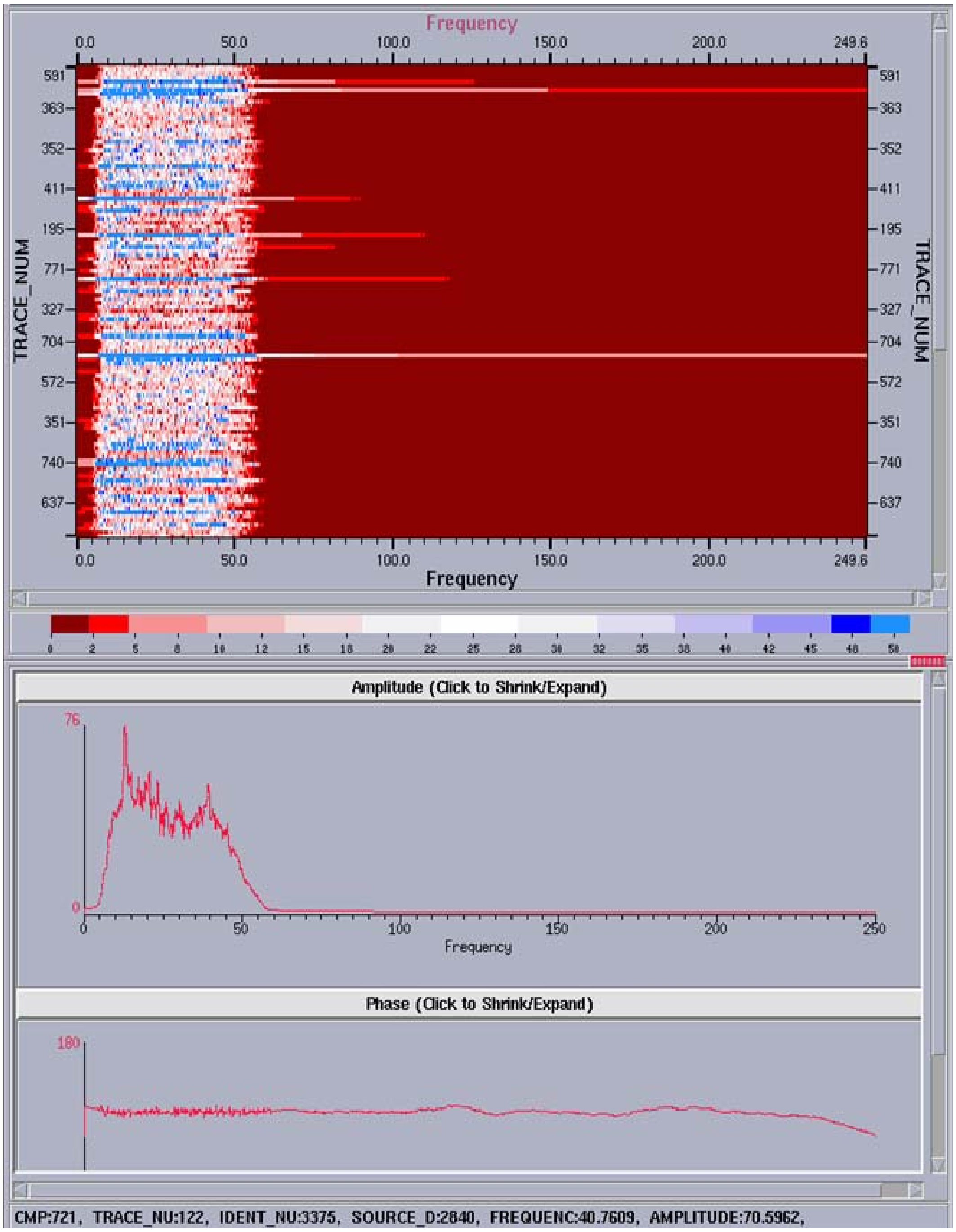

Figure 5.10 Amplitude and phase spectra plot in the frequency domain after band-pass filtering (filter: Lowcut = 4, Lowpass = 8, Highpass = 40 and Highcut = 60)

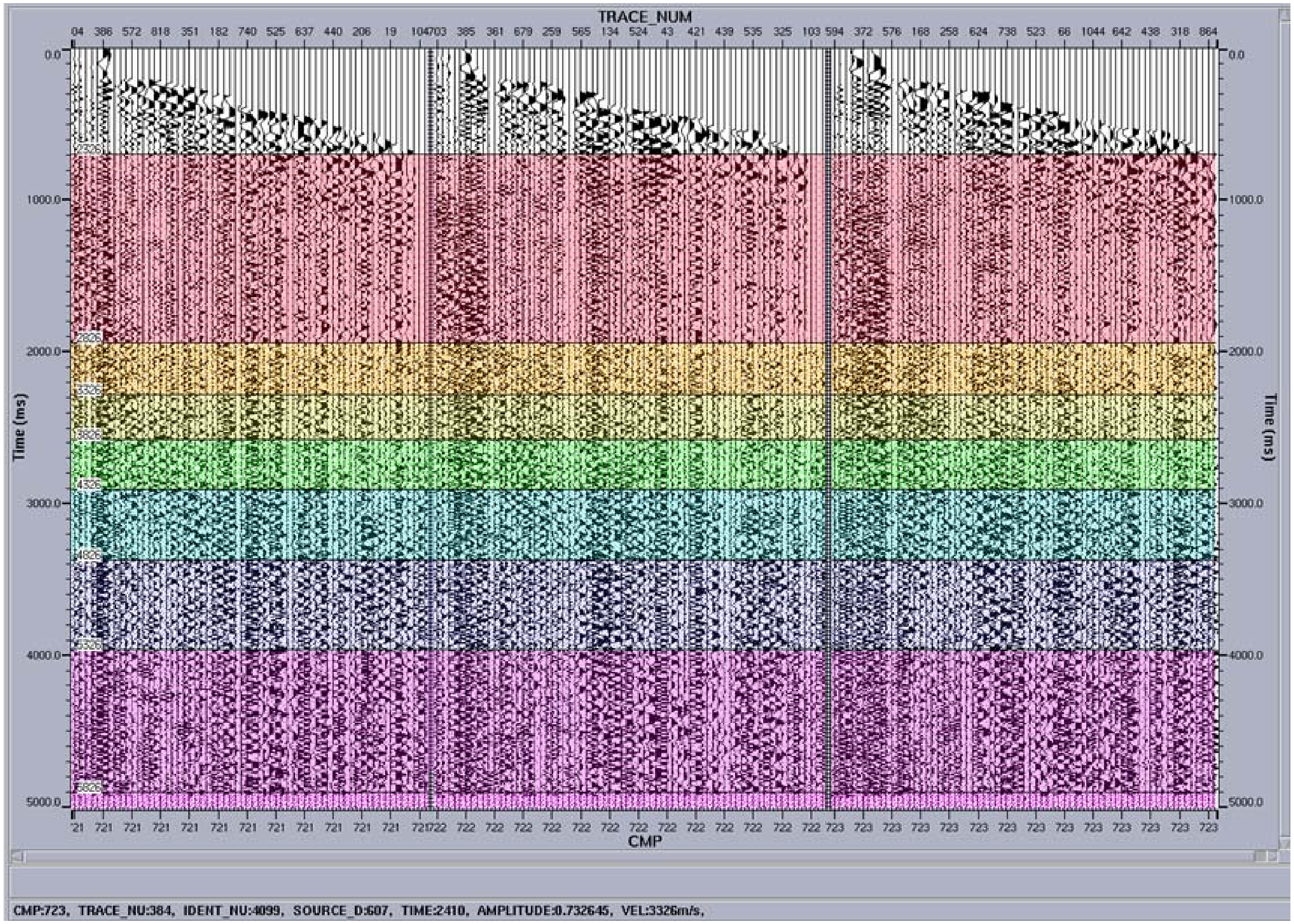

Figure 5.11 CMP-gathers 720, 721 and 722 post- program gain, band-pass filtering and NMO correction, RMS velocity shown as an overlay and color coded.

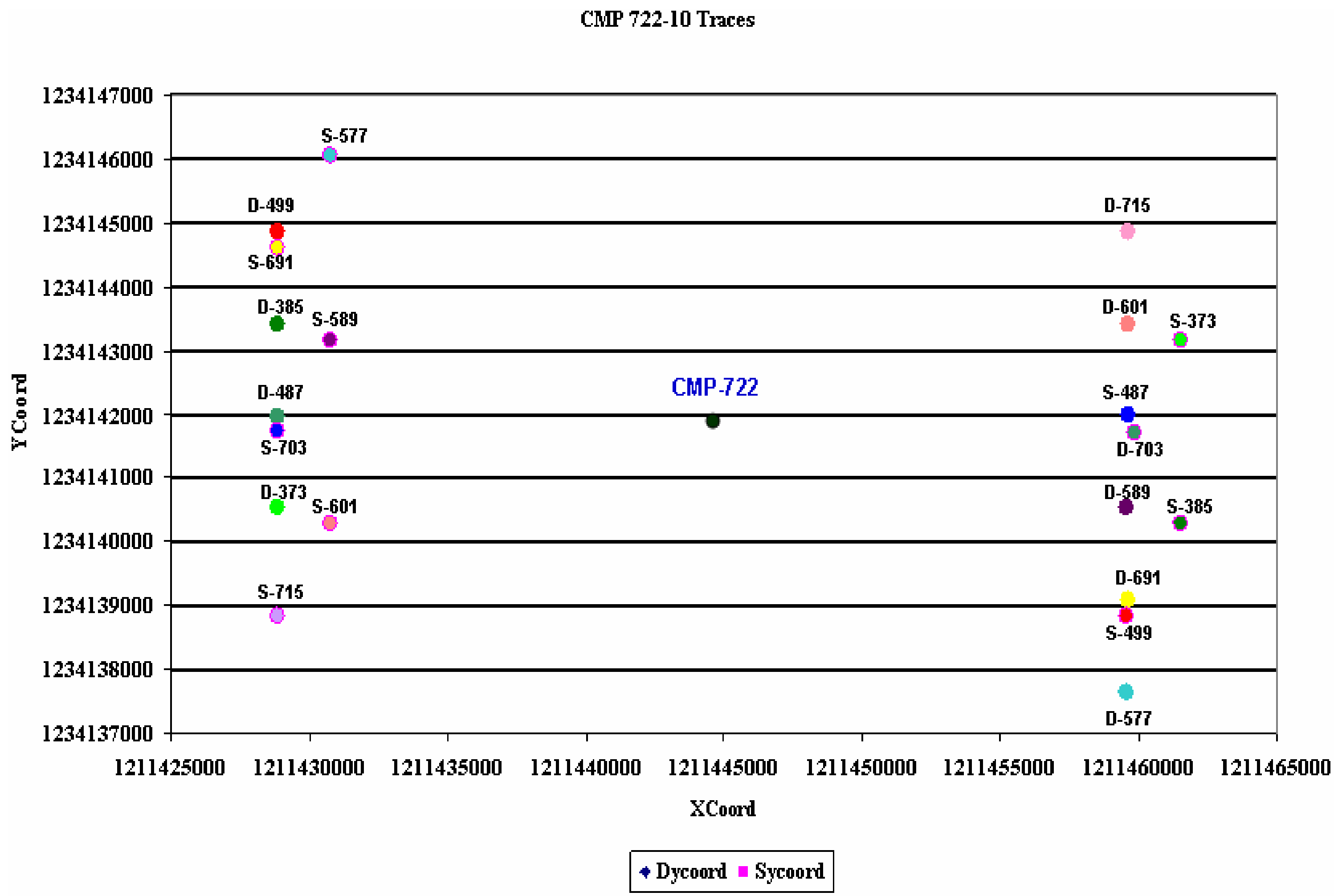

Figure 5.12 Location for CMP-gather 722 and nearest source and receiver location for 10 traces.

5.5 Observation and Discussion

Figure 5.13 shows the estimated interval Q values from the selected traces and the measured Q values from core samples collected from Well C-276 (red solid line). The figure indicates there is a good correlation between the Q values plot from the core samples and the Q values plot from the reflection seismic traces. However, there are few traces which do not show significant relationship, and these traces are the far offset traces. The figure also indicates low Q values at two locations (circled green) for the Q measurement from the core samples, as well as for the Q measurement from the reflection seismic traces. The two locations with low Q values correspond to the high porosity and permeability zones imaged by Q earlier (Figure 5.13).

Figure 5.14 shows the CMP-gathers after inverse Q filtering, where Q values measured from Well C-276 core samples are used for the inverse Q filtering. The interval filtered is between 1.66 seconds and 1.78 seconds. Based on the observation on Figure 5.14 and comparison with Figures 5.7 and 9, there is a significant improvement on the amplitude and resolution.

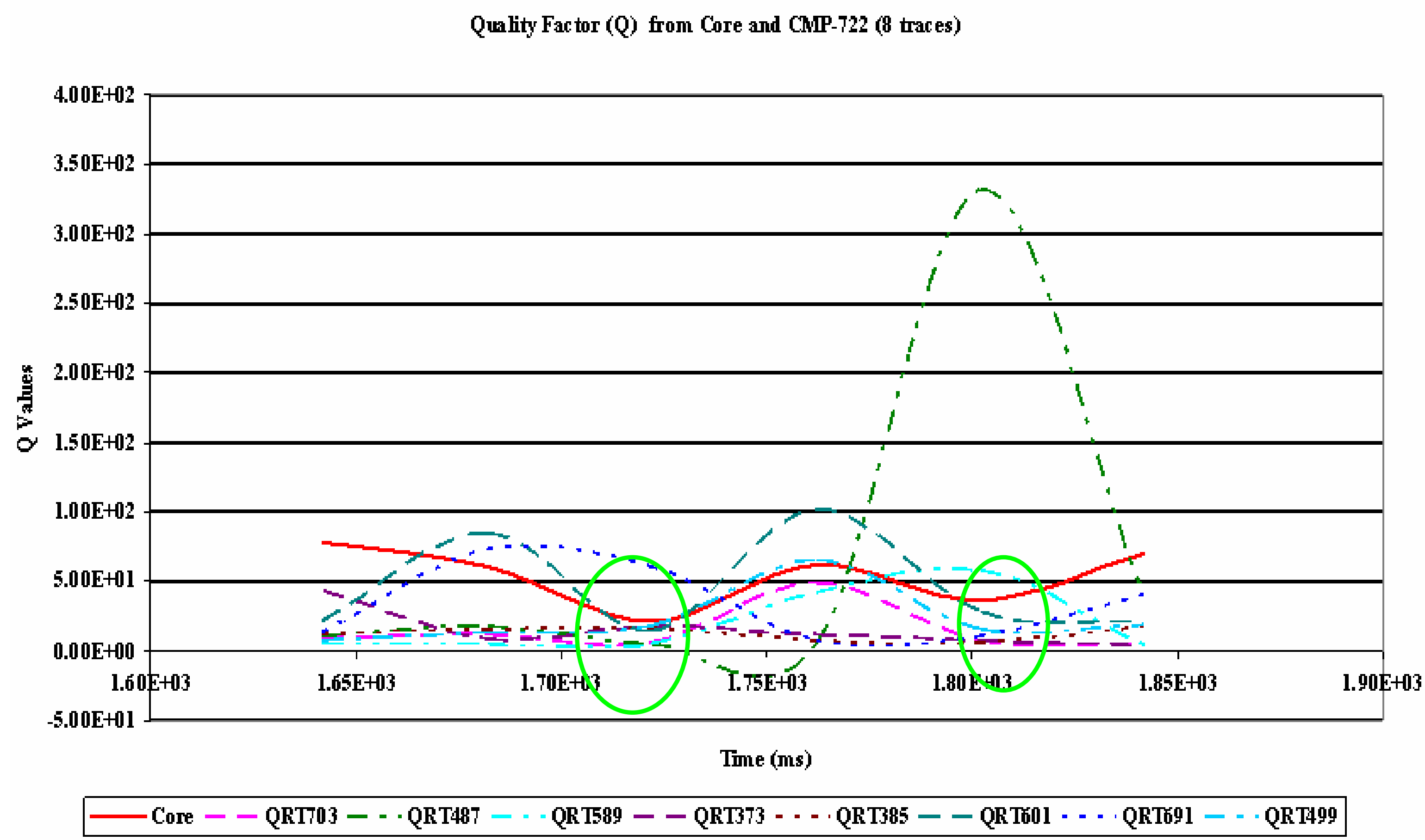

Figure 5.13 Measured Q values from core samples (red solid line), and interval Q values from reflection seismic traces of CMP-gather 722, 10 traces shown (various colors dashed lines)

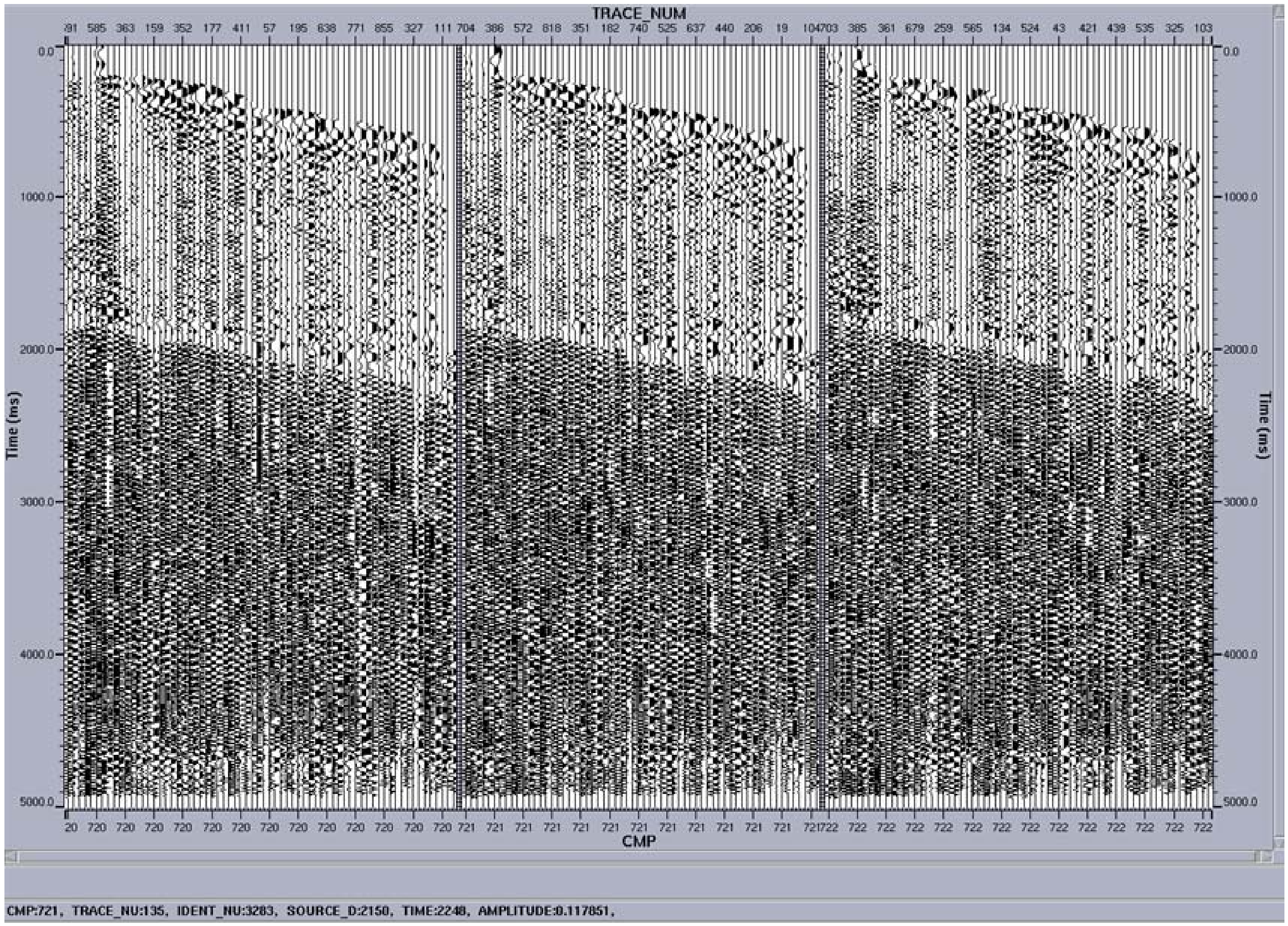

Figure 5.14 CMP gathers 720, 721 and 722, after inverse Q filtering.

5.6 Summary and Conclusions

Quality factor (Q) values computed from sonic log, Well C-276, are compared to the Q values from core samples, Well C-276, and there is a strong maching between the two Q measurements. In addition, Q values estimated from reflection seismic traces extracted from CMP-gather (CMP 722) show good relationship with the Q values calculated from the core samples of Well C-276. Correlation of Q from the core samples with porosity and permeability (Chapter 4) has indicated the presence of a positive link between Q and porosity and Q and permeability. Inverse Q filtering processing of the CMP-gathers has improved the resolution of the reflection seismic data affected by attenuation.

Therefore, geologically constrained Q measurements can have useful application for predicting petrophysical properties such as lithology, porosity and fluid characteristics, and these petrophysical properties are the critical criteria for reservoir characterization. Furthermore, knowledge of Q can help enhance seismic data quality such as resolution, by applying inverse Q filter to reflection seismic data affected presence of attenuative horizons.

REFERENCES

Aki, K. and Richard, P.G., 1980, Quantitative Seismology: Theory and Methods, W.H. Freeman and Co., San Francisco, 932 pp.

Backus, G.E., 1962. Long-wave elastic anisotropy produced by horizontal layering: J. Geophys. Res. **67**, 4427-4440.

Bernys, C.J., Zamora, L., Antunez, S., Chiquito, F., Herrera, A., Rodriguez, F., Romero, O., and Suarez O., 1996, in Petroleum geology of Venezuela annual report.

Best, A I., and McCann, C., 1995, Seismic attenuation and pore fluid viscosity in clay-rich reservoir sandstones: Geophysics, **60**, 1386-1397.

Best, A.I., McCann, C., and Southcott, J., 1994, The relationship between the velocities, attenuations, and petrophysical properties of reservoir sedimentary rocks: Geophys. Prosp., **42**, 151-178.

Birch, F., and Bancroft, D., 1938, Elasticity and internal friction in a long column of granite: Bull. SSA, **28**, 243-254.

Born, W.T., 1941, Attenuation constant of earth materials: Geophysics, v.6, 132-148.

Castanga, J.P., Batzle, M.L., and Kan, T.K., 1993, Rock physics – The link between rock properties and AVO response, in Offset-Dependent Reflectivity – Theory and Practice of AVO Analysis, J.P. Castagna and M. Backus, eds. Investigation in Geophysics, No. 8, Society of Exploration Geophysics, Tulsa, Oklahoma, 135-171.

Dasgupta, R., and Clark, R.A., 1998, Estimation of Q from surface seismic reflection data, Geophysics, **63**, 2120-2128.

Dasios, A., Astin, T.R., and McCann, C., 2001, Compressional-wave Q estimation from full-wave sonic data, Geophysical Prospecting, 49, 353-373.

Frazer, L.N., 1994, A pulse in a binary sediment. Geophys., J. Int., **118**, 75-93.

Futterman, W.I., 1962, Dispersive body waves: Journal of Geophysical Research, **67**, 5279-5291.

Gardner, G.H.F., Wyllie, M.R.J., and Droschak, D.M., 1964, Effects of pressure and fluid saturation on the attenuation of elastic waves in sands: J. Petrol. Tech., **16**, 189-198.

Hamilton, E.L., 1972, Compressional wave attenuation in marine sediments: Geophysics, **37**, 620 – 646.

Jackson, D.D., 1969, Grain boundary relaxation and the attenuation of seismic waves: Ph.D. thesis M.I.T.

Johnston, D.H., and Toksoz, M.N., 1981, Definition and terminology, in Toksoz, M.N., and Johnston, D.H., Eds., Seismic Wave Attenuation: SEG Reprint Series, **2** 1-5.

Kennett, B.L.N., 1974, Reflections, rays and reverberations. Bull. Seismology Soc. Am. **64**, 1685-1696.

Kuster, G.T., and Toksoz, M.N., 1974, Velocity and attenuation of seismic waves in two-phase media: Part II-Experimental results: Geophysics, **39**, 607-618.

Lui, Y., and Schmitt, R.D., 2002, Seismic scale effects: Dispersion, attenuation, and anisotropy by multiple scattering of waves, CSEG, Geophysics. 1-3.

Marion, D., and Couldin, P., 1992, From ray to effective medium theories in stratified media: an experimental study: 62nd Ann. Internat. Mtg., SEG's Expanded Abstracts, 1341-1343.

MathWork, 2001, MATLAB, 6: The MathWorks, Inc

Mavko, G., Mukerji, T., and Dvorkin, J., 1998, The Rock Physics Handbook, Tools for Seismic Analysis in Porous Media, Cambridge University Press, 329.

Mukerji, T., Mavko, G., Mujica, D., and Lucet, N., 1995, Scale-dependent seismic velocity in heterogeneous media: Geophysics, **60**, 1222-1233.

Murat B., 2001, Estudio Sedimentológico y de Fracturas del Pozo C-276 Cretácico de los Núcleos 1 a 21 Campo: La Concepción, Venezuela, Preparado para PEREZ COMPANC de VENEZUELA S.A.

Murat, B., and Munoz, P., 1997, The Maraca-basal La Luna Fm. Interval: a carbonate play in the Maracaibo Basin, IAS VIII Venezuelan Geological Congress and I Latin-American Congress of Sedimentology, November 1997.

Murphy, F.W. 1982, Effect of microstructure and pore fluids on the acoustic properties of granular sedimentary rocks: Ph.D. thesis Stanford University.

Murphy, F.W., 1984, Acoustic measures at partial gas saturation in tight sandstones: J. Geophysical Res., **89**, 11549-11559.

O'Doherty, R.F., and Anstey, N.A., 1971, Reflection on amplitudes: Geophysical Prospecting, **19**, 430-438.

O'Connell, R.J., and Budianisky, B., 1977, Viscoelastic properties of fluid saturated cracked solids: submitted to J. Geophysics Research., **82,** p. 5719 – 5736.

Peacock, S., McCann, C., Sothcott, J., Astin, T.R., 1994, Experimental measurement of seismic attenuation in microfractured sedimentary rocks: Geophysics, **59**, 1342-1351.

Peselnick, L., and Zietz, I., 1959, Internal friction of fine grained limestones at ultrasonic frequencies, Geophysics, **24**, 285-296.

Plona, T.J., and Tsang, L., 1979, Determination of the average microscopic dimension in granular media using ultrasonic pulses: theory and experiments. Presented at SEG 1979 Annual Convention, New Orleans, LA.

Postma, G.W., 1955, Wave propagation in stratified medium, Geophysics, **20**, 780-806.

Schreiber, E., Anderson, O.L., and Soga, N., 1973, Elastic constants and their measurement: New York, McGraw-Hill Book Co. Inc.

Sheriff, R.E., 1975, Factors affecting seismic amplitudes: Geoph. Prosp., **23,**125 – 138.

Spetzler, H., and Anderson, D.L., 1968, The effect of temperature and partial melting on velocity and attenuation in a simple binary system, J. Geophysics Res., **73**, 6051-6060.

Sun, C.T., Achenbach, J.D., Herrmann, G., 1968, Continuum theory for a laminated medium: J. Appl. Mech., **35**, 467-475.

Tittmann, B.R., Housely, R.M., Aler, G.A., and Carlin, E. H., 1974, Internal friction in rocks and its relationship to volatile on the moon: Geochem. et Cosmochin. Acta, Supp., **5**, 2913-2918.

Toksoz, M.N., Johnston, D.H., and Tamur, A., 1979, Attenuation of seismic waves in dry and saturated rocks: I. Laboratory measurements: Geophysics, **44**, p. 681-690.

Ward, R.W., and Toksoz, M.N., 1971, Causes of regional variation of magnitude in: SSA Bull. **66**, 649-670.

Watson, T.H., and Wuenschel, P.C., 1973, An experimental study of attenuation in fluid saturated porous media, compressional waves and interfacial waves: Presented at the 43rd Annual International SEG Meeting, October 22 in Mexico City.

Winkler K.W. and Nur A., 1979, Pore fluids and seismic attenuation in rocks: Rock physics project Geophysics Department Stanford University, Stanford, California.

Yilmaz, O., 1987, Seismic Data Processing, Soc. Expl. Geoph. 526.

Zanng, C., and Ulrych, T.J., 2002, Estimation of quality factor –an analytical approach, CSEG, Geophysics, 1-3.